APPLICATION OF NATIVE MASS SPECTROMETRY AND ION MOBILITY-MASS SPECTROMETRY TOWARDS THE STUDY OF SMALL MOLECULE COMPLEXES, PROTEIN COMPLEXES, AND ANTIBODIES

A Dissertation

by

CHRISTOPHER S. MALLIS

Submitted to the Graduate and Professional School of
Texas A&M University
in partial fulfillment of the requirements for the degree of

DOCTOR OF PHILOSOPHY

Chair of Committee,	David H. Russell
Committee Members,	Arthur Laganowsky
	Sarbajit Banerjee
	Penny K. Riggs
Head of Department,	Simon North

December 2021

Major Subject: Chemistry

ABSTRACT

Native mass spectrometry (nMS) is an expanding technique whereby ions with low internal energies are ionized and non-covalent structural elements remain intact following desolvation from solution-phase molecules to solvent-free, gas-phase ions. By retaining weak, non-covalent interactions (i.e. H-bonds, salt bridges, hydrophobic contacts), these ions can be kinetically trapped in their solution conformers for analysis in the gas phase. Hyphenation of nMS with ion mobility (nIM-MS) then provides structural details of conformer preferences by separating ions by their size and/or shape to complement the mass and charge information encoded in the resulting IM-MS spectra.

Principles of nIM-MS are applied to study labile non-biologically relevant small molecules formed through coordination-driven self-assembly (CDSA) reactions of rigid bidentate ligands capped with electron donating pyridyl groups or electron accepting, square planar Pt(II) groups. By retaining low ion internal energies, we show that these reaction products can maintain their solution-phase structures in the gas phase. nMS methods are also applied without IM separation towards the characterization of native large biomolecular complexes (>100 kDa), including soluble protein complexes, membrane protein complexes, and the protein chaperonin GroEL. Under the appropriate solution and instrument conditions, these protein complexes produce well-resolved charge state distributions with high sensitivity to better interrogate large protein contaminants at low relative abundances.

When sampled from native-like buffer conditions (e.g. ammonium acetate), high resolution MS of the monoclonal antibody (mAb), human immunoglobulin gamma-1 kappa (IgG1κ) reveals the expected *N*-glycan mass profile. In addition to the distribution of glycoforms, at high resolution, we observe signals corresponding to an increase in mass of 40 Da to each glycan peak. The mass shift does not correspond to a common post-translational modification; however, we interrogate the identity of this mass shift as (i) an exchange of mannose (Man) or galactose (Gal) sugar residue with an N-acetylglucosamine (GlcNAc) on the *N*-glycan structures, (ii) possible metal adduction of endogenous K^+ or Ca^{2+} cations, or (iii) single point mutations of amino acid residues in the primary sequence of the heavy chain.

Finally, nIM-MS spectra can have utility in discerning shifts in ground-state arrival-time or conformer population distributions; however, for some proteins and protein complexes, the changes in structure may not significantly affect the ground state conformer distributions. Collision-induced unfolding (CIU) works to probe the gas-phase conformational landscape through progressive collisional activation of the flexible ion of interest, (namely proteins and protein complexes) and correlating the collision-cross section (CCS) distribution as a function of collision energy or an instrument collision voltage. CIU experiments have traditionally been performed on travelling-wave IMS (TWIMS) based instrumentation; however, these instruments require external calibrants for CCS determinations and lose considerable sensitivity at the high *m/z* regimes needed to sample larger native protein complexes. We worked to evaluate a new desolvation assembly design with capabilities for higher energy CIU of large protein complexes in N_2

without the need for additional dopant gases (e.g. Ar, SF_6) in collaboration with a cross-laboratory study prior to commercialization of the technology.

DEDICATION

This dissertation is dedicated to my dad, Larry Mallis, for inspiring me to pursue an advanced degree in chemistry and for providing an early introduction into mass spectrometry. It is dedicated to my mom, Carine Mallis, for cheering me on throughout the process and for putting up with chemistry talk whenever I am home and nearby to dad. It is dedicated to my grandparents, Dora and Godfried Dekeyser (Oma & Opa, respectively), for providing me a wonderful and supportive home away from home in Houston. Finally, it is dedicated to my loving fiancée, Tristin Nyman, for all her endless support and encouragement through the hard days, for her celebration and homecoming on the good days, and for her partnership and care as we navigated the COVID-19 pandemic together. May our life together continue beyond Texas with the love and support we have found in each other.

ACKNOWLEDGEMENTS

I would like to thank my advisor, Professor David H. Russell, for implicitly and explicitly teaching me the philosophy of science and research through his patient mentorship. I am thankful for our discussions of research problems and teaching philosophies, for his encouragement and suggestions for new experiments, and for his insight in communicating a story when presenting results. I would also like to thank my committee member, Prof. Arthur Laganowsky, for his advanced insight into protein structure and function and providing an open door for discussion and my other committee members, Prof. Sarbajit Banerjee and Prof. Penny Riggs, for their encouragement throughout my graduate career.

I would also like to thank all of the present and former Russell group members for their training and insights. Specifically, I would like to thank Dr. Nicole Wagner for her insight into graduate school and for my initial mass spectrometer trainings. I would also like to thank Jacob McCabe for being like an academic brother to me, from coffee sessions, to tailgating in the MS lot, to our white board discussions, you have been a great friend and colleague to me. I want to thank Will Seward and Karl Yeager of the TAMU Chemistry Machine Shop for helping prepare and trim the homebuilt parts that made the experiments Chapter 3 possible. Also to John Sausen and Ruwan Kurulugama for helping to develop and organize the wonderful collaboration between the Russell Research Group and Agilent Technologies for the work performed on the Agilent 6545XT Q-TOF and 6560 IM-Q-TOF.

I also want to acknowledge all the science and chemistry teachers and professors I have had from North Penn High School, Penn State University, and Texas A&M University for your inspiring passion and professionalism to take chemistry and make it understandable. I have often claimed that chemistry is not difficult if you understand the fundamentals, and you have all provided an outstanding foundation for pursuing a higher degree in chemistry.

Lastly, I would like to thank my friends for their support throughout graduate school. Specifically, Jordon Benzie and Kelly Robert for helping Tristin and me stay sane through the pandemic shutdowns with our Uno nights. Also, thanks to TJ for helping us navigate the end of the pandemic and for being an overall great companion.

CONTRIBUTORS AND FUNDING SOURCES

Contributors

This work was supervised by a dissertation committee chaired by Professor David H. Russell with committee members Professor Arthur Laganowsky and Professor Sarbajit Banerjee of the Department of Chemistry and Professor Penny K. Riggs of the Department of Animal Science at Texas A&M University.

The self-assembly reaction samples analyzed in Chapter 2 were provided by Dr. Manik Saha and Professor Peter J. Stang of The University of Utah. The membrane protein complex samples analyzed in Chapter 3 were provided by Jixing Lyu and Professor Arthur Laganowsky of the Department of Chemistry. The GroEL chaperonin samples analyzed in Chapter 3 were provided by Dr. Andrew Roth and Professor Hays Rye of the Department of Biochemistry and Biophysics. The analyses of the membrane protein complex data depicted in Chapter 3 were conducted in part by Dr. Xueyun Zheng of the Department of Chemistry. The protein and protein complex samples using in Chapter 5 were provided by Dr. Varun Gadkari and Prof. Brandon Ruotolo as part of the cross-laboratory study. The prototype desolvation assembly used in Chapter 5 to facilitate higher energy collision-induced unfolding experiments was designed by Dr. Ruwan Kurulugama and provided by Agilent Technologies. The computer-aided design drawing shown in Figure 6.2(D) was prepared by Jacob W. McCabe.

All other work conducted for the dissertation was completed by the student independently.

Funding Sources

This work was made possible in part by the National Institutes of Health under Grant Numbers P41GM128577 and R01GM121751, and the National Science Foundation under Grant Number CHE1707675. Its contents are solely the responsibility of the authors and do not necessarily represent the official views of the funding agencies.

NOMENCLATURE

ADCs	Antibody-drug conjugates
ADH	Alcohol dehydrogenase
AmA	Ammonium acetate
ATD	Arrival-time distribution
β-ME	β-mercaptoethanol
BSA	Bovine Serum Albumin
CA	Collisional activation
CCS	Collision cross section
CDR	Complementarity-determining regions
CDSA	Coordination-driven self-assembly
CE	Collision energy
CID	Collision-induced dissociation
CIU	Collision-induced unfolding
CRM	Charge residue model
CSD	Charge-state distribution
CV	Collision voltage
DTIMS	Drift tube ion mobility spectrometry
DTT	Dithiothreitol
E_{lab}	Laboratory-frame collision energy
ECD	Electron capture dissociation

EDDA	Ethylenediamine diacetate
ESI	Electrospray ionization
F_{ab}	Antigen-binding fragment
F_c	Crystallizable fragment
Fuc	Fucose residue
Gal	Galactose residue
GlcNAc	N-acetylglucosamine residue
IEM	Ion evaporation model
IgG1	Immunoglobulin gamma, subclass 1
ISD	In-source dissociation
IST	In-source trapping
m/z	Mass-to-charge ratio
mAb	Monoclonal antibody
Man	Mannose residue
MD	Molecular dynamics
MW	Molecular weight
Myo	Horse heart myoglobin
nESI	Nanoelectrospray ionization
nIM-MS	Native ion mobility-mass spectrometry
nMS	Native mass spectrometry
PDB	Protein data bank
PK	Pyruvate kinase

PTM	Post-translational modification
Q	Quadrupole
RMSD	Relative mean standard deviation
RSD	Relative standard deviation
SA	Streptavidin from *Streptomyces avidinii*
SASA	Solvent-accessible surface area
SNR	Signal-to-noise ratio
SY	Survival Yield
TAMU	Texas A&M University
TCEP	Tris(2-carboxyethyl)phosphine
TDP	Top-down proteomics
TEAA	Triethylammonium acetate
TOF	Time-of-flight
TWIMS	Travelling wave ion mobility spectrometry
Ubq	Bovine ubiquitin
VU	Vanderbilt University

TABLE OF CONTENTS

Page

LIST OF FIGURES

Page

LIST OF TABLES

Page

1. INTRODUCTION

Mass spectrometry (MS) and ion mobility-MS (IM-MS) are powerful analytical characterization tools for interrogation of gas-phase structures of intact macromolecular ions ranging from small peptides[1-3] and salt clusters[4, 5] to complex protein machinery[6-8] and intact virus capsids[9-11]. IM-MS provides high-resolution and high-fidelity measurements that can be particularly impactful when analyzing complex mixtures by revealing what may be hidden by low resolution and/or solution-averaged measurements.[12, 13] Herein, we apply methods of native MS and native IM-MS to study labile products of self-assembly reactions,[14] evaluate structure and topology of native protein complexes,[15] interrogate small (~40 Da) mass shifts on native, intact antibody ions, and evaluate new ion optic designs for performing collision-induced unfolding of protein and protein complex ions.

1.1. Native Mass Spectrometry

MS-based analytical methods fundamentally rely on the ability to ionize, transmit, separate, and detect gas-phase ions based on their mass-to-charge (*m/z*) ratios. Ionization techniques commonly include matrix-assisted laser desorption ionization (MALDI) and electrospray ionization (ESI). While ESI is often used in conjunction with separation techniques (e.g. high-performance liquid chromatography, capillary electrophoresis), these methods are often optimized under denaturing solution conditions using organic solvents and low pH buffers. These denaturing solvents can disrupt the non-covalent

contacts that hold proteins and other small molecules together. In contrast, native MS (nMS) is often defined by the ability to retain non-covalent interactions (e.g. H-bonds, salt bridges, hydrophobic patches) representative of the native solution environment upon transition from the solution phase to solvent-free, gas-phase ions.[16] The traditional thermochemical definition of native structure is derived from the conformation with the lowest free energy and is often described by three-dimensional energy landscapes referred to as Dill folding funnels as shown in **Figure 1.1.**[17, 18] Native protein structures reside at the low-energy base of the folding funnel, and high-energy, non-native or denatured structures reside at the upper rim of the funnel. In between the high- and low-energy regimes exist partially stable thermodynamic wells in which protein folding intermediates may reside.

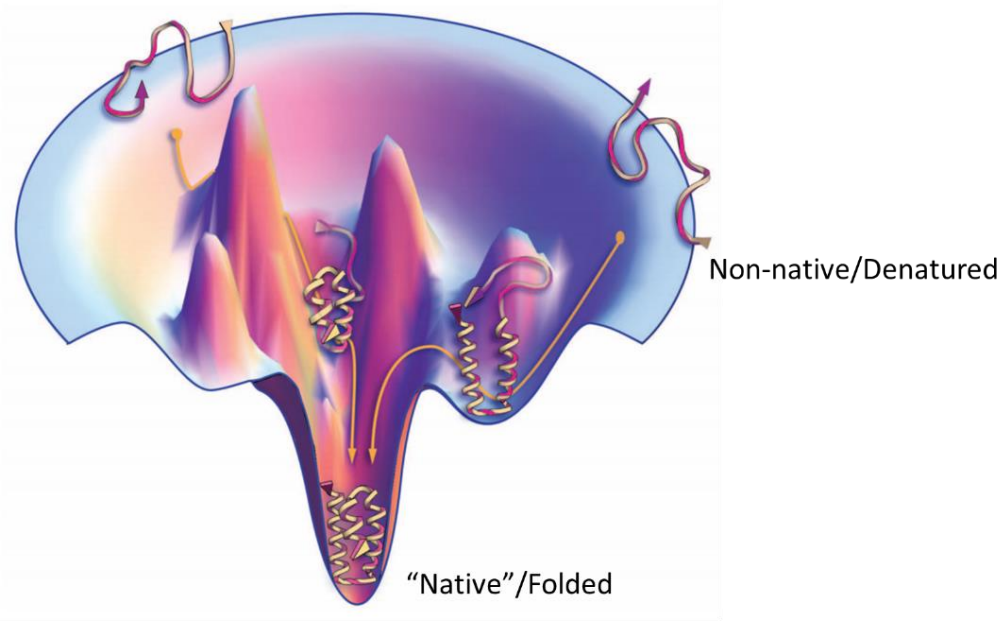

Figure 1.1. The potential energy landscape for proteins is depicted as a three-dimensional funnel containing many high-energy, denatured and non-native conformers at the upper rim and very few low energy, native or folded conformers at the base. Adapted from *Science*, **2012**, *388*, 1042-6. Reprinted with permission from AAAS.[18]

Maintaining native or native-like structures is partially achieved through replacement of denaturing organic solvents and acids with nMS-compatible buffers and cosolutes, including ammonium acetate (AmA), triethylammonium acetate (TEAA), and ethylenediamine diacetate (EDDA).[19] nMS also requires the "soft" ionization and transmission of gas-phase ions whereby ions are gently transmitted through the MS instruments while minimizing effects of collisional activation, ion heating, and gas-phase unfolding.[20] The primary challenges of nMS are two-fold: (1) preparing clean samples that require minimal additional energy to clean the ions following desolvation[19] and (2) achieving a balance between minimizing ion activation and maximizing ion sensitivity and transmission.[21, 22] On the latter point, for nMS experiments, mass spectrometers are often tuned to minimize effects of collisional activation through the reduction of the potential gradient across the instrument; however, reduced potentials can lead to reduced ion transmission and sensitivity.[23]

For more flexible ions, the effects of collisional activation are typically not observed without an additional separation technique (*e.g.* ion mobility spectrometry); however, small, labile ions and labile protein complexes can fragment and/or dissociate even under mild collisional activating conditions.[14, 21] This can lead to potential artifacts in the mass spectrum as signals may be observed that do not correlate to the native solution environment. Although these signals may still be informative for certain applications (*viz.* top-down proteomics),[24, 25] the complex stoichiometry or topology may be completely

lost. Therefore, careful instrument tuning must be performed especially for analyses of complexes held together by weak intramolecular interactions.[21, 26-28]

1.2. Nanoelectrospray Ionization

Electrospray ionization is achieved through application of a potential offset between a spraying needle and the inlet or spray shield at the entrance to a mass spectrometer. This is typically accomplished using high voltage power supplies as shown in **Figure 1.2** with application of 1-3 kV. This potential offset leads to the formation of a Taylor cone from which charged parent droplets are sputtered.[29] Solvent evaporation then leads to accumulation of surface charge until the Rayleigh limit[30] where following Coulomb fission or explosion events lead to formation of smaller product droplets. This process continues until solvated ions in microdroplets are desolvated into solvent-free, gas-phase ions. Specific desolvation mechanisms include the ion evaporation model (IEM) and charged residue model (CRM).[31] In addition to the formation of solvent-free, gas-phase ions, desolvation also produces ions with low internal energies due to evaporative cooling effects, termed "freeze-drying effect" by Beauchamp and coworkers.[32] These effects will then kinetically and thermodynamically trap protein solution-phase structures as gas-phase conformers following some gas-phase collapse and potential salt bridge rearrangements on the protein surface.[33]

A hallmark of nMS of proteins and protein complexes are mass spectra with lower and more narrow charge-state distribution (CSD) than what would be observed from harsher solvent or instrumental tune conditions. CSD characteristics are often

representative of the solvent-accessible surface area (SASA) of the biomolecular ions as unfolded, non-native ion conformers will have greater SASA and generally produces mass spectra with wider CSDs centered at higher charge states and subsequently lower *m/z* ranges.[34] Recently, nMS has achieved a resurgence through the use of static nanoESI (nESI) emitters. Some practical improvements that these nESI emitters provide are the significantly lower sample consumption as a few microliters of sample can be used for hours-worth of data collection at approximated flow rates of nanoliters per minute.[35] In addition, the smaller emitters produce smaller droplets with fewer solvent and cosolute molecules to remove via desolvation and collisional activation. Also, smaller emitters with submicron outer diameters at the emitter tip have been used to essential desalt proteins in nonvolatile buffers for determination of protein structure without offline buffer exchange or desalting.[36]

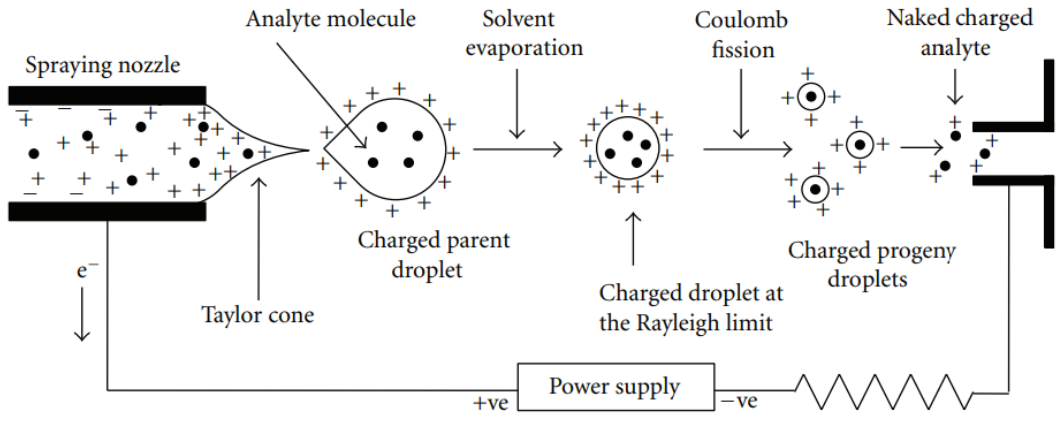

Figure 1.2. Applying a potential offset between the spray needle (left) and the MS inlet (right) produces a Taylor cone. This Taylor cone produces charged droplets that undergo solvent evaporation and Coulomb fission until solvent-free, gas-phase ions are formed as naked charged analytes. Reprinted with permission from *International Journal of Analytical Chemistry*, **2012**, *2012*, 1-40. Copyright 2012 Banerjee *et al.* Open-Access License.[31]

1.3. Ion Mobility Spectrometry

Ion mobility spectrometry (IMS) provides the separation of ions under the influence of a weak electric field in the presence of a neutral, inert buffer gas (e.g. He, N_2). Ion separation is governed in large part due to the electronic forces pulling the ions through the drift tube (which increase with increasing ion charge) and the friction forces dragging the ions pushing the ions back due to collisions with the background gas (which increase with increasing size and/or surface area). In general, IMS leads to separation based on an approximate size-to-charge ratio that determines the ions mobility, *K*, through the drift region. For the studies presented in **Chapter 2** and **Chapter 4**, instruments employing traveling wave IMS (TWIMS, **Figure 1.3(A)**) and uniform-field drift tube IMS (DTIMS, **Figure 1.3(B)**) were used, respectively.

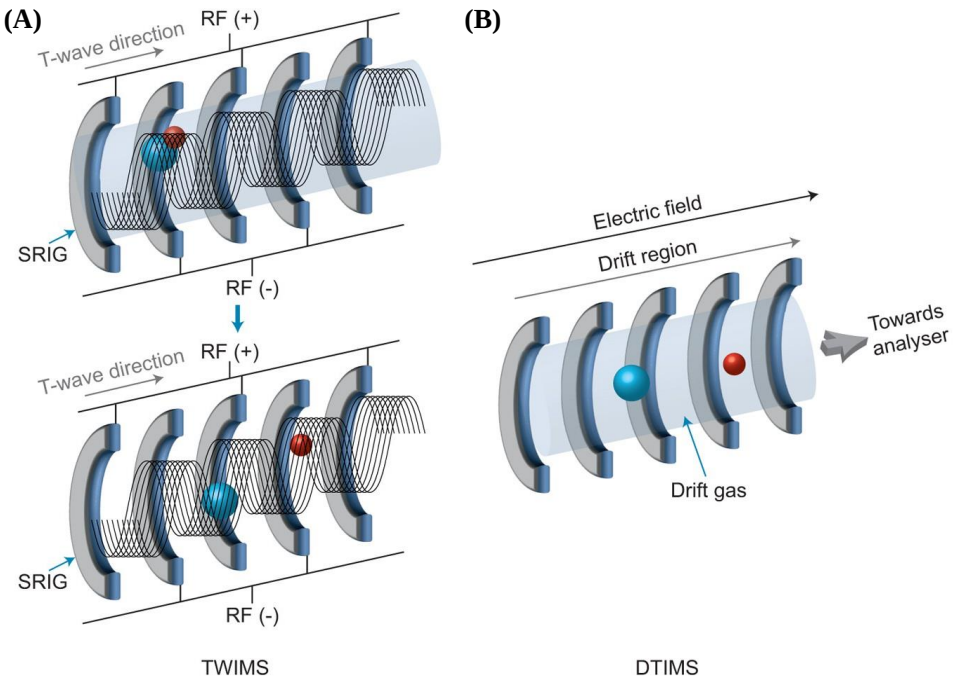

Figure 1.3. Schematics of the IMS devices for (A) TWIMS and (B) DTIMS show separation of ions with large (blue) and small (red) CCS values. Reprinted with permission from *Nature Chemistry*, 6, 281-294. Copyright 2014 Macmillan Publishers Limited.[37]

In uniform field DTIMS devices, the drift velocity of the ions, *v*, is a product of the electric field, *E*, and the ion mobility, *K*, as shown in **Equation 1.1**.

$$\boldsymbol{v = KE} \qquad \textbf{(Eq. 1.1.)}$$

The **Equation 1.1** can be rearranged such that the ion mobility, *K*, is be calculated from the resulting drift velocity, *v*, (as the drift time, t_d, divided by the drift tube length, *L*) and the applied electric field (as the potential difference between the DT entrance and exit potentials, ΔV, divided by the drift tube length, *L*), as shown in **Equation 1.2.**

$$\boldsymbol{K = \frac{L^2}{\Delta V * t_d}} \qquad \textbf{(Eq. 1.2.)}$$

From the experimentally calculated mobility, *K*, the rotationally averaged, ion-neutral collision cross section (CCS), Ω, can be calculated from first-principles physics following the Mason-Schamp Equation[38] shown in **Equation 1.3.**

$$\Omega = \left(\frac{3ze}{16N_0}\right)\left(\frac{2\pi}{\mu k_B T}\right)^{\frac{1}{2}}\frac{1}{K}\left(\frac{P_0}{P}\right)\left(\frac{T}{T_0}\right) \qquad \textbf{(Eq. 1.3.)}$$

where z is the ion charge state, e is the elementary charge, N_0 is the standard number density of the drift gas, μ is the reduced mass of the ion-drift gas system, k_B is the Boltzmann constant, T is temperature, K is the ion mobility (as defined by **Equations 1.1.** and **1.2.)**, P is the drift tube pressure, and P_0 and T_0 are the standard pressure and temperature, respectively.

The CCS is also referred to as the solution to a momentum-transfer integral between the ions of interest and the IM bath gas and is directly proportional to the t_d of the ions of interest as the t_d is inversely proportional to K. For non-DT based IMS instruments, calibrants are often employed to convert between t_d or arrival time distribution (ATD) and CCS as is the case most commonly with traveling wave-IMS (TWIMS) [39-41] and trapped-IMS (TIMS).[42, 43] For DTIMS, experimental strategies may also be employed to correct the arrival time of ions at the detector, t_A, to the t_d of ions in the DT separation. This can be accomplished through "1/V Plots" wherein the y-intercept of the correlation between arrival time and inverse drift tube potential gradient (ΔV) provides the t_0 used to correct arrival time for t_d as shown by **Equations 1.4** & **1.5** whereby reorganization of **Equation 1.2** then defines the slope of the correlation as the ratio of L^2/K which is independent of the DT potentials.

$$t_A = t_d + t_0 \quad \textbf{(Eq. 1.4.)}$$

$$t_A = \frac{L^2}{K} * \frac{1}{\Delta V} + t_0 \quad \textbf{(Eq. 1.5.)}$$

The experimental CCS values are often compared between experiments performed on the same and different IM instrument platforms as well as values calculated from available structures in the protein databank (PDB).[44] For many proteins and protein complexes, structures determined by x-ray crystallography, nuclear magnetic resonance spectroscopy, and cryogenic electron microscopy can be manipulated by molecular dynamics simulations to simulate the reorganization of secondary and tertiary structure elements upon transition into the less polar environment of the gas phase.[45] Following these changes, CCS values can be calculated from the structures using different methods including projection approximation (PA),[46] trajectory method (TM),[47] and exact hard-sphere scattering (EHSS),[48] and projection superposition approximation (PSA).[49-52] MOBCAL was one of the original packages used to calculate PA, TM, and EHSS CCS values of input structures;[47, 48] however, the program runs on Fortran 77 coding language and is not optimized for modern computing capabilities. Some combinations of these methods have been incorporated into more user-friendly software packages that often take advantage of multithreading and hardware acceleration to optimize calculation times, which is necessary for sampling theoretical CCS of large proteins and protein complexes.[53] Some of these programs include PSA, which reports both PA and PSA values for input structures from a publicly available webserver,[49-52] IMPACT, which quickly reports PA and an approximate TM value (called TJM*),[54] and Collidoscope,

which more efficiently calculates TM CCS values for large proteins and protein complexes.[55]

1.4. Ion Mobility-Mass Spectrometry

IMS is commonly combined with MS due to the duty cycle matching between IM separations which occur on the order of milliseconds and MS measurements which occur on the order of microseconds for quadrupole and time-of-flight (TOF) based mass analyzers. This duty cycle matching allows for multiple MS transients per IM experiment such that each datapoint across an IM scan is accompanied by a mass spectrum. For IM-MS experiments where the IM-MS duty cycles are mismatched, (e.g. IM-Orbitrap MS) dual ion gating regimes with Fourier Transform deconvolution have been employed for IM-MS experiments with high resolution in the mass and mobility domains.[12, 53, 56] An added benefit of IM-MS is the information of mass and charge required to calculate CCS is encoded directly in the MS data.

IM-MS instruments have been used to provide structural information on many classes of molecules ranging from peptides[3, 57, 58] and lipids[59-61] to membrane protein complexes[62-64] and protein chaperones.[65, 66] Native IM-MS (nIM-MS) methods allow for determination of CCS distributions with comparison to values calculated from available structures. These methods can provide important structural details that may be unavailable by traditional condensed phase techniques. Similarly to nMS, nIM-MS experiments aim to maintain low free energy of ions in the gas phase primarily by minimizing effects of collisional activation while maintaining ion transmission and sensitivity.[67] This allows for

CCS determination of noncovalent protein and protein-ligand complexes. By progressive, gas-phase collisional activation against a neutral background collision gas, these proteins and protein complexes can unfold resulting in collision-induced unfolding (CIU).[68] Plotting the ATD or CCS distributions as a function of an instrumental collision voltage or some lab-frame collision energy (E_{lab}), CIU heatmaps are generated.[69, 70] Further comparison of these heatmaps following ligand binding, point mutations, or other changes in solution content can then provide inferences regarding stabilization and/or destabilization of protein structure. Practical applications of CIU will be discussed in more detail in **Chapter 5**.

1.5. Instrumentation

1.5.1. Waters Synapt G2 (Q-TWIMS-TOF)

In **Chapter 2**, we apply methods developed for nIM-MS analysis of small, flexible proteins towards the topological analysis of fragile complexes formed through coordination-driven self-assembly (CDSA). CDSA reaction products are formed from self-organization of geometrically rigid structures typically capped with square planar platinum(II) (or palladium(II)) electron acceptors and rigid, electron-rich pyridyl electron donors.[71] By tuning the bonding angles of the rigid backbones between the Pt(II) or pyridyl acceptor or donor, polygons and polyhedra can be easily synthesized with structures similar to those shown in **Figure 1.4.**[72]

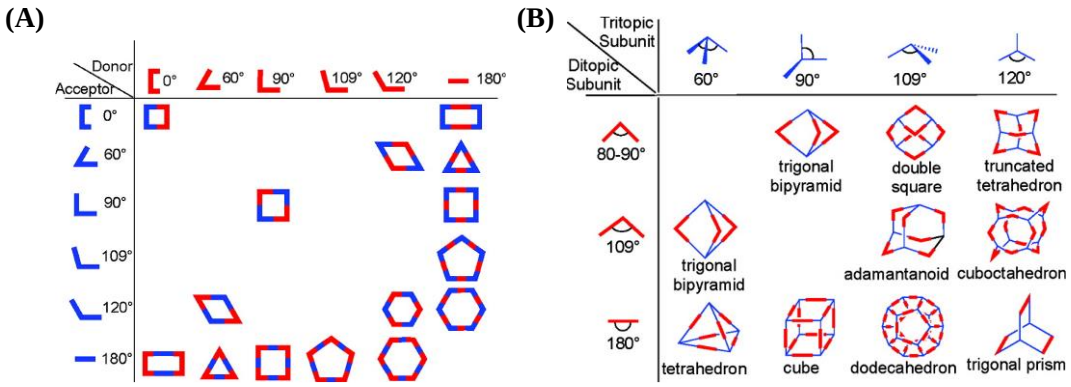

Figure 1.4. By tuning the bond angles between ditopic or tritopic donor and acceptor ligands, a host of (A) two-dimensional and (B) three-dimensional polyhedra can discretely self-assemble. Adapted with permission from *Chemical Reviews*, **2011**, *111*, 6810-6918. Copyright 2011 American Chemical Society.[72]

Because these structures are only held together with labile Pt—N bonds, nIM-MS analysis was able to preserve the intact reaction product complexes and provide evidence that anionic adducts to the intact cationic CDSA complexes provide for gas-phase stabilization against collision-induced dissociation. These IM-MS experiments were performed using a Waters Synapt G2 shown in **Figure 1.5**. Some unique features of this instrument include a pre-IM quadrupole (Q) MS for mass selection prior to IM analysis. Between the Q and IMS regions, there is a trap region that allows for pre-IM CA of ions for CIU experiments by varying the trap collision voltage. Because of these design factors, the Waters Synapt instrument line has been the prominent instrument platform for performing CIU experiments. Following the trap region is the TWIMS device. TWIMS provides IM separation through application of a sinusoidal DC voltage and a confining RF voltage to the stacked ring ion guide.[73, 74] The RF voltage works to radially confine ions to the TWIMS device while the sinusoidal DC voltage provides a traveling wave.

Separation occurs as ions with high mobility will be pushed by the wave while ions with low mobility will roll over the wave. Due to the nonuniformity of the electric fields used, external calibrants are required to determine CCS.[39] Following TWIMS separation, ions can be collisionally activated in the post-IM trap region prior to MS analysis on the orthogonal-acceleration time-of-flight (TOF) mass analyzer.

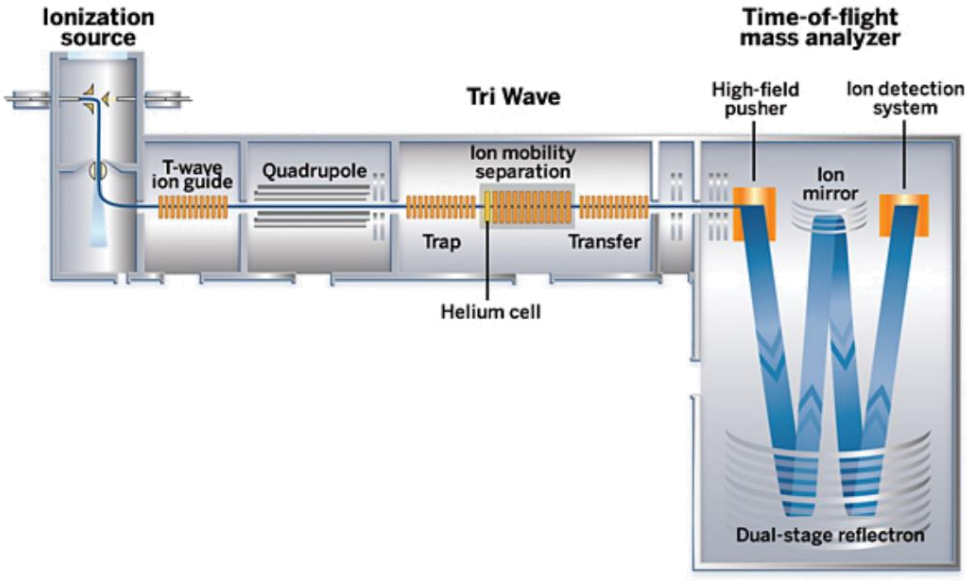

Figure 1.5. A schematic view of the Waters Synapt G2 show the overall layout of quadrupole (Q), TriWave, and orthogonal acceleration time-of-flight (oa-TOF) mass analyzer. TriWave device incorporates a pre-IM trap and post-IM transfer regions for optional collisional activation and a pre-IM helium cell for collisional cooling of ions prior to entry into the TWIMS device. Adapted from Waters Overview and Maintenance Guide.

1.5.2. Agilent 6545XT (Q-TOF MS)

For nMS analysis of large proteins and protein complexes, instruments with high-mass capabilities are needed. The Agilent 6545XT (shown in **Figure 1.6**) is a Q-TOF mass spectrometer with advanced hardware capabilities for acquisition of up to 30,000 m/z. A unique feature of this instrument is its upgraded TOF mass analyzer that was built longer

and operated at lower pressures (low 10^{-8} Torr) compared to other Agilent Q-TOF MS instruments to improve mass resolution and sensitivity. The source ion optics are primarily designed for fast polarity switching for simultaneous LC-MS acquisition in positive and negative ion polarities using a resistively coated borosilicate ion transfer capillary. While these optics are not specifically designed for nMS, the Agilent NanoSpray source was adapted for static nESI for the analysis of soluble and membrane protein complexes and the protein chaperonin, GroEL. Collision-induced dissociation (CID) of the native GroEL 14-mer ions produces signals up to ~22,000 *m/z* corresponding to the charge-stripped 13-mer ions. These results are discussed in further detail in **Chapter 3**.

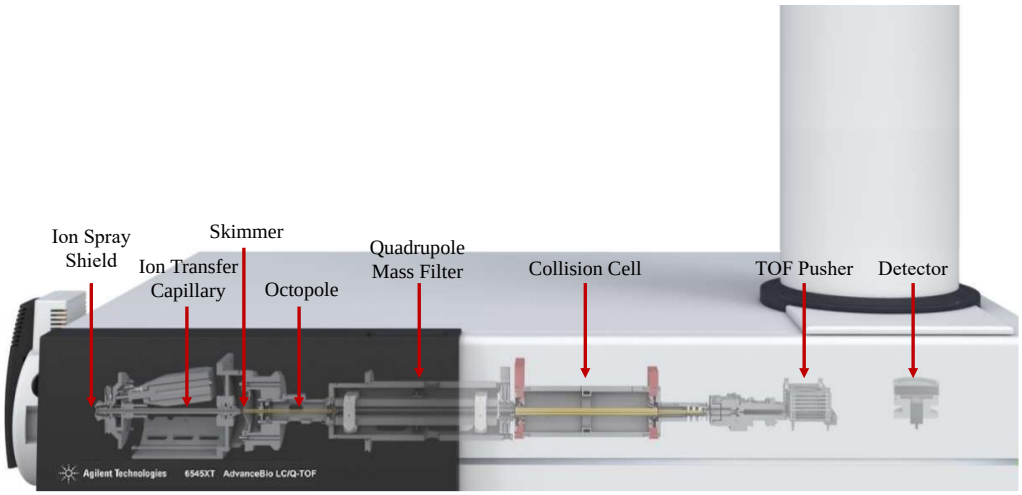

Figure 1.6. Schematic diagram of the Agilent 6545XT shows the general Q-TOF design of the instrument. This instrument was designed for advanced capabilities including high mass acquisition (up to *m/z* 30,000) with enhanced mass resolution from a longer TOF mass analyzer operating at lower pressures (*ca.* 10^{-8} Torr). Adapted from Agilent website.

1.5.3. Thermo UHMR (Q-Orbitrap MS)

Advances in high-resolution mass analysis continuously push the limits of resolving smaller and smaller mass shifts on larger and larger ions. The Q Exactive UHMR

is a quadrupole-Orbitrap mass spectrometer from Thermo Fisher Scientific with state-of-the-art capabilities including ultra-high mass range, high sensitivity, and available high resolution mass acquisition. The design changes towards development of this instrument were also realized with nMS capabilities in mind by reducing RF voltage frequencies to improve ion transmission at high *m/z* and implementing in-source trapping (IST) of ions to enhance desolvation of large ions prior to MS analysis. A schematic diagram of the UHMR is provided in **Figure 1.7**.

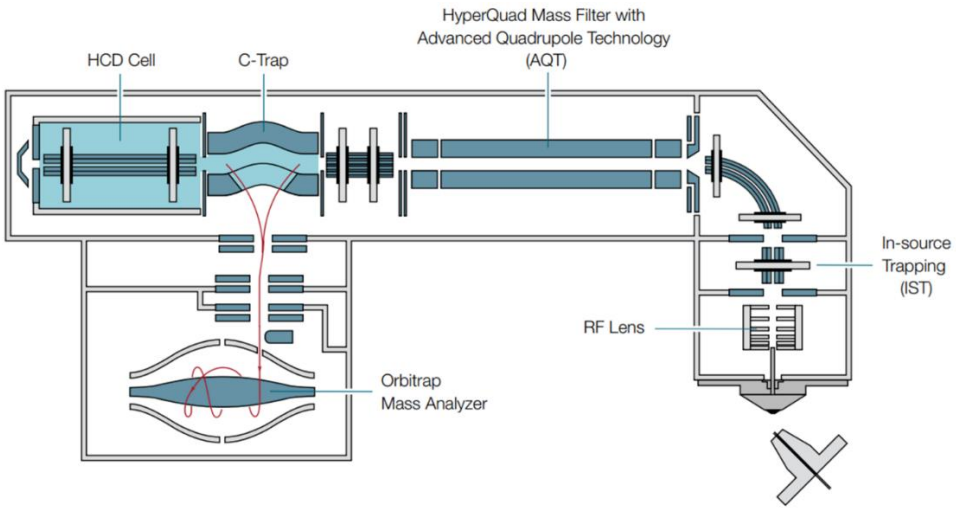

Figure 1.7. Schematic diagram of the Thermo Fisher Scientific UHMR Q-Orbitrap mass spectrometer. In-source trapping (IST) provides more efficient desolvation in the source region. Adapted from the Thermo Fisher website.

Enhanced desolvation and high mass resolution capabilities of this instrument were used to identify and further probe mass heterogeneity observed on a native, intact monoclonal antibody (mAb) in **Chapter 4**. mAbs are becoming ubiquitous research target to study their structure and function related to viral disease mechanisms and treatments as well as development of antibody-drug conjugates (ADCs) for biotherapeutic

applications.[75] IgG1 is the most abundant antibody in human serum, and its structure is described in further detail in **Chapter 4**. The structural heterogeneity of mAbs results from two primary factors: (i) *N*-glycan heterogeneity and (ii) sequence variants in complementarity-determining regions (CDRs) that allow for highly specific antigen binding.

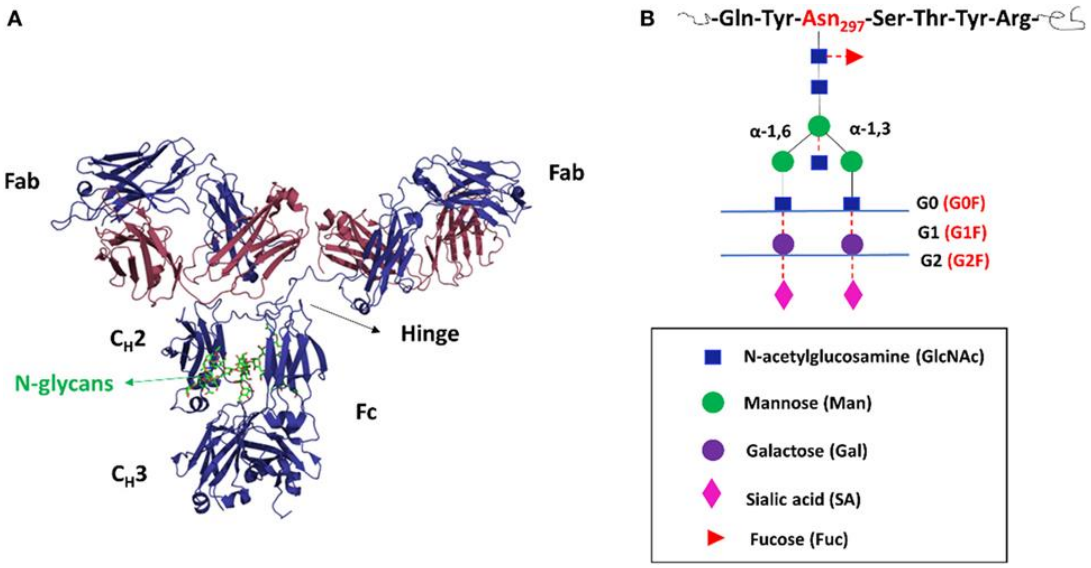

Figure 1.8. (A) Immunoglobulin gamma (IgG) antibodies consist of two heavy chains (blue) and two light chains (red) connected with disulfide bonds. The structure is shown highlighting the antigen binding fragment (Fab) domains, crystallizable fragment (Fc) domains, hinge region. N-linked glycans are bound to each heavy chain (blue) and generally buried in the Fc domain. (B) Glycan structure is often depicted as cartoon drawings to simplify the structure with variability in the glycan residue size and heterogeneity typically depicted as G0F, G1F, G2F for each heavy chain. Figure from *Frontiers in Immunology*, **2017**, *8*,1-15. Copyright 2017 Li *et al.* Open-Access License.[76]

N-linked glycans on IgG mAbs are attached on the amide nitrogen atom of an asparagine residue around position 300 of each heavy chain; however, they can be found on any glycosylated protein containing the Asn-X-Ser/Thr tripeptide sequence where X is any amino acid except Pro. The biosynthesis of N-glycans is governed by highly specific

enzymatic processes in the endoplasmic reticulum and Golgi *in vivo*.[77] The resulting glycosylated IgG mAbs will then contain N-glycans bound to each heavy chain in the crystallizable fragment (Fc) domain with varying structures highlighted in **Figure 1.8**.[76] For human IgGs, differences in truncation or clipping of the N-glycan residues leads to 36 possible structures. Human IgG1 mAbs are typically observed with G0F, G1F, and G2F residues on each heavy chain, annotated as a series of G0F/G0F, G0F/G1F, G1F/G1F (or G0F/G2F), G1F/G2F, and G2F/G2F glycan structures. These glycans each differ by one galactose (Gal) residue with mass shifts of 162 Da. Moderately high mass resolution is needed to achieve baseline resolution of these mass differences on an intact mAb of *ca.* 148 kDa. For smaller mass differences of ~40 Da on intact glycosylated IgG1 mass signals as observed and described in **Chapter 4**, the high mass resolution capabilities of the UHMR are required.

1.5.4. Agilent 6560 (DTIMS-Q-TOF)

The Agilent 6560 IMS-Q-TOF is the only commercially available IM-MS instrument equipped with a uniform field DT for first-principles CCS determination without the need for external CCS calibrants. A schematic of the instrument is provided in **Figure 1.9**. Following ESI, ions are pneumatically focused through the ion transfer capillary into the high-pressure front funnel region. The front funnel focuses ions into the trapping funnel where ions are accumulated and then pulsed into the drift tube with controllable trap fill and trap release times. Following IM separation in the DT, ions are refocused in the post-IM rear funnel prior to transfer into the quadrupole mass filter,

collision cell, and TOF mass analyzer. In this instrument, the time spent outside the drift tube prior to detection (identified as t_0 in **Equations 1.4** and **1.5**) accounts for the time ions spend transiting through these post-IM ion optics.

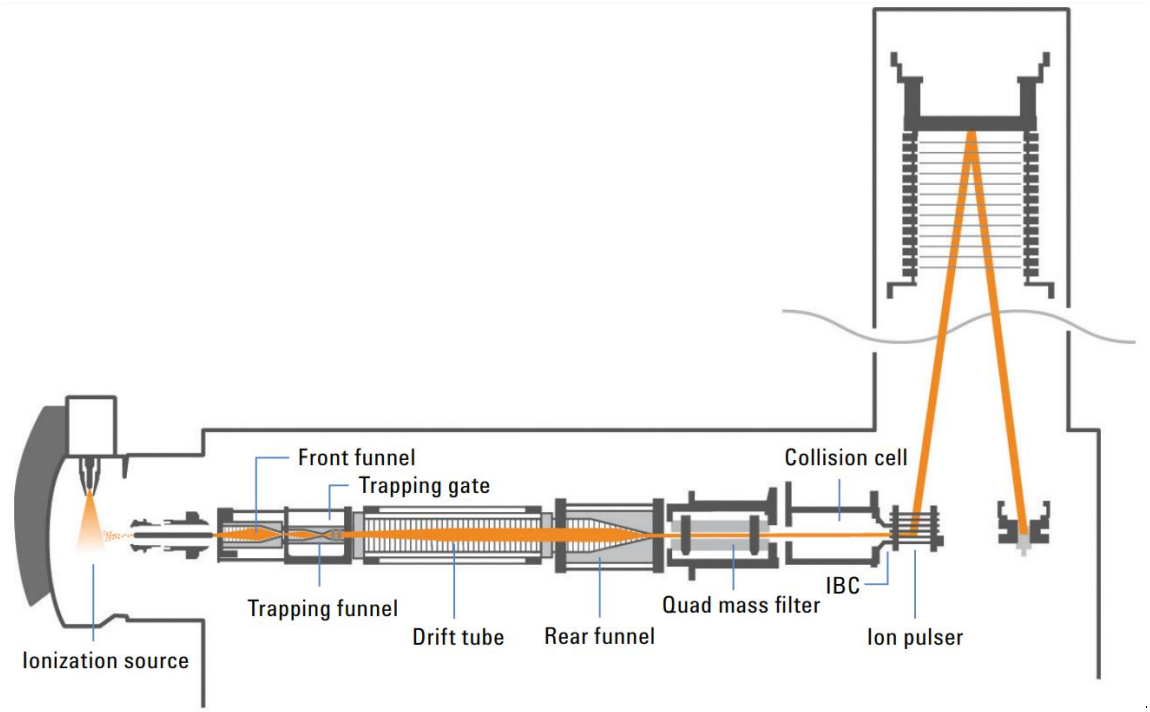

Figure 1.9. Schematics of the Agilent 6560 DTIMS-Q-TOF. For collision-induced unfolding experiments, ions are activated in a lens placed at the end of the ion transfer capillary prior to entry into the high-pressure front funnel. Adapted from Agilent website.

Because of the uniform field DT in this instrument, first-principles CCS determinations can be performed following correlation of ion ATDs with the inverse of the DT potential. Because the different DT fields must be scanned for the multiple-field CCS determination, these methods are largely unsuitable for temporally-limited scans, such as those performed in conjunction with LC-MS, where the timescale of acquisition

does not allow for acquisition across multiple DT E fields. As a solution, single-field CCS calibration strategies using Agilent TuneMix ions have been established.[78]

This instrument is equipped with upgraded firmware for acquisition up to 20,000 *m/z* and upgraded prototype desolvation assembly to facilitate CIU of proteins and protein complexes between the end of the ion transfer capillary and the entrance to the high-pressure front funnel as highlighted in **Chapter 5**. In this region, ions are accelerated into the high-pressure front funnel (set at 4.5 to 4.8 Torr) with a tunable "in-source collision energy" potential. Increasing this potential leads to increasing CIU as observed by increases in ATD and CCS distributions.

2. TOPOLOGICAL CHARACTERIZATION OF COORDINATION-DRIVEN SELF-ASSEMBLY COMPLEXES: APPLICATIONS OF ION MOBILITY-MASS SPECTROMETRY*

2.1. Introduction

Self-assembly (SA) allows the spontaneous formation of ordered systems at all scales from the organization of weather systems to the formation of molecular crystals.[79] A subclass of SA reactions includes coordination-driven self-assembly (CDSA) reactions which form highly selective complexes through the coordination of nitrogen-containing, donor ligands and metal-containing acceptor ligands.[80] Pioneering work from Lehn,[81-83] Stang,[71, 84-86] Fujita,[87-89] Wesdemiotis,[90-92] and others has driven the design, synthesis, and characterization of a variety of CDSA reaction products. CDSA reaction products have been designed for use as catalysts, chemical sensors, drug transporters, and theranostic agents with recent success.[84, 86, 93-97] However, their characterization is complicated by overlapping signals of precursor and product signals in NMR spectroscopic measurements, and CDSA products can be difficult to crystallize due to intrinsic physicochemical properties, such as void space. Additionally, their weak coordinating bonding networks are intrinsically dynamic in structure, and thus greatly benefit from characterization techniques that can measure condensed-phase structures or conformers.[79]

---

* Reprinted with permission from Mallis, C.S.; Saha, M.L.; Stang, P.J.; Russell, D.H. Topological Characterization of Coordination-Driven Self-Assembly Complexes: Applications of Ion Mobility-Mass Spectrometry. *Journal of the American Society for Mass Spectrometry*, **2019**, *30*, 1654-1662.

Mass spectrometry (MS) and ion mobility-mass spectrometry (IM-MS) have been used to characterize intact supramolecular ions with the measured masses and gas-phase conformers related back to solution chemistry and crystal structures.[98-100] The high mass resolution afforded by modern mass spectrometers provides accurate determination of elemental composition from nominal masses and correlation of complex isotopic distributions to the identity and number of metal centers in organometallic ions.[101] Specifically, IM provides an orthogonal separation of gas-phase ions based on their size-to-charge ratio and allows for determination of ion-neutral collision cross sections (CCS) from which conformational or structural information can be interpreted.[102, 103] Drift tube based IM instruments separate ions based on size-to-charge ratio as they are transported by an electrostatic field filled with a buffer gas (typically helium or nitrogen). The traveling wave-based IM instrumentation uses a set of stacked ring ion guides to superimpose a traveling wave over the radio-frequency ion guide, wherein small ions travel with the wave and larger ions roll over the wave. Additionally, IM can separate isobaric ions which have overlapping *m/z* signals, yet different elemental compositions. Due to the high rotational symmetry of many CDSA product ions, the gas-phase dissociation of intact complexes will often produce isobaric ions as both the mass and charge of the ions are reduced by the same factor.

Wesdemiotis and coworkers used traveling wave IM-MS to separate and identify isobaric reaction and dissociative product ions of several metallated terpyridine macrocyclic complexes and have identified cyclic and linear gas-phase conformers.[90-92] Brocker *et al.* demonstrated that supramolecular square, triangle, and triangular prism

structures can be characterized by IM-MS with their CCS agreeing well reported crystal structures; however, their mass spectra contain a host of identified fragment ions.[104] While these results are promising, the reported MS show a host of fragments, multiple charge states, and there is limited discussion on the effects of improper instrument tuning on the observed IM-MS spectra.

While IM-MS has demonstrated ability to observe gas-phase conformers of a range of biomolecular ions (*viz.* peptides, proteins, protein complexes, etc.), recent literature suggests that the sampling conditions (i.e. instrument tune settings) can greatly affect the sampled conformation space.[21, 26, 105, 106] Here, we show that by properly tuning an IM-MS instrument, intact ions having low internal energies and minimal anion binding can be observed by IM-MS in high relative abundances. Additionally, collision-induced dissociation (CID) of the observed intact product ions reveals the topology of the rhomboid products and suggests that anionic adducts provide for Coulombic stabilization of self-assembly products in the gas phase.

2.2. Methods

2.2.1. Sample Preparation

The Pt-based precursor **1** and pyridine-based precursor **2** (1,3-bis(pyridin-4-ylethynyl)benzene) were dissolved separately in HPLC-grade acetone (EMD Chemicals, NJ, USA) and mixed to a final product concentration of ~50 μM prior to being loaded into borosilicate capillary tips (~20 μm O.D.). A platinum wire was placed in contact with the solution inside the glass capillary to facilitate electrospray.

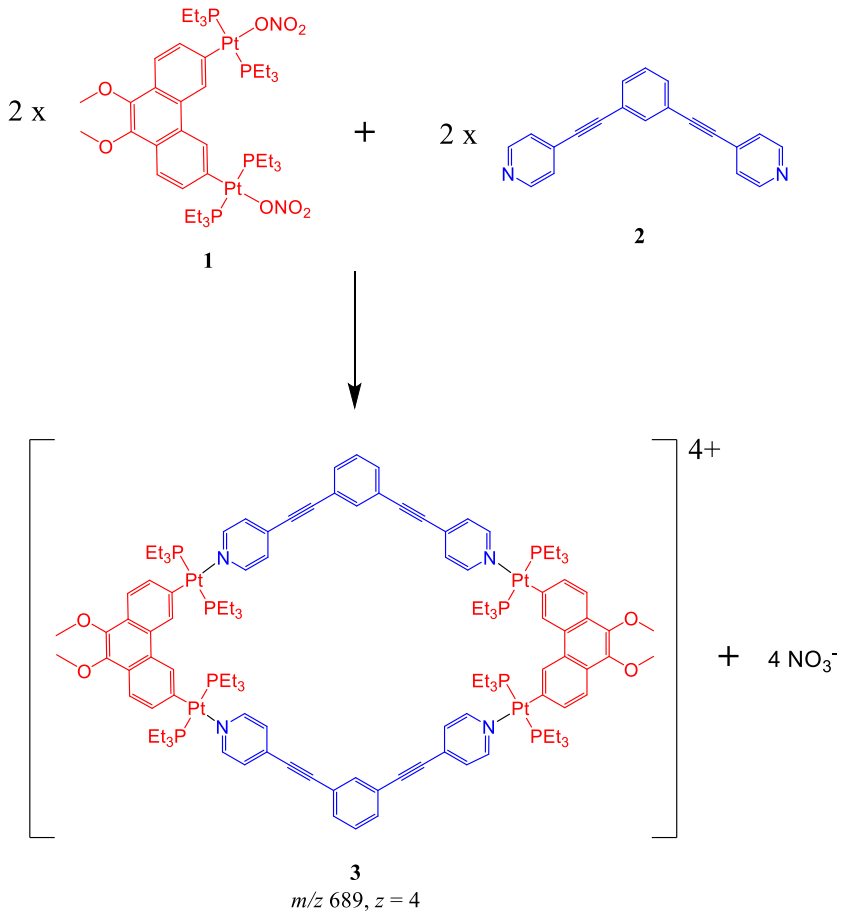

Figure 2.1. Solution mixing of precursors **1** and **2** in acetone solutions at room temperature results in the formation of the charged rhomboid ion **3** with four nitrate counterions.

2.2.2. Ion Mobility-Mass Spectrometry

The Waters Synapt G2 (Manchester, UK) was operated in the positive mode as a nESI-Q-TWIMS-TOF and has been described in detail elsewhere.[107] Briefly, after nanoelectrospray ionization (nESI), the ions generated can be mass selected in the quadrupole (Q), collisionally activated in the trap region prior to mobility separation, separated in the traveling wave ion mobility (TWIM) cell, and finally analyzed with the time-of-flight (TOF) mass analyzer. The IMS operates with three regions: trap, IMS, and transfer with a helium cell located between the trap and IMS regions. For pre-IMS CID

experiments, ions are mass selected in the Q and collisionally activated in the trap region. Capillary voltages were set to ~1.3 kV. For instrument tuning and CID experiments, traveling wave height was set to 10 V, wave velocity was set to 200 m/s, and IM nitrogen flow rate was set to 50 mL/min. These settings provided the greatest relative abundance of intact rhomboid ions **3** relative to dissociation product ions as shown in **Figures 2.2 and 2.3**.

Mass spectra were externally calibrated with sodium iodide. In all experiments the source temperature was set to 100 °C. The trap DC was manually controlled (Entrance: 0V; Bias: 40 V; DC: 0 V; Exit: -10 V). The IMS DC was manually controlled (Entrance: 35 V; DC: 5 V; Exit: -5 V; Bias: 3 V; Exit: 0 V). For CID experiments, the approximate centroid of the *m/z* packet was selected with a low mass resolution of 15 for both experiments.

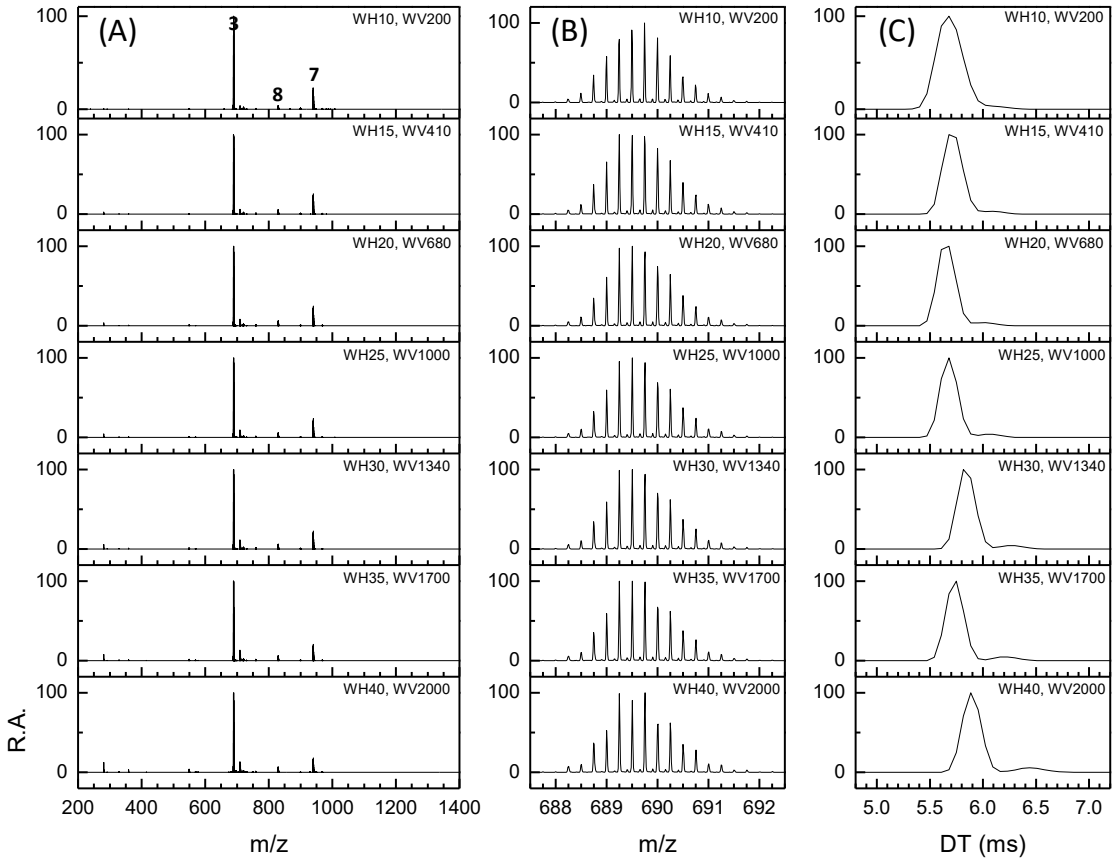

Figure 2.2. The wave heights (WH, units V) were increased in 5 V increments with the wave velocity (WV, units m/s) increased accordingly such that the ion velocity in the drift cell of **3** does not change significantly. (A) MS do not show significant differences in ion abundances as the wave settings are changed. (B) The isotopic distribution of the *m/z* range of the rhomboid, **3**, does not change significantly and still is dominated by the intact rhomboid ion (**3**, 4+ charge) rather than the 2+ charge half-rhomboid ion fragment (**4**, 2+ charge). (C) In this experiment, the wave heights and velocities were changed such that the drift time of the main reaction product **3** (*m/z* 689 remains constant with a drift time of ~5.9 ms. The IMS nitrogen flow rate was set 45 mL/min in each MS.

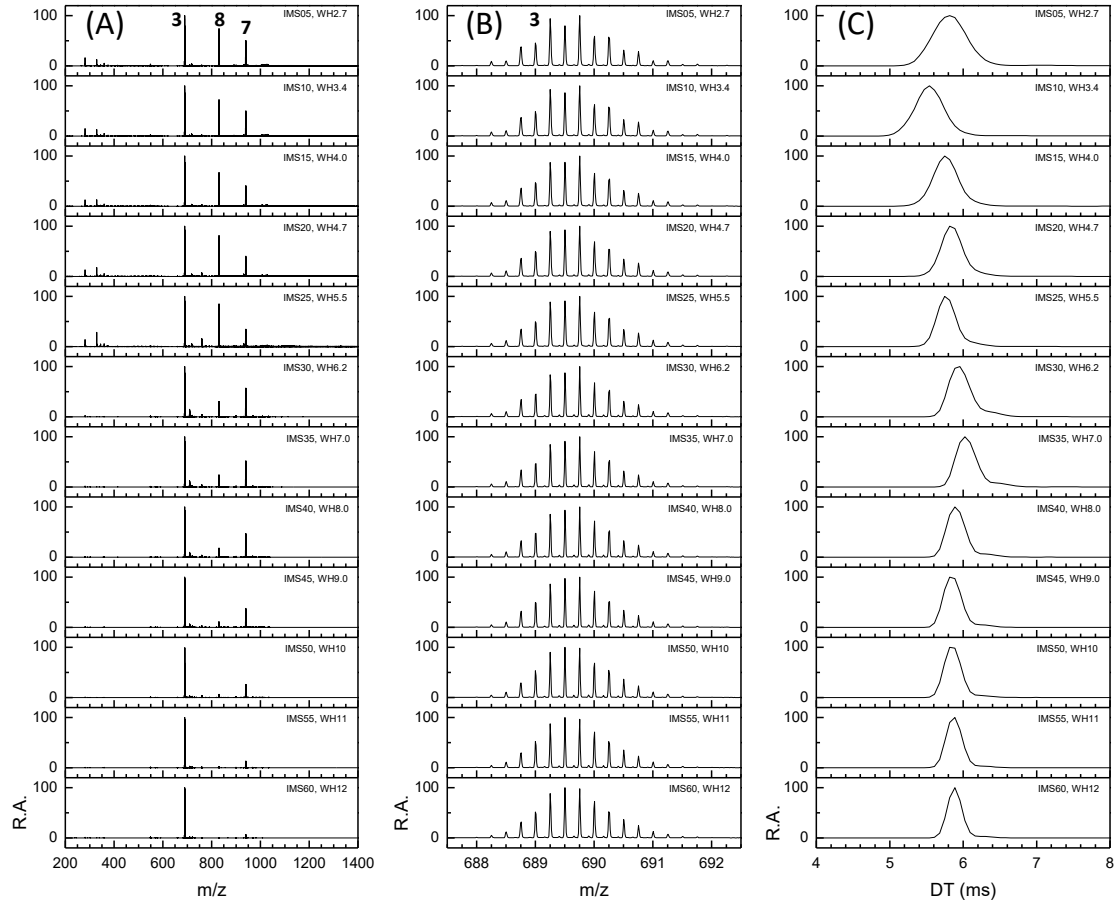

Figure 2.3. Nitrogen flow rates into the IMS cell (IMS, units mL/min) were increased in 5 mL/min increments and traveling wave heights (WH, units V) were varied at constant wave velocity (200 m/s) while maintaining constant ion velocity of the intact rhomboid ion, **3**. (A) Mass spectra show increased relative abundances of the of the nitrate-adducted rhomboid ion, **7**, and its fragment, **8**, as the IMS flow rate decreases. (B) The isotope distribution of the intact rhomboid, **3**, shows very minimal fragmentation to a half-rhomboid, **4**, as the dominant charge state of the isotopic distribution remains 4+ throughout the experiment. (C) As the IMS flow rates and traveling wave heights are changed, the drift time of the intact rhomboid ion, **3**, remains ~5.9 ms. In all MS, WV was set to 200 m/s.

Following instrument tuning methods similar to those published on ubiquitin and metallothionein for reducing the effective temperature of ions,[26] a tuning grid was developed to study the effects of instrument tuning on the observed MS (**Figure 2.4**).

Select MS spectra are shown in **Figure 2.8**. Additionally, observed fragmentation pathways for the rhomboid and nitrate-adducted rhomboid ions are shown in **Figure 2.5** to label the identified ions. After tuning optimization, CID experiments were performed on the nitrate-free (**3**) and nitrate-adducted (**7**) rhomboid ions by mass selecting them in the quadrupole and increasing the collision voltage (CV) in the trap region up to a maximum of 40 V. The MS results of these CID experiments are presented in **Figure 2.9**.

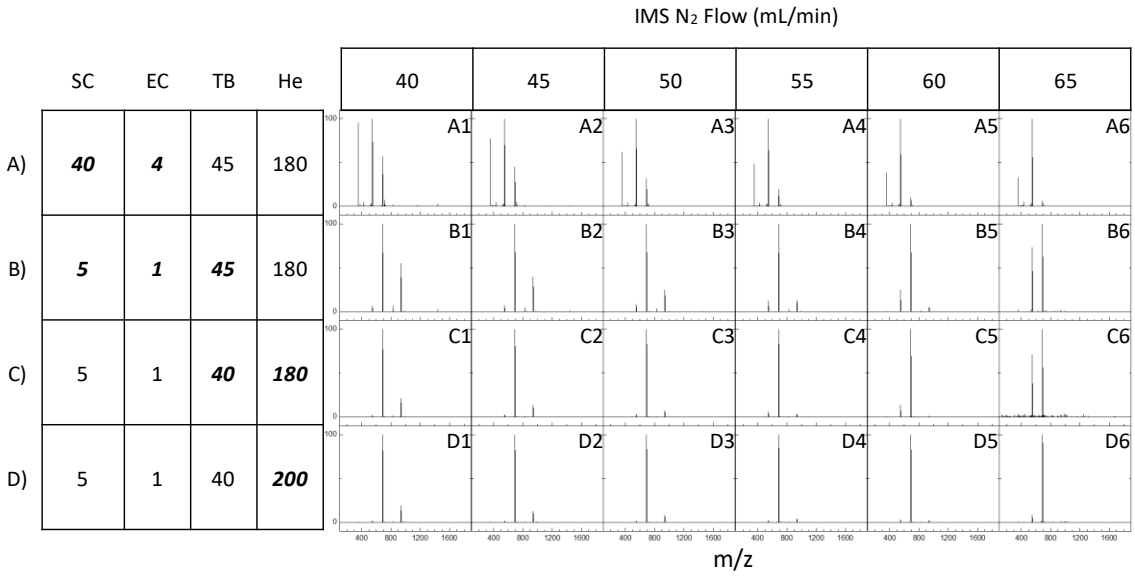

Figure 2.4. Mass spectra were taken after adjusting the source cone voltage (SC), extraction cone voltage (EC), trap bias voltage (TB), helium cell flow rate (He), and IMS N_2 flow rates (labeled). This tuning grid was used to observe specific effects of lowering the source voltages (A to B) to reduce effects of in-source dissociation. Reduction of the trap bias voltage (B to C) shows decreased relative abundances of observed fragment ions. Increasing the helium flow rate results in decreased relative abundance of the nitrate-free fragment ion (4, *m/z* 549). Additionally, at lower helium flow rates, increasing the IMS flow rate leads to increased abundance of the *m/z* 549 fragment ion.

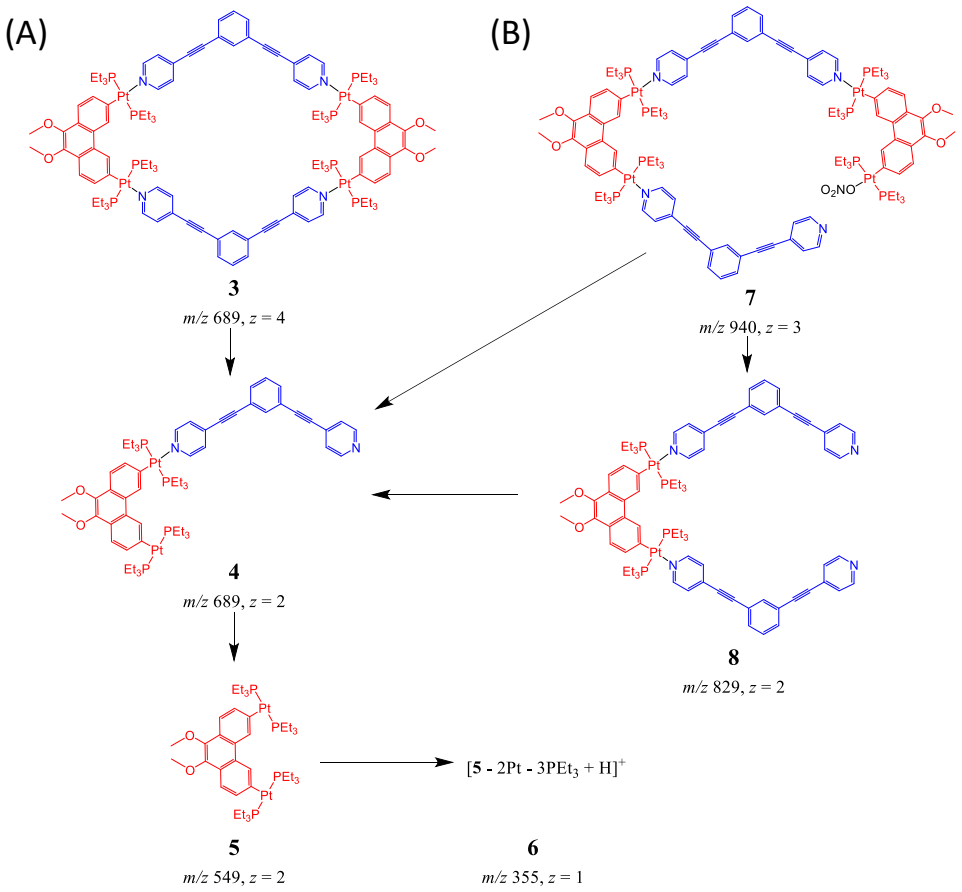

Figure 2.5. General structures, *m/z*, and charge state (*z*) of ions identified in the mass spectra resulting from CID of (A) the nitrate-free rhomboid **3** and (B) the nitrate-adducted rhomboid **7**.

Due to the non-uniform electric field applied along the mobility device, external calibrant ions are required to convert an experimental traveling wave-based ATD to a rotationally-averaged CCS. While CCS calibrants have been developed for proteins and polymers,[39, 40, 108] none have been developed for the ions studied herein. Therefore, IM ATDs were not converted to CCSs.

2.2.3. Data Processing and Relative Abundance Determination

IM-MS data were initially extracted using MassLynx 4.1 (Waters Corporation, Manchester, UK). Gaussian peak fitting of select IM spectra was performed using Origin 8 (OriginLab Corporation, Northampton, MA). Theoretical MS isotope distributions were calculated with ChemCalc.[109] Comparisons of experimental and theoretical isotopic distributions are included **Figure 2.6**. Theoretical masses of the products identified in **Figures 2.1 & 2.5** are provided in **Table 2.1**.

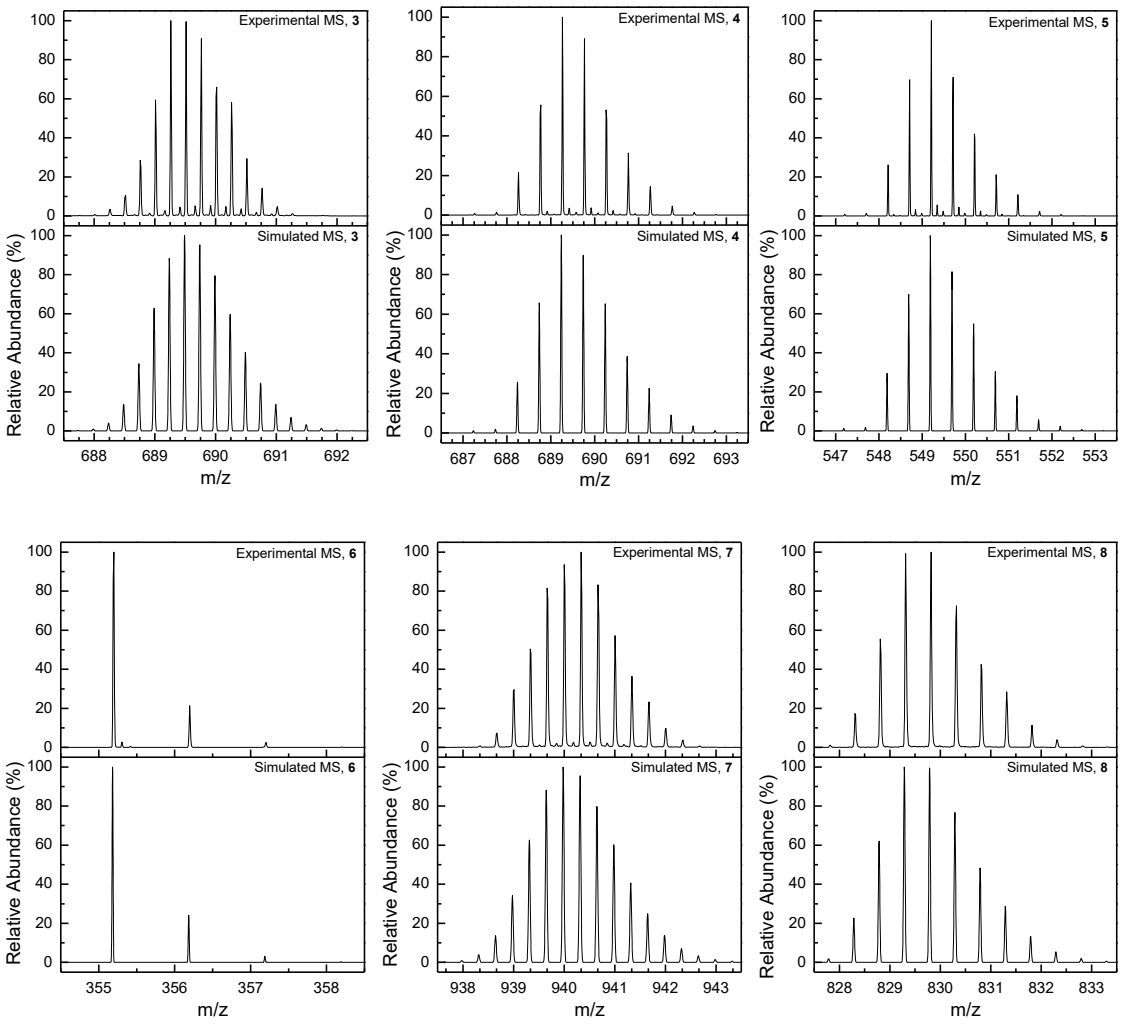

Figure 2.6. Comparisons of experimental MS to simulated MS (ChemCalc, $R_{m/z}$ = 25,000) for the identified ions.

Table 2.1. A summary of precursor molecules (**1** – **2**), reaction product ions (**3**, **7**), and fragmentation/dissociation product ions (**4** – **6**, **8**) along with their average molecular weight, monoisotopic mass and monoisotopic *m/z*.

ID	Structural Formula	Chemical Formula	Molecular Weight	Monoisotopic Mass	Charge	Monoisotopic m/z
1	((Pt(PEt3)2)2C16H12O2)(NO3)2	$C_{40}H_{72}N_2O_8P_4Pt_2$	1223.060	1222.353	0	N/A
2	(C20H12N2)	$C_{20}H_{12}N_2$	280.323	280.100	0	N/A
3	(Pt2(PEt3)4C16H12O2)2(C20H12N2)2(4+)	$C_{120}H_{168}N_4O_4P_8Pt_4^{+4}$	2758.748	2756.956	4	689.238
4	(Pt2(PEt3)4C16H12O2)(C20H12N2)(2+)	$C_{60}H_{84}N_2O_2P_4Pt_2^{+2}$	1379.374	1378.478	2	689.238
5	(Pt2(PEt3)4C16H12O2)(2+)	$C_{40}H_{72}O_2P_4Pt_2^{+2}$	1099.051	1098.378	2	549.188
6	(C16O2H12)PEt3H(+)	$C_{22}H_{28}O_2P^{+1}$	355.431	355.183	1	355.182
7	(Pt2(PEt3)4C16H12O2)2(C20H12N2)2(NO3)(3+)	$C_{120}H_{168}N_5O_7P_8Pt_4^{+3}$	2820.753	2818.944	3	939.647
8	(Pt2(PEt3)4C16H12O2)(C20H12N2)2(2+)	$C_{80}H_{96}N_4O_2P_4Pt_2^{+2}$	1659.697	1658.578	2	829.288

Determination of relative ion abundances was performed using the IM data rather than the MS data. Relative IM abundances (RA_{IM}) were calculated as the ratio of the Gaussian peak fit area of identified ions to the total integrated area of the IM spectra. For example, an RA_{IM} of 50% would indicate that half of the total ion signal is found under the Gaussian fit of an identified ion. These steps are necessary due to the overlapping signals in the mass spectra of the full (**3**) and half-rhomboid (**4**) ions. In this way, the relative abundances of isobaric ions can be quantified for the processing of CID data. A visual explanation of the RA_{IM} determination is provided in **Figure 2.7**.

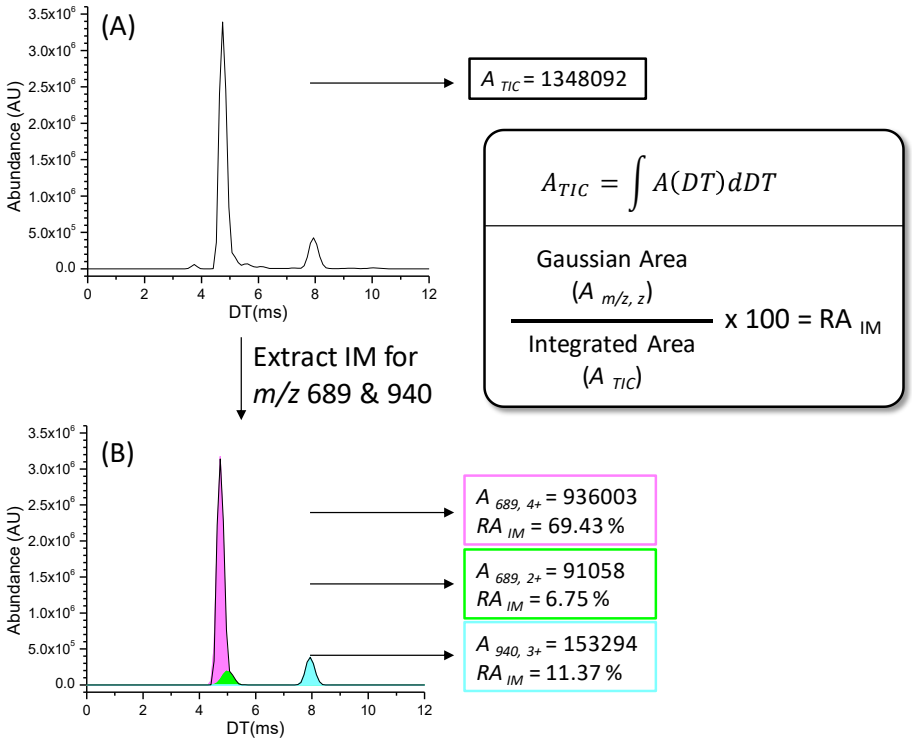

Figure 2.7. Mathematical extraction of ion abundances using IM data allows for the calculation of relative abundance of isobaric ions, like the *m/z* 689, 2+ and 4+ ions (corresponding to the full rhomboid and half rhomboid complexes, respectively). (A) Integration of the IM spectrum allows for the calculation of the total ion current abundance area (A_{TIC}). (B) Extraction of the Gaussian fit areas of the mass selected IM spectra of identified ions is correlated to ion abundance, and relative abundance can be calculated by dividing the Gaussian area by the integrated area of the full IM spectrum.

2.3. Results

2.3.1. Supramolecular Rhomboid Product Ions

The combination of the 60° bite angle between the square planar Pt(II) acceptors of precursor **1** and the 120° difference between the pyridine donor ligands of precursor **2** (See **Figure 2.1)** yields the CDSA of a molecular ion with a rhomboidal supramolecular shape and an overall charge of 4+ (ion **3**, *m/z* 689) from loss of four nitrate anions (two from each precursor **1**). Lower charge ions are formed from adduction of counterions in

solution, as is observed with the nitrate-adducted rhomboid ion, with an overall charge of 3+ (ion **7**, *m/z* 940). For clarity, ions resulting from gas-phase dissociation or fragmentation are identified in **Figure 2.5**.

2.3.2. Reduction of Ion Internal Energies

To observe intact, solution-phase ion structures in the gas phase by IM-MS, the internal energy of the ions must remain below their respective dissociation thresholds. Default instrument tuning parameters promote high transmission of ions; however, these instrument conditions result in ions identified as products of dissociation and fragmentation of intact ions formed in solution. The ion with the highest relative abundance under these default conditions is identified as the nitrate-free analogue to the bis-Pt(II) precursor ion, **5** (*m/z* 549) (**Figure 2.8A**). Effects of in-source activation and dissociation are mitigated by reduction of source potentials including the source and extraction cones (**Figure 2.8B**) where the relative abundance of the nitrate-free rhomboid **3** as well as the half-rhomboid **4** are observed in higher relative abundance. Finally, progressive tuning was completed by reduction of the trap bias potentials, increasing the flow to the pre-IM helium cell, and reducing the nitrogen flow to the IM cell (**Figure 2.8C**). The finalized instrument parameters were selected to promote transmission of the intact nitrate-free and nitrate-adducted rhomboid ions (**3** & **7**, respectively) as the most abundant ions. A larger grid of instrument tuning parameters is available in **Figure 2.4**.

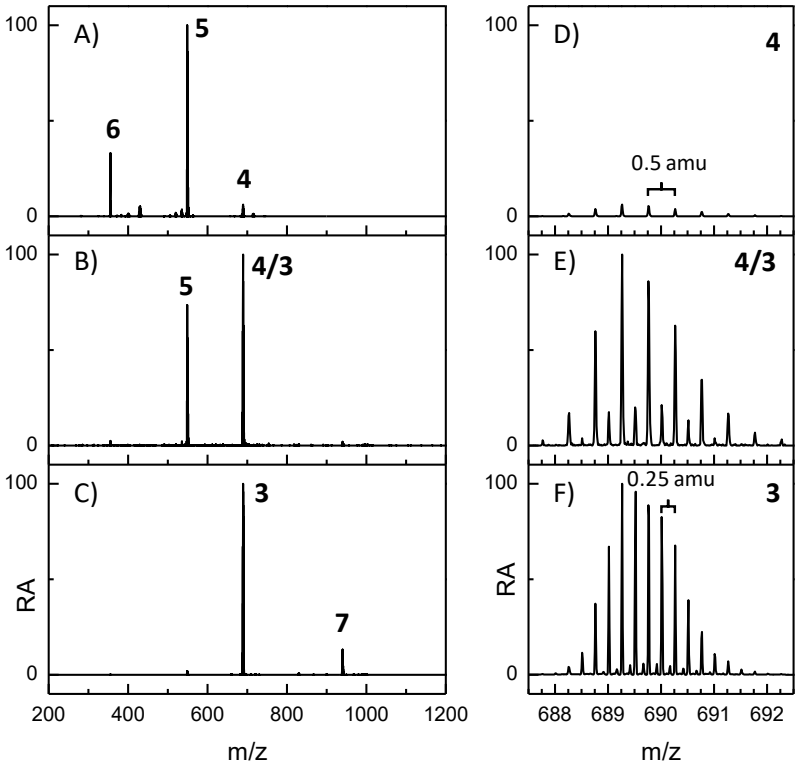

Figure 2.8. The effects of instrument tuning on the observed mass spectra. (A) Dissociation products dominate the mass spectrum under default tuning conditions. (B) Reduction of the source and extraction cone potentials reveals some intact rhomboid 4 in low relative abundance. (C) Reduction of the trap bias voltage, increasing the helium cell flow, and decreasing the IM nitrogen flow rates show the rhomboid ions **3** & **7** with the largest relative abundances. (D-F) Expansion of the mass spectrum around *m/z* 690 of A-C, respectively, reveals the isobaric mass spectrum of the half-rhomboid ions (**4**, $z = 2$) and intact rhomboid ions (**3**, $z = 4$) with isotopic spacings of 0.5 and 0.25 amu, respectively.

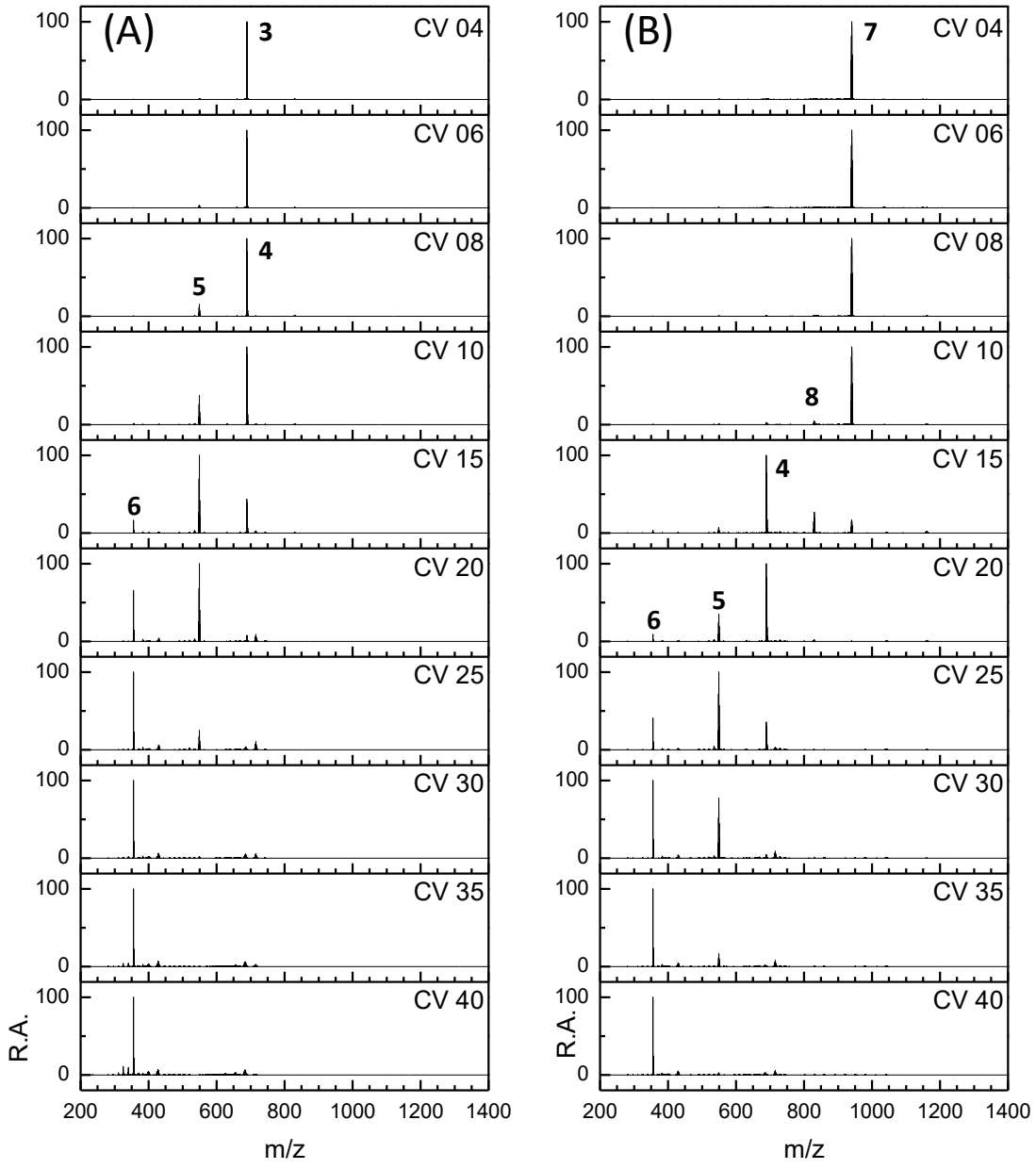

Figure 2.9. MS from the CID of the (A) intact rhomboid, **3**, and the (B) nitrate-adducted rhomboid, **4**, with trap collision voltages labeled. The IM data for the ions identified by MS were used in Figures. 3 & 4 (main text).

One of the problems with mass spectral characterization of many coordination-driven self-assembly products is the high degree of rotational symmetry of the reaction

products. As a result, collisional activation of intact ions can lead to loss of mass and charge such that the *m/z* of the precursor and product ions are the same. IM is implemented as an orthogonal separation tool for these isobaric ions, where the conformational heterogeneity of all ions can be observed, and the relative abundances of isobaric ions can be determined.

Secondary tuning of the IM separation conditions was performed by changing the traveling wave height and wave velocity while maintaining constant drift times of the rhomboid ion, **3** (*m/z* 689) (**Figure 2.2**). Others have noted that increasing wave height leads to narrowing of IM peak widths and increasing wave velocity leads to widening of mobility peak widths.[110] To maintain constant ion drift times, both the wave heights and velocities must increase (or decrease). As a result, the observed changes in peak widths are minimal as relative increase and decrease in peak widths effectively cancel each other.

2.3.3. Collision-Induced Dissociation of Intact Complexes

Collision-induced dissociation (CID) of the observed rhomboid complexes (nitrate-free rhomboid, **3**, and nitrate-adducted rhomboid, **7**) was performed to confirm topology of the reaction products. CID was accomplished through mass selection of the precursor ions of interest, collisional activation in the pre-IM trap region with increasing collision voltages (CV), separation in the TWIMS cell, then mass analysis of observed dissociative or fragmentation products in the TOF. Relative abundances of the identified products were determined using the previously described methods and are shown in **Figure 2.10A & 2.10B** and dissociation pathways are presented in **Figure 2.5**. Example

mass spectra for low and moderate collision voltages are presented in **Figure 2.10C & 2.11D** for the nitrate-free rhomboid **3** and nitrate-adducted rhomboid **7**, respectively.

CID of the nitrate-free rhomboid **3** reveals three sequential dissociation steps (**Figure 2.10A**). First, the intact rhomboid **3** dissociates to the isobaric half-rhomboid **4** with a maximum relative abundance observed at a CV of 10 V. Next, the half-rhomboid **4** loses its bis-pyridine ligand **2** to form the denitrated Pt-precursor ion **5** with a maximum relative abundance observed at 20 CV. The final step involves fragmentation of the Pt-precursor ion **5** to form ion **6** with an undetermined structure, but with a mass and isotope pattern corresponding to $[\mathbf{5} - 2\ Pt - 3\ PEt_3 + H]^+$.

CID of the nitrate-adducted rhomboid **7** reveals 4 sequential dissociation steps (**Figure 2.10B**). The first two dissociative products are observed at 15 CV. These two products are identified: **8** is formed from the loss of $[\mathbf{5} + NO_3^-]^+$ and the half-rhomboid **4** is formed from the loss of a nitrate-adducted half-rhomboid ion. The half-rhomboid **4** can also result from the loss of one of its bis-pyridine ligands **2** from the observed ion **8**. Continued dissociation and fragmentation of the half-rhomboid ion **4** then follows a similar pattern as observed with the half-rhomboid **4** from the dissociation of the nitrate-free rhomboid **3**, wherein ion **4** loses its bis-pyridine ligand **2** to form a nitrate-free precursor ion **5** before fragmenting to ion **3**.

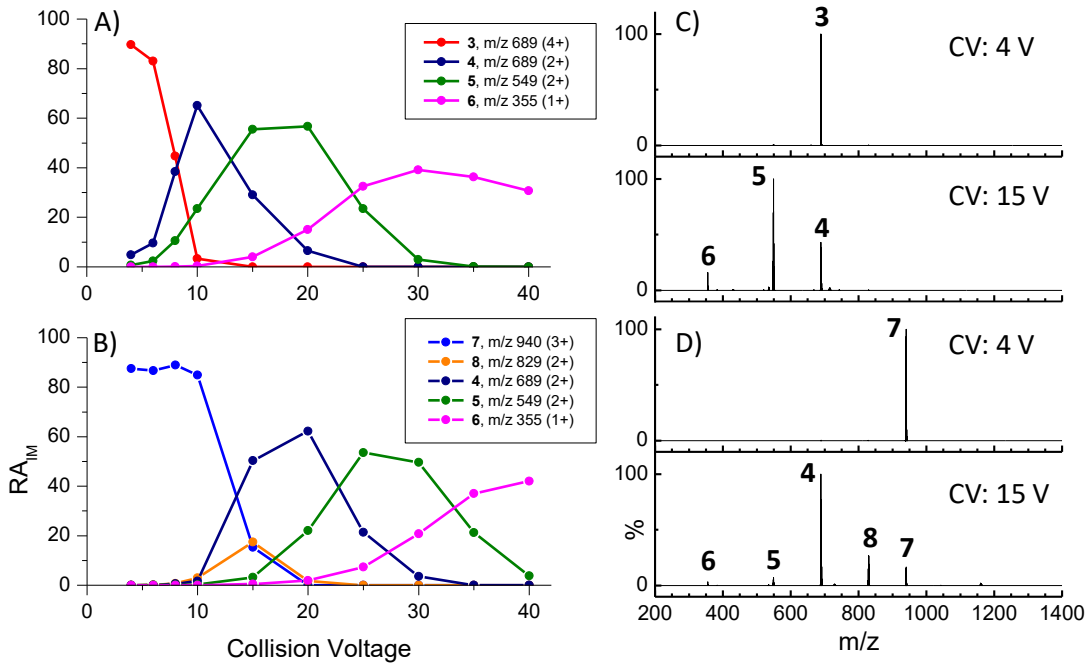

Figure 2.10. Plot of the relative IM abundances (RA_{IM}) as a function of trap collision voltage for the CID of A) the nitrate-free rhomboid ion **3** and B) the nitrate-adducted rhomboid 7. Example MS spectra resulting from the CID of **3** and **7** are shown as panels C) and D), respectively.

2.3.4. Survival Yield Comparisons

From the plots of the relative abundance of the CID precursor ions (either **3** or **7**) as a function of collision voltage (**Figure 2.10**), it is apparent that the nitrate-adducted rhomboid **7** survives until significantly higher collision voltage compared to the nitrate-free rhomboid **3**. Converting collision voltages to laboratory-frame collision energies (E_{lab}) can normalize for the relative collision energies of different charge states at the same collision voltages, since at the same collision voltage, an ion with higher charge will experience a greater acceleration (larger collision forces) into the collision cell than an ion with lower charge. Even when normalizing for effects of different ion charge in the

collision cell, it is still apparent that the nitrate-free rhomboid ions **3** are more fragile than the nitrate-adducted rhomboid **7**. This result is likely due to the greater destabilizing Coulombic repulsion of ions with higher charge, wherein the charge reduction associated with nitrate adduction results in more stable gas-phase ions.

The survival yield (SY) abundances of the CID precursor ions were then plotted as a function of E_{lab} of the CID precursor ions (**Figure 2.11)** to normalize for collision energy as ions with higher charge will experience greater acceleration in the collision cell. After fitting the SY data to sigmoidal curves, the inflection points were used to determine CE_{50} values for each precursor ion where half of the initial relative abundance is observed. Fitting of these data reveal CE_{50} values of 32.0 eV for the nitrate-free rhomboid **3** ion and 40.4 eV for the nitrate-adducted rhomboid **7**. While this manipulation is used as an attempt to mitigate the effects of different charge states when exposed to similar collision potentials, the difference in these energies is likely a result of increased Coulombic repulsion effects, wherein the ion with more charge sites may be driven to dissociate at lower energies. Overall, these data suggest an increase in gas-phase stability with the addition of the nitrate anion.

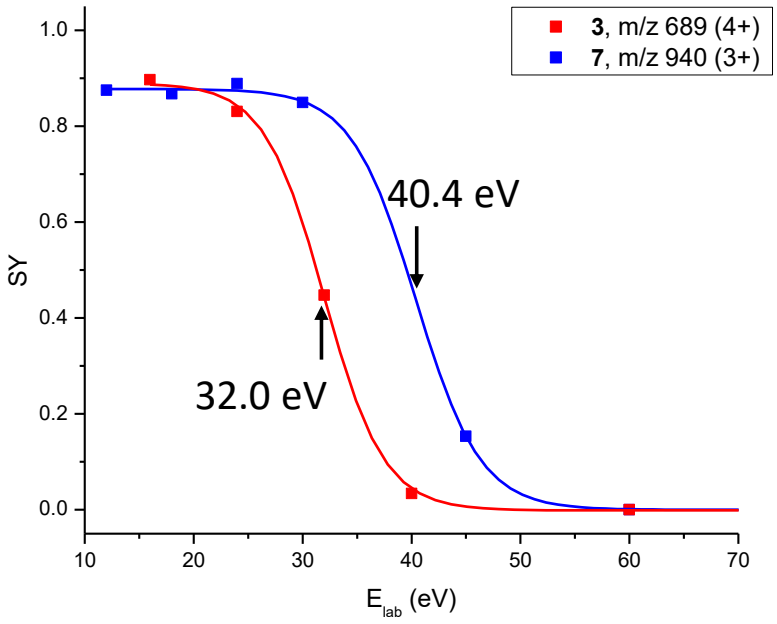

Figure 2.11. Plots of survival yield (SY) of the CID precursor ions as a function of their laboratory-frame collision energies (E_{lab}). Sigmoidal fits of each SY data set reveal inflection points corresponding to the $E_{lab,50}$ of 32.0 eV and 40.4 eV for the nitrate-free rhomboid (**3**, red) and nitrate-adducted rhomboid (**7**, blue) ions, respectively.

2.4. Discussion

The utility of IM-MS as a reaction product characterization technique is dependent on its ability to preserve intact, solution-phase reaction products through separation and detection in the gas phase. Through proper tuning of the TWIMS-MS instrument, we show that intact, high-charge complexes can be ionized and transmitted through the instrument in high relative abundances. For the first time, counterion-free CDSA reaction product ions are observed from the mixture of precursors without prior isolation of reaction product complexes. Observed CDSA ion charge states are dependent primarily on the number of metal-centers and anion adducts, such that reduction in observed nitrate adducts leads to increase in ion charge and consequently an increase in repulsive Coulombic

forces. Therefore, high-charge complexes require careful instrument tuning to observe intact ions with internal energies below their respective dissociation thresholds.

The specific utility of IM herein is two-fold. First, IM is used as a separation tool for the isobaric nitrate-free full rhomboid **3** and the half-rhomboid **4** ions. These ions are separated using IM such that their relative abundances can be determined from the observed mobility spectra. Second, the IM distribution of each identified ion can be fit to single Gaussian peaks with high coefficients of determination ($R^2 > 0.995$ for all fits). Therefore, all identified ions adopt singular conformers in the gas phase, or other conformers are indistinguishable at the given IM resolution. Unlike what has been observed with triangular CDSA complexes having a similar coordination motif,[104] we did not observe multiple conformers (i.e. open and closed) of these rhomboidal ions at either charge state.

After tuning, mass selection and collisional activation (i.e. CID) of the observed nitrate-free and nitrate-adducted rhomboid ions (**3** and **7**, respectively) confirm the topologies of the ions as well. The sequential losses observed and highlighted in **Figures 2.5 & 2.10** show that the dissociation pathways of the two rhomboid ions to the half-rhomboid ion **4** are different. The nitrate-free rhomboid **3** dissociates in half to form the half-rhomboid at relatively low collision energies, while the nitrate-adducted rhomboid **7** appears to lose its nitrate adduct in its first dissociative loss either as a nitrate-adducted analogue of the fragment **5** (i.e. $[\mathbf{5} + NO_3]^+$) to form **8** or a nitrate-adducted analogue of the half-rhomboid ion **4** (i.e. $[\mathbf{4} + NO_3]^+$) to form **4**. Because the appearance energies of these two observed dissociative products are the same (15 V), it appears that these ions

are both formed from the nitrate-adducted rhomboid **9** at lower collision energies and at higher collision energies, the half-rhomboid ion **4** may be formed from the loss of one bis-pyridine ligand **2** from ion **8**. Additionally, the IM drift times do not change as a function of collision voltage, and each ion can be fit to single Gaussian distributions throughout the CID experiment (see **Figure 2.12**); therefore, ions are observed to dissociate rather than rearrange or unfold in the gas phase.

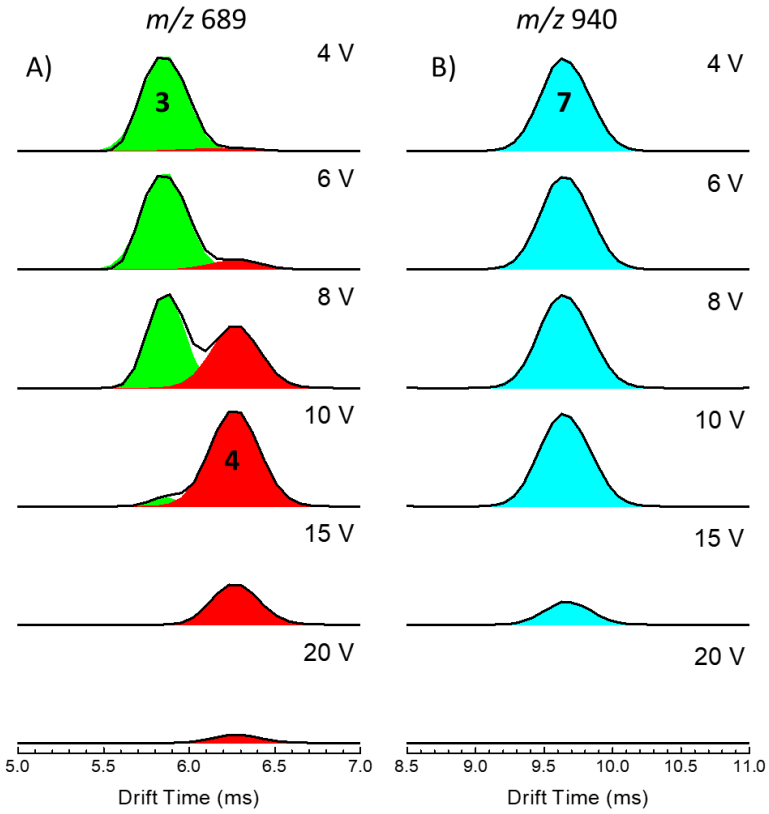

Figure 2.12. Gaussian peak-fitting IM spectra resulting from CID of the (A) isobaric nitrate-free rhomboid (**3**, 5.86 ms, green) and half-rhomboid (**4**, 6.25 ms, red) and (B) the nitrate-adducted rhomboid (**7**, 9.67 ms, blue).

Overall, these dissociation results suggest that the nitrate adduct is coordinated to one of the Pt-centers of the rhomboid complex and may disrupt closure of the rhomboid ring. Without experimentally determined CCS and crystallographic structures of these

ions, these conjectures cannot be definitively confirmed. Calibration of CCS on the traveling-wave based IM separations requires calibrants with similar interaction potentials to the buffer gas and the ions studied herein and which have not been previously established. While other calibrant systems are available, they have been primarily designed and tested for CCS determination of peptide[111] and protein ions.[39, 112]

With proper CCS calibrants and MD simulations of candidate structures, it may be possible to determine the overall structure of the nitrate-adducted rhomboid, although the CCS difference between open and closed rhomboid conformers may be minimal and require significantly greater IM resolving power to separate than is commercially available. While MD simulations of other CDSA reaction products postulate that bulkier counterions, like triflate or hexafluorophosphate, can bind to the central void of larger supramolecular complexes and coordinate to metal centers,[104] our results suggest that when nitrate is present, it is tightly bound to one of the Pt coordination sites.

Currently, commercial drift-tube based IM instrumentation (e.g. Agilent 6560 IMS-Q-TOF) is unsuitable for first-principles determination of CCS of fragile complexes due to the post-mobility collision cell which cannot be tuned to preserve intact, high-charge complexes without significantly reducing the resolving power of the mobility separation (data not shown).[21, 106] Reduction of the potentials of the post-IM collision cell leads to the largest reduction of ion heating effects allowing for transmission and mass detection of fragile complexes; however, reduction of these potentials slows the ions, which leads to diffusional broadening of the observed IM spectra such that any CCS information is lost. Additionally, the potential for post-IM fragmentation severely

complicates assignment of IM signals for CCS determination as ions will transmit through the drift tube as high-order complexes but be identified as fragments or dissociation products. Thus, for first-principles determination of CCS of fragile CDSA reaction product complexes, home-built or modified commercial instrumentation must be used.[104]

Overall, we observe that careful instrument tuning is required to observe intact, anion-free CDSA reaction products in high relative abundances. CID provides topological confirmation of the expected reaction products and suggests that when observed, nitrate adducts are specifically coordinated to Pt-centers. Nitrate adducts mitigate effects of Coulombic repulsion in the gas phase as the nitrate-adducted reaction products survive at higher collision energies than the nitrate-free analogue. The gas-phase observations made herein may suggest that in the condensed phase, charge neutralization with counterions may improve the stability of larger reaction products, like 3D geometries or sheet-like reaction products,[84] and that these effects may be beyond attractive Coulombic effects (*vis.* negatively charged counterions binding non-specifically to positively charged reaction products). While anionic adducts are often ignored (or omitted) when reporting MS or IM-MS results of supramolecular complexes, the comparative effects of other anions (*e.g.* triflate, hexafluorophosphate, etc.) may prove valuable to the design of larger CDSA products where Coulombic repulsion effects may prevent observation of intact products either by condensed-phase or gas-phase characterization techniques. Rational design of the shape and structure of CDSA reaction products can be tested by CID results correlated to condensed-phase chemistries and to specific effects of adduction of other anionic counterions. While the effects observed herein are limited to the gas phase, condensed-

phase reaction products will likely bind anions resulting from Coulombic attraction, which may affect the stability or intended performance of reaction products. Overall, gas-phase characterization of CDSA ions must be performed below their respective dissociation thresholds, and CID of intact ions reveal that charge reduction through adduction of anions results in increased stability of lower-charged reaction products in the gas phase.

2.5. Conclusion

Detection and characterization of fragile complexes by MS and IM-MS must be performed carefully to minimize effects of collisional activation. By carefully tuning IM-MS instruments for small molecules and complexes in a similar protocol to what has been published for proteins, large, intact reaction products have been observed from solution mixtures of reaction precursors. When MS signals overlap, the IM peak areas can be used for determination of relative abundance of isobaric ions. An additional benefit of determining relative abundance for CID experiments using extracted IM spectra includes the ability to focus on pre-mobility dissociation rather than the ensemble of all post mass-selection dissociation events as pre-mobility dissociation will result in product ions with unique drift times; whereas, post-mobility fragmentation will result in *m/z* of the dissociation product ions but with the drift time (or arrival time) of the precursor ions.

The IM-MS data clearly show singular, gas-phase conformations and structures for the precursor and product ions of CID as each identified ion can be fit to singular Gaussian peaks, supporting the notion that these ions are rigid in structure and conformationally homogeneous. The results of CID reveal the fragmentation pathways,

and neutral and charged dissociation products help to confirm the topology of the mass-selected reaction product ions and identify coordination sites of anionic adducts. Additionally, the SY results provide a basis for comparison of the stability of reaction products. They show that the gas-phase stability of these supramolecular complex ions is dependent on the supramolecular or macromolecular shape and charge rather than the number of Pt—N bonds. Application of IM-MS to the characterization of small molecules and labile complexes requires careful tuning to preserve solution-phase structures. IM-MS provides structural characterization of supramolecular complexes which may not be achieved by traditional spectroscopic techniques and serves as a potential high-throughput approach for characterizing CDSA reaction products once instrument tuning is complete.

3. DEVELOPMENT OF NATIVE MS CAPABILITIES ON AN EXTENDED MASS RANGE Q-TOF MS*

3.1. Introduction

Advancements in biophysical techniques drive greater understanding and deeper interrogation of the structure and function of proteins and protein complexes. Contributions of mass spectrometry (MS) towards studies of protein function have largely been realized through proteomics, including both bottom-up and top-down methods for analysis of protein primary structure.[113, 114] These methods are often optimized using denaturing conditions to expose more amino acids to proteolytic digestion in solution or fragmentation in the gas phase. More recently developed methods include those used in studies of intact protein complexes, where solution-phase conformations and noncovalent contacts are retained in the transition from solution to the gas phase.[16, 25] Recent developments in these areas are frequently referred to as native MS (nMS) and native ion mobility-MS (nIM-MS). One major focus of nMS has made possible studies of protein complexes with aims to develop better understanding of quaternary structure, including stoichiometry and topology.

---

* Reprinted with permission from Mallis, C.S.; Zheng, X.; Qiu, X.; McCabe, J.W.; Shirzadeh, M.; Lyu, J.; Laganowsky, A.; Russell, D.H. Development of Native MS Capabilities on an Extended Mass Range Q-TOF MS. *International Journal of Mass Spectrometry*, **2020**, *458*, 1-7.

Challenges for nMS of intact proteins and protein complexes include developing better understanding of how the solution conditions (e.g. buffer, cosolutes, solvent) influence protein structure and ionization.[115-118] Additionally, transmission of ions with high mass-to-charge ratios (*m/z*) represents a challenge that has been overcome by development of state-of-the-art MS instruments.[12, 119, 120] Due to the high *m/z* of large, intact protein complexes (>100 kDa), high resolving power is needed to separate signals with smaller mass shifts. Separation of these signals makes possible the identification of sequence modifications (e.g. truncations, mutations, post-translational modifications (PTM)) and binding of endogenous ligands, salts, and other small molecule adducts.[12] Efficient desolvation helps to remove solvent and volatile buffer solutes from droplets formed by electrospray ionization (ESI), leading to narrower ion signals and greater ability to resolve what would otherwise be hidden.[12] One method for enhancing desolvation includes the use of small, low flow emitters (1-3 μm inner diameter, nL/min flow) that promote formation of smaller droplets compared to traditional direct infusion nanoESI, and their usage in nMS studies has been invaluable.[121, 122] As the transition towards studies of larger (kDa to MDa) biomolecular complexes have progressed, numerous types of ESI emitters and ion source designs have evolved to accommodate static-spray nanoESI.[123]

Here, we report results obtained using a quadrupole-time-of-flight (Q-TOF) instrument (Agilent 6545XT Q-TOF MS) that has extended mass range (*m/z* 30,000) and a modified static nanospray ESI emitter (1-10 μm O.D.) for nMS studies of protein complexes. The performance of the instrument is demonstrated using results obtained for several soluble protein complexes, *viz.* alcohol dehydrogenase (tetramer, 147 kDa),

pyruvate kinase (tetramer, 232 kDa), a trimeric 127 kDa membrane protein complex (ammonium transport channel, AmtB), and the tetradecameric 801 kDa protein chaperonin GroEL from *E. coli*. This study reports enhanced performance (in terms of *m/z* range and resolution) of a Q-TOF mass spectrometer for large native, intact protein complexes. Additionally, interrogation of low relative abundance and low molecular weight adducts was performed on ions formed by collision-induced dissociation (CID) of the native protein complexes.

3.2. Experimental

3.2.1. Materials

Ammonium acetate and lyophilized powders of yeast alcohol dehydrogenase and rabbit muscle pyruvate kinase were purchased from Sigma-Aldrich (St. Louis, MO). Wild type and double mutant (E87C, C312T) AmtB protein complex from *E. coli* was expressed and purified as previously described.[124] The GroEL chaperonin complex was purified as previously described.[125] More detailed information for these complexes is provided in **Table 3.1.** All buffers and lyophilized protein samples were dissolved in 18.2 MΩ·cm water (Barnstead Easy Pure II, Thermo Scientific). All samples were buffer exchanged to 200 mM aqueous ammonium acetate using Micro BioSpin P-6 gel columns (BioRad) at working concentrations of 1-10 μM. For AmtB, the samples were buffer exchanged into 200 mM ammonium acetate supplemented with 2x critical micelle concentration of tetraethylene glycol monooctyl ether (0.5% C_8E_4).

Table 3.1. Protein complex details include UniProt ID codes for determination of theoretical molecular weights as well as PDB codes used for inset structures in the main text.

Protein	Species	UniProt ID	MW (kDa)	Complex	pI	PDB	Source
Alcohol dehydrogenase	ADH1_YEAST	P00330	147.0	Tetramer	6.21	4W6Z	Sigma-Aldrich
Pyruvate Kinase	KPYM_RABIT	P11974	232.0	Tetramer	7.6	1F3W	Sigma-Aldrich
Bacterial ammonium transport channel	AMTB_ECOLI	P69681	126.9	Trimer	6.25	1U7G	Texas A&M University
GroEL	CH60_ECOLI	P0A6F5	800.7	Tetradecamer	4.85	1SS8	Texas A&M University

3.2.2. Mass Spectrometry

The protein samples were analyzed on an Agilent 6545XT Q-TOF mass spectrometer (Agilent Technologies, Santa Clara, CA). Agilent MassHunter Acquisition (B.09) was used for data acquisition. The Agilent nanoelectrospray ionization (nanoESI) source was adapted using custom parts to enable static spray. Briefly, borosilicate capillary emitter tips were pulled in house using a flaming/brown micropipette puller (P-1000, Sutter Instruments), loaded with aqueous protein solution, and placed in a fabricated capillary tip holder containing a platinum wire as described previously (see **Figure 3.1** & **3.2** for details of the setup and technical drawings of the custom-fabricated tip holder).[123] The tip holder was mounted onto the nanoESI capillary holder and positioned to within ~5-10 mm of the nanoESI spray shield. As the emitter solution is maintained at ground, no modification to the application of ESI potentials is required, allowing for the ease of transition between static spray and LC-compatible nanoESI. Capillary voltages are defined as the negative offset between the grounded emitter and the entrance to the ion transfer capillary (see **Figure 3.1(C)**). Capillary voltages were adjusted to maximize ionization efficiency for each protein complex. For nMS analyses, capillary exit and

skimmer cone potentials were optimized to maximize ionization and ion transmission through the source region while simultaneously minimizing dissociation.

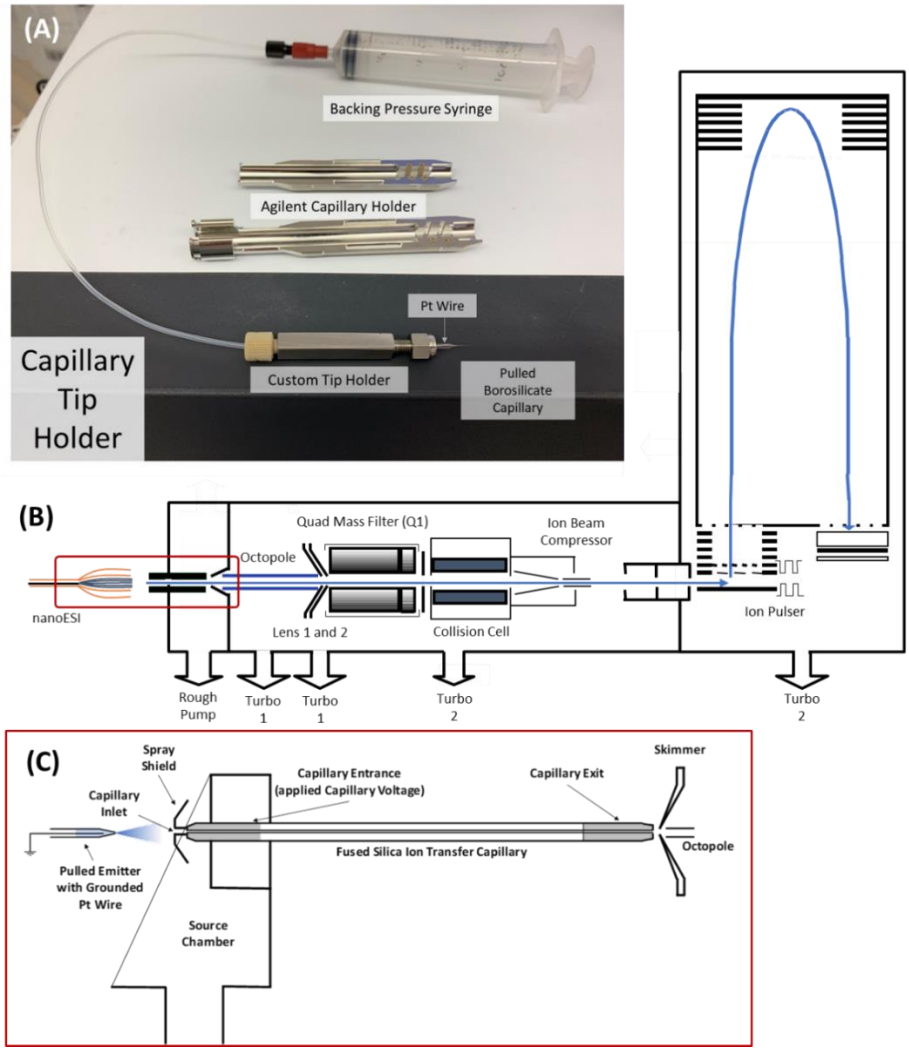

Figure 3.1. (A) A custom static-spray capillary emitter holder was fabricated in house to fit inside the Agilent capillary holder for compatibility with the Agilent nanoESI source. This tip holder contains a platinum wire to ground the solution and has a syringe attachement to apply backing pressure. The tip holder fits inside of the Agilent capillary holder which is placed inside the nanoESI source. The emitter tip is positioned within 5-10 mm of the spray shield. (B) A schematic of the Agilent 6545XT is shown with ion optics labeled and the source region highlighted (red box). (C) A shematic of the instrument source shows location of the capillary exit and skimmer cone, where the capillary exit and skimmer potentials are applied, respecctively. Increasing these potentials allows for in-source activation.

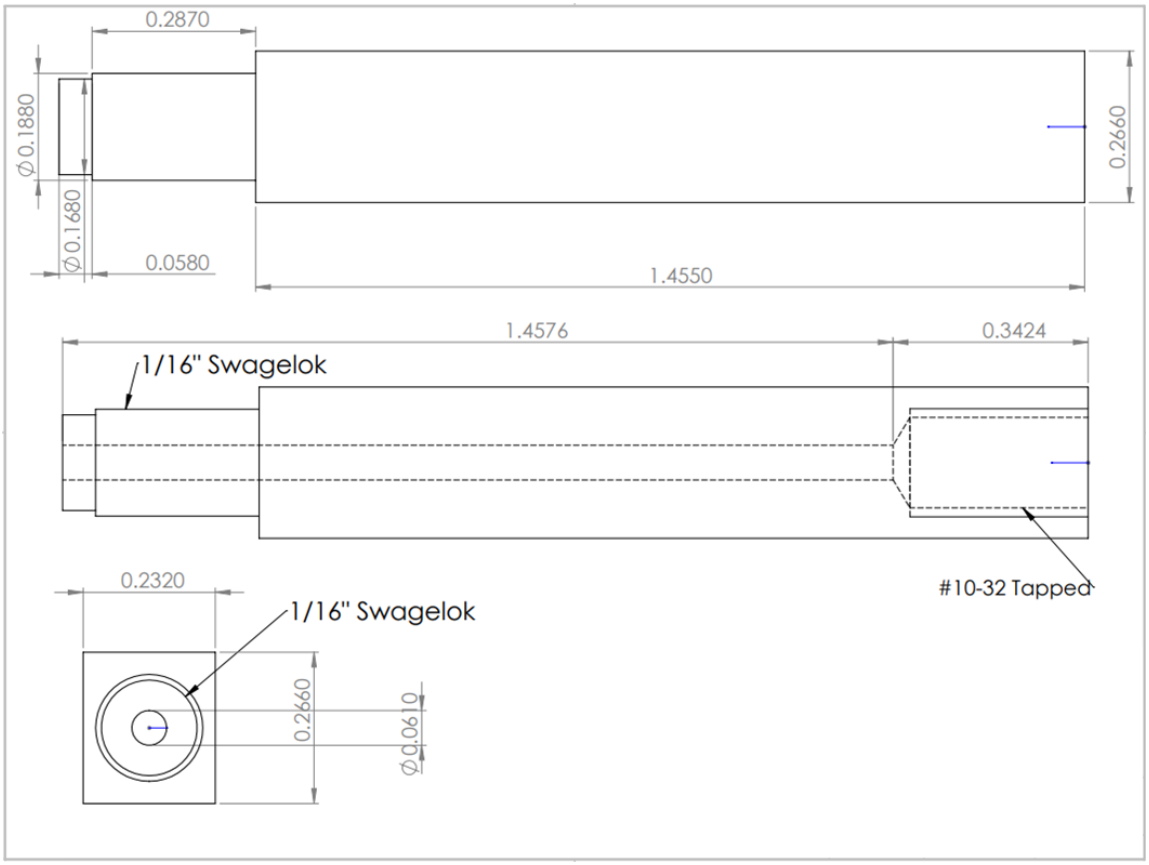

Figure 3.2. CAD drawings of the modified static spray tip holder shown in Figure S1. This tip holder was machined out of 316 SS and features (left) a 1/16" Swagelok extrusion to secure the emitter tip with a graphite ferrule and (right) a #10-32 tapped hole for applying backing pressure.

For alcohol dehydrogenase (ADH) and protein kinase (PK), the capillary exit and skimmer potentials were adjusted to optimize transmission of intact protein complex ions or to promote collision-induced dissociation (see **Figures 3.3-3.6**). For example, in-source dissociation (ISD) is performed at high source (capillary exit >240 V; skimmer >260 V), leading to ejection of high charge monomer ions. At low source potentials, overall ion transmission is decreased leading to poor signal-to-noise ratios. The GroEL and AmtB

collisional activation and collision-induced dissociation (CID) experiments were performed by increasing potentials in the collision cell (**Figure 3.1**), and N_2 was used as a bath gas at the recommended backing pressure (22 psi).

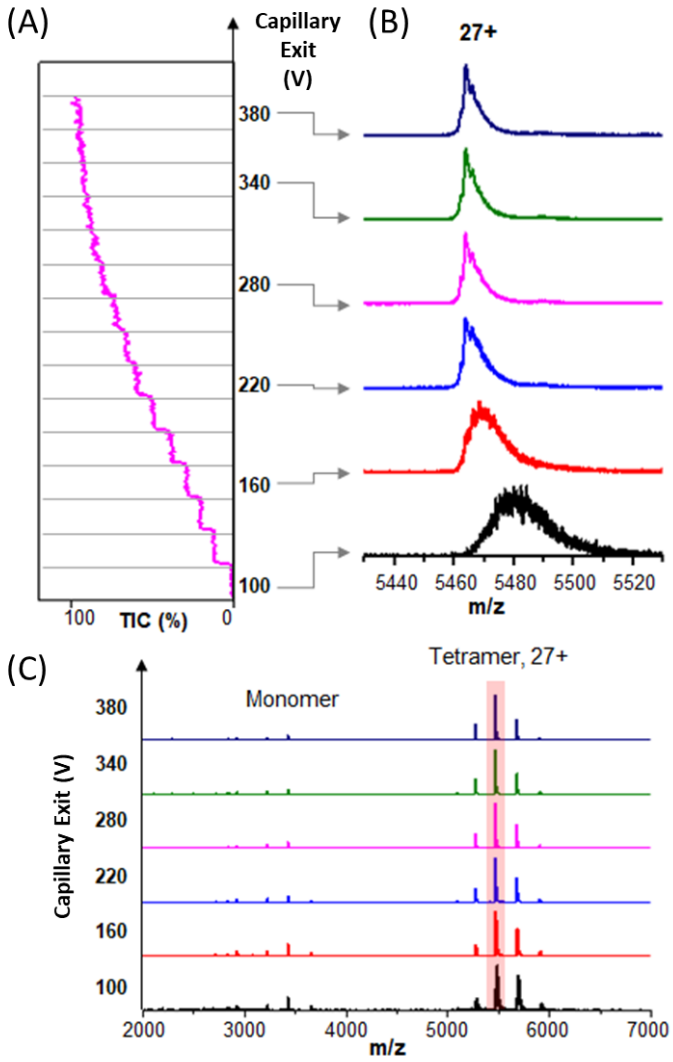

Figure 3.3. Signals for alcohol dehydrogenase (ADH) were optimized by tuning capillary exit voltages (skimmer held at 140 V) to maximize ion abundances while minimizing collision-induced dissociation. (A) Total ion chromatogram (TIC) shows increasing ion current with increasing capillary exit potentials. (B) Increasing capillary exit voltages leads to decreased peak widths as noncovalent adducts are removed. (C) Full mass spectra show similar features with capillary exit voltages above 220 V including the native homotetrameric complex centered at 27^+.

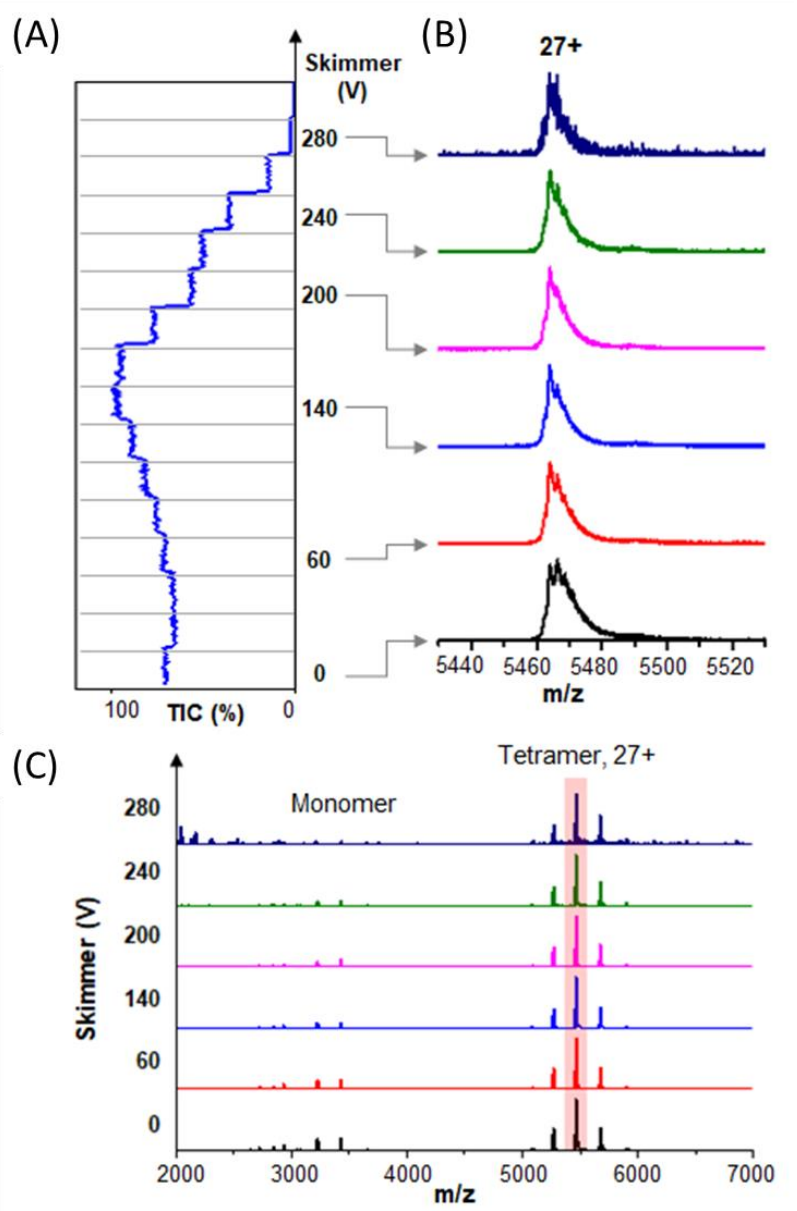

Figure 3.4. (A) Increasing skimmer potentials (capillary exit potential held at 220 V) leads to maximized TIC signal at 140 V. (B) At 140 V, the ADH^{27+} ions have the smallest peak widths. Above 140 V, ion transmission is decreased, leading to poor signal-to-noise. Below 140 V, poor desolvation leads to increased peak widths. (C) Mass spectra shown as a function of skimmer potential shows similar features at intermediate skimmer potentials (60 V – 240 V) including the native tetrameric complex centered at 27^{+}.

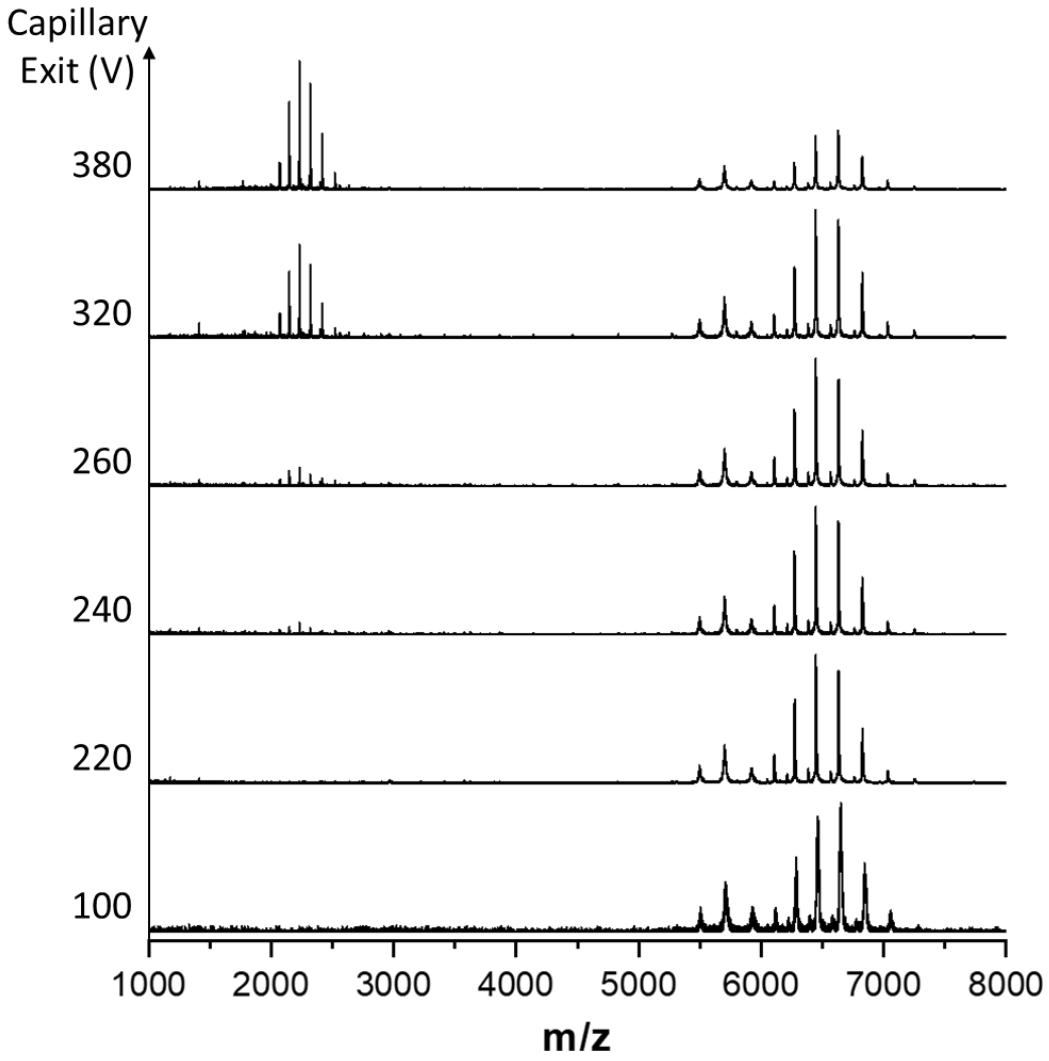

Figure 3.5. Mass spectra of pyruvate kinase (PK) at increasing capillary exit potentials (skimmer held at 140 V) show collision-induced dissociation with increased capillary exit voltages. Ejected pyruvate kinase (PK) monomers are observed centered at 26^{+} with capillary exit voltages above 220 V. The observed monomer ions are ejected from the high relative abundance tetramer ions. No ejected monomers are observed from the other low relative abundance PK complexes.

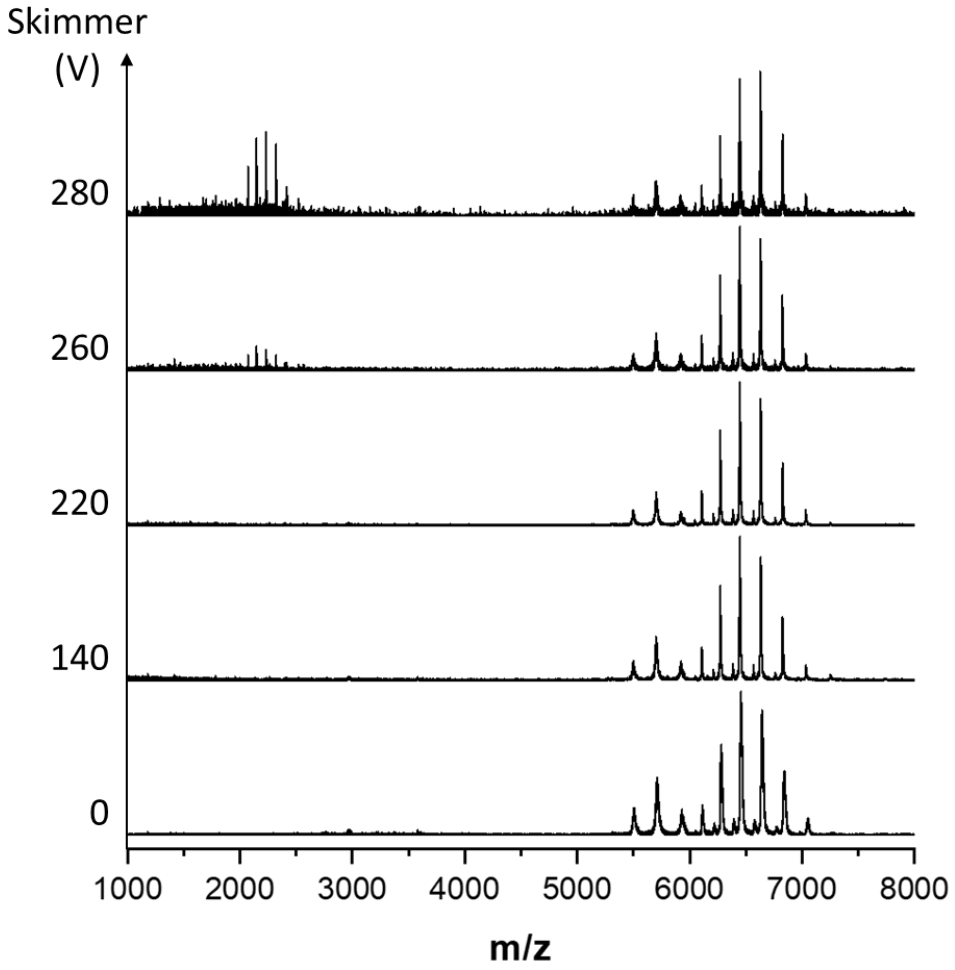

Figure 3.6. Mass spectra resulting from increasing skimmer voltages (capillary exit potential held at 220 V) for PK show monomer ejection resulting from collision-induced dissociation at high skimmer potentials (>220 V). Similar to ejected PK monomers at high capillary exit voltages (Figure S5), the measured masses of monomer ions correspond to the high relative abundance, native PK tetramer ions.

ISD experiments (for GroEL) were performed as described above by increasing the capillary exit potentials from 200 V to 380 V. Prior to analysis of protein samples, the instrument was tuned in high-mass mode (*m/z* 20,000) and appropriate mass ranges were selected for different experiments. Sliding scales for different mass ranges are available

for *m/z* 90-10,000 through *m/z* 6,830-30,000 and were adjusted and recalibrated as needed to optimize for different experiments.

3.2.3. Data Analysis

All mass spectra were compiled using standard vendor procedures (Agilent MassHunter Qualitative Analysis (B.10) and BioConfirm (B.10)). Experimentally measured molecular weights (MW) were determined from peak maxima with average masses and standard deviations calculated from identified charge states. Theoretical MW were calculated based on the appropriate UniProt sequences using ChemCalc.[109, 126] Theoretical isoelectric points (pI) were obtained using the ExPASy web server and are shown in **Table 3.1**.[127]

3.3. Results & Discussion

For this study, we selected several large protein complexes ranging in size from 127 kDa to 801 kDa which had been used in prior studies that employed the extended *m/z* range (20 kDa *m/z*) Agilent 6560 IM-Q-TOF and homebuilt ion mobility-Orbitrap instruments.[13, 53, 56, 116, 120] These complexes include two soluble proteins (alcohol dehydrogenase (ADH) and pyruvate kinase (PK)), an integral membrane protein complex (ammonium transport channel (AmtB)), and a chaperonin protein (GroEL) from *E. coli*.

3.3.1. Soluble Protein Complexes

Optimization of ion source conditions was performed using the homotetrameric protein complexes ADH and PK (see Experimental Section). Tuning the source potentials

was necessary in order to optimize desolvation and ionization efficiencies. A compromise between maximizing ion transmission and minimizing dissociation was reached using similar source potentials for both protein complexes (capillary exit: 220 V; skimmer: 140 V).

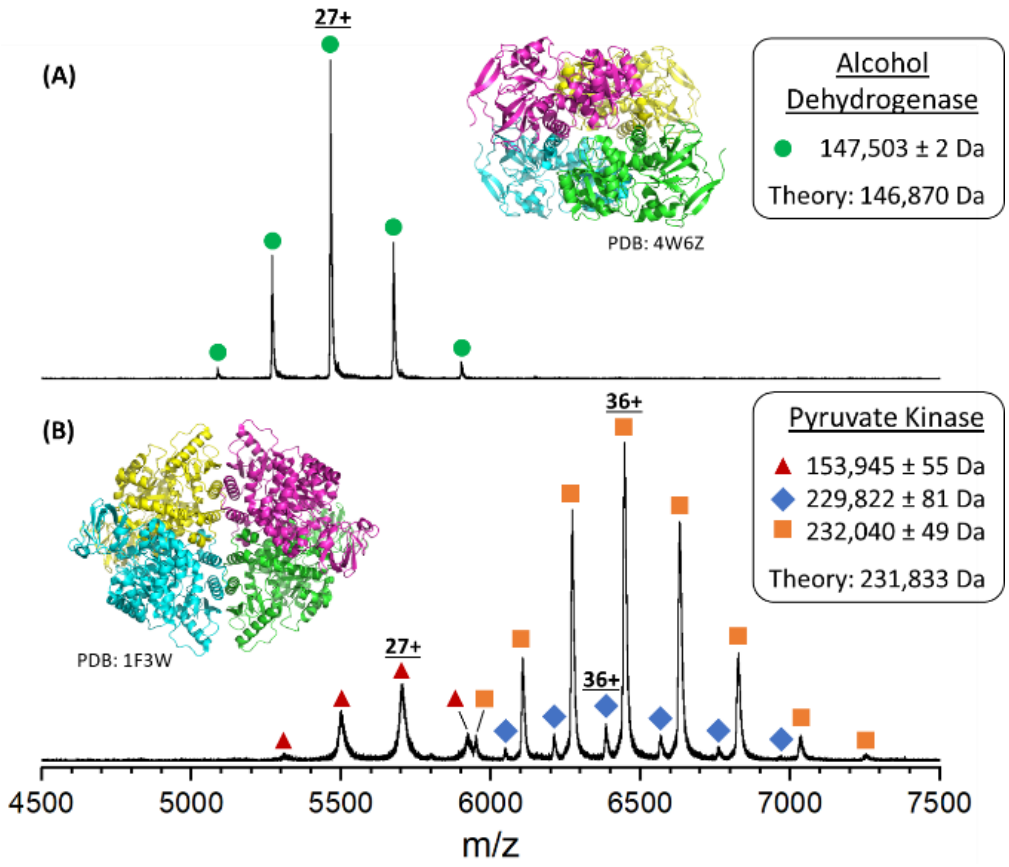

Figure 3.7. Native mass spectra of (A) alcohol dehydrogenase (ADH) and (B) pyruvate kinase (PK) reveal the intact, native protein complexes. Zero-charge molecular weights determined from the experimental charge-state distributions are shown in the inset boxes along with the theoretical MW. Differences between theoretical and zero-charge molecular weights is attributed to unresolved, nonspecific adducts that are common features of native mass spectra.[128] The peaks labelled with red triangles (154 kDa) correspond to an unidentified species; however, these same signals have been reported previously as impurities (see text).

Native mass spectra of intact ADH and PK are shown in **Figure 3.7.** The peaks for the intact ADH homotetrameric complex (**Figure 3.7(A)**) were observed to have a charge-state distribution (CSD) centered at 27^+ and a measured MW of 147.5 kDa which is in good agreement with the theoretical MW (146.9 kDa). The discrepancy between the theoretical and measured MW of ADH is attributed to unresolved adducts and/or endogenous ligands; CID of ADH produces monomers having a range of adducted small molecules (see **Figure 3.8(C)**). The MW of the apo-ADH ejected monomer (36,726 ± 2 Da) is in excellent agreement with the theoretical monomer MW (36,718 Da).

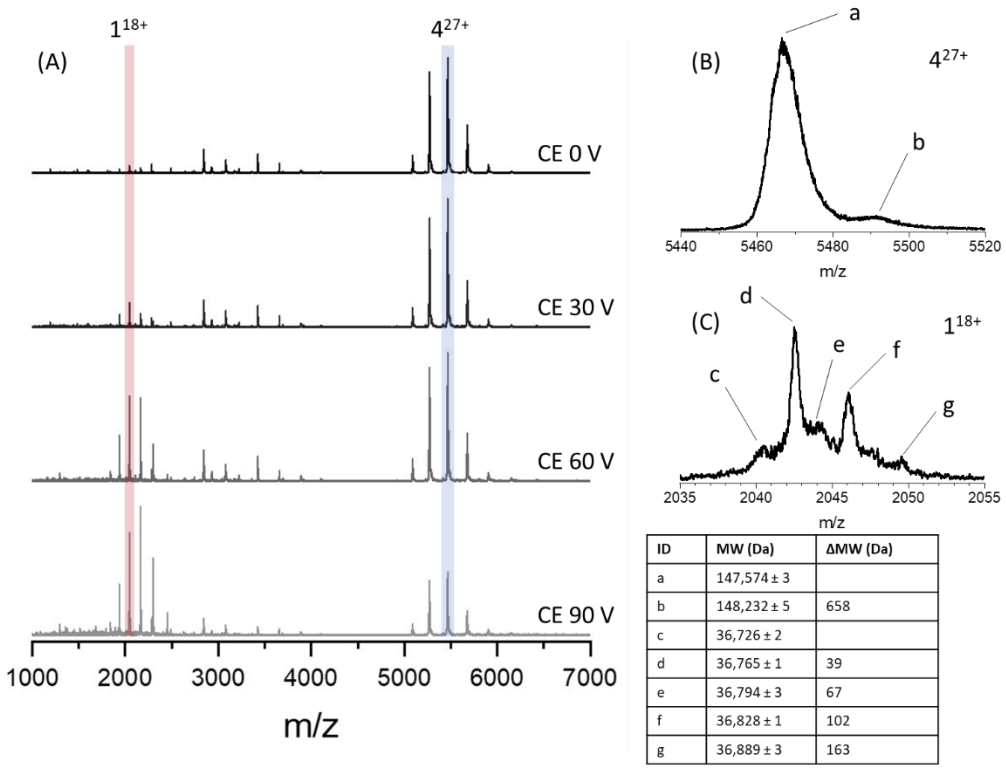

ID	MW (Da)	ΔMW (Da)
a	147,574 ± 3	
b	148,232 ± 5	658
c	36,726 ± 2	
d	36,765 ± 1	39
e	36,794 ± 3	67
f	36,828 ± 1	102
g	36,889 ± 3	163

Figure 3.8. (A) CID of native ADH was performed by increasing CE voltages. (B) Tetramer (27^+) spectrum at 0 V show signal corresponding to native ADH and another species heavier by *ca.* 660 Da. (C) Ejected monomer (18^+) signal at 90 V shows a host of adducts with the apo-monomer (labeled *c*) matching the theoretical monomer MW (36,718 Da).

The native mass spectrum of pyruvate kinase (PK) **(Figure 3.7(B))** contains signals that are assigned to three different complexes. The intact homotetrameric complex shows peaks centered at the 36^+ charge state with a measured mass of 232.0 kDa, which agrees well with the MW of PK after removal of the initiator methionine and acetylation of the N-terminal serine (231.8 kDa).[129] Low abundance signals centered at 36^+, yield a measured MW of 229.8 kDa, tentatively assigned to ions from truncation of the first five N-terminal residues (^{1}MSKSH^5) of each subunit with a corresponding theoretical MW of 229.9 kDa for the resulting complex. A third CSD is observed that corresponds to a 153.9 kDa complex centered at 27^+. The increased peak widths, much lower MW compared to that of the native tetramer complex, and unidentified stoichiometry suggest that this complex is not a simple sequence modification of the native PK complex. It appears more likely to be a contaminant in the lyophilized preparation. While the specific sequence of this contaminant remains unknown, similar signals have been reported previously from samples that were prepared in a similar manner as was done here.[24, 53, 130]

3.3.2. Membrane protein complexes

Membrane protein complexes have become more important as pharmaceutical drug targets,[131] yet their detection by nMS methods has remained challenging due to nonspecific adduction of lipids and their instability in aqueous, hydrophilic environments. Solubilizing of membrane protein complexes in detergent micelles removes the complexes from their supporting lipids without precipitation into solution.[132] The detergent micelles are then removed via collisional activation, resulting in well-resolved CSDs. Here, a double mutant variant of the ammonium transport channel complex (DM-AmtB) as well

as wild-type (WT-AmtB) are used to evaluate the capabilities of our modified instrument towards characterization of native membrane protein complexes.

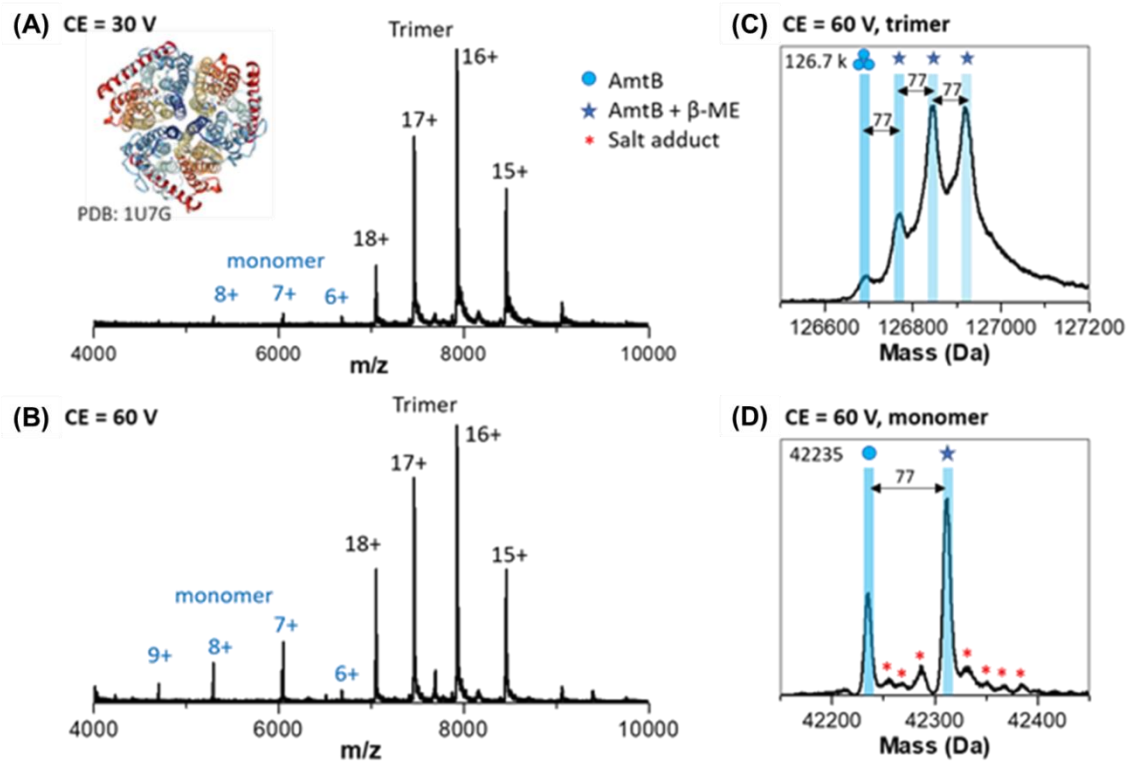

Figure 3.9. Native MS of a trimeric integral membrane protein complex. (A) mass spectrum of DM-AmtB at low collision energy (30 V) reveals the native intact trimer complex with a mass of 126.7 kDa. (B) Increasing the collision energy to 60 V leads to ejected monomer ions. (C) The zero-charge mass spectrum reveals the presence of up to three β-mercaptoethanol (β-ME) (77 Da adducts) on the intact trimer ions. (D) Zero-charge mass spectrum of ejected monomer also reveals low abundance salt adducts and a single β-ME adduct.

Figure 3.9. contains native mass spectra for the double mutant (E87C, C312T) bacterial ammonium channel (DM-AmtB, 127 kDa) membrane protein complex. Abundant signals for the intact homotrimeric complex are centered at 16^+ (**Figure 3.9(A-B)**). The mass spectrum of the trimer (**Figure 3.9(C)**) contains a distribution of four

species, *viz.* the apo-AmtB trimer complex and signals for up to three adducts that are shifted by 77 Da. We attribute the mass shifts to covalent disulphide-binding of the β-mercaptoethanol (β-ME) molecule to the cysteine side chain of the E87C mutant. Increasing the collision energy leads to monomer ejection, and the ejected monomer signals provide further evidence for the covalently bound β-ME molecules (see **Figure 3.9(D)**). The measured mass of the apo-DM-AmtB monomer ions (42,235 Da) is in reasonable agreement with the theoretical MW (42,273 Da). Similar β-ME modifications are not observed in the mass spectra of the wild-type AmtB (see **Figure 3.10)**. Ejected monomers from WT-AmtB also have measured molecular weights (42,292 Da) in agreement with theoretical MW (42,301 Da). These results further illustrate the utility of the Q-TOF platform for analyzing membrane proteins with sufficient resolving power to identify small molecule adducts with and its potential for future ligand and lipid binding studies.[64, 123]

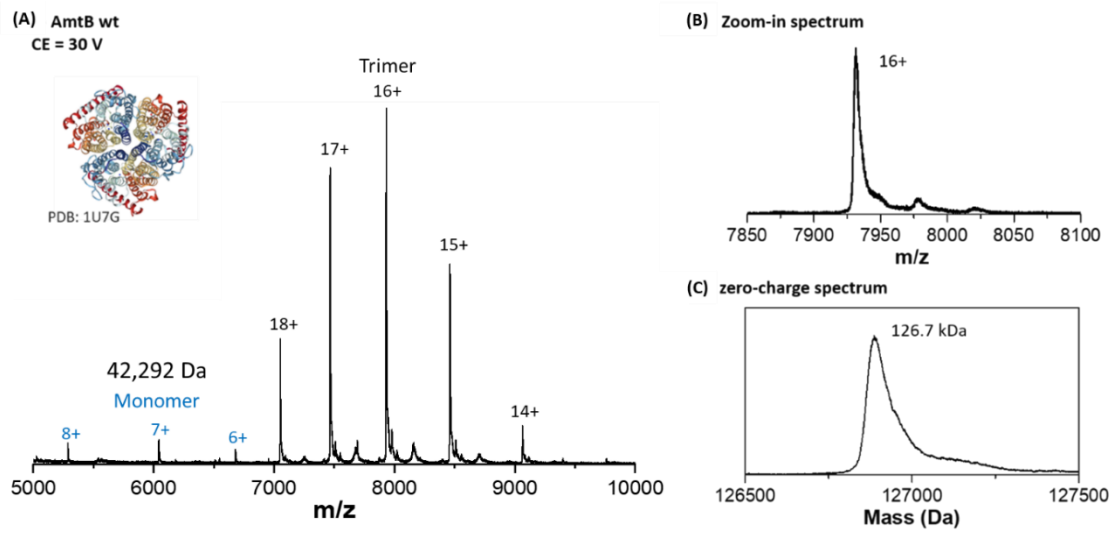

Figure 3.10. Mass spectra of wild type AmtB shows no β-ME binding. (A) Similar charge state distribution is observed for WT-AmtB as with the double-mutant AmtB, centered at 16^+ with low relative abundance monomer ions. (B) Expansion of the 16^+ trimer ions shows no β-ME binding. (C) Deconvolution of AmtB trimer signals reveals no β-ME binding.

3.3.3. Chaperonin Complex (GroEL)

Native mass spectrometry of GroEL, a homotetradecameric (14-mer) complex, further illustrates the utility of the modified instrument for studies of high MW, sub-MDa protein complexes.[53, 65, 133, 134] The native GroEL complex is observed in high relative abundance with well-resolved charge states when electrosprayed using mildly activating source potentials (**Figure 3.11(A)**). The measured mass determined under these conditions (801,088 Da) agrees well with the theoretical MW of the chaperonin complex (800,760. Da). The observed differences are consistent with nonspecific binding of salts and/or water molecules.[13, 53, 66] The CSD observed under these conditions, centered at 74^+, also agrees well with those presented by others using aqueous ammonium acetate solutions.[133-136]

The measured masses of the intact GroEL 14-mer ions are observed to shift to lower mass by ~644 Da under conditions where ISD occurs (**Figure 3.11(B)**). This is evidence for loss of non-covalent adducts, salts, and/or water bound to the surface or internal cavity of GroEL. ISD of GroEL also leads to ejection of high charge state monomers with a bimodal CSD (centered at 20^+ and 32^+). The bimodal CSD of the monomer ions also provides evidence of non-uniform dissociation processes and agree well with CSDs previously observed following CID (32^+) and SID (20^+).[65, 133] There are also low abundance signals corresponding to ejected dimer and trimer ions centered at 25^+ and 29^+, respectively. Dimer and trimer ions have been observed in previous studies of CID and by surface-induced dissociation (SID) of GroEL.[65, 134] The subunit MW derived from the CID fragment ions (57,198 Da), is in excellent agreement with the experimental subunit MW of the activated 14-mer (57,173 Da) and the theoretical subunit MW of GroEL (57,197 Da).

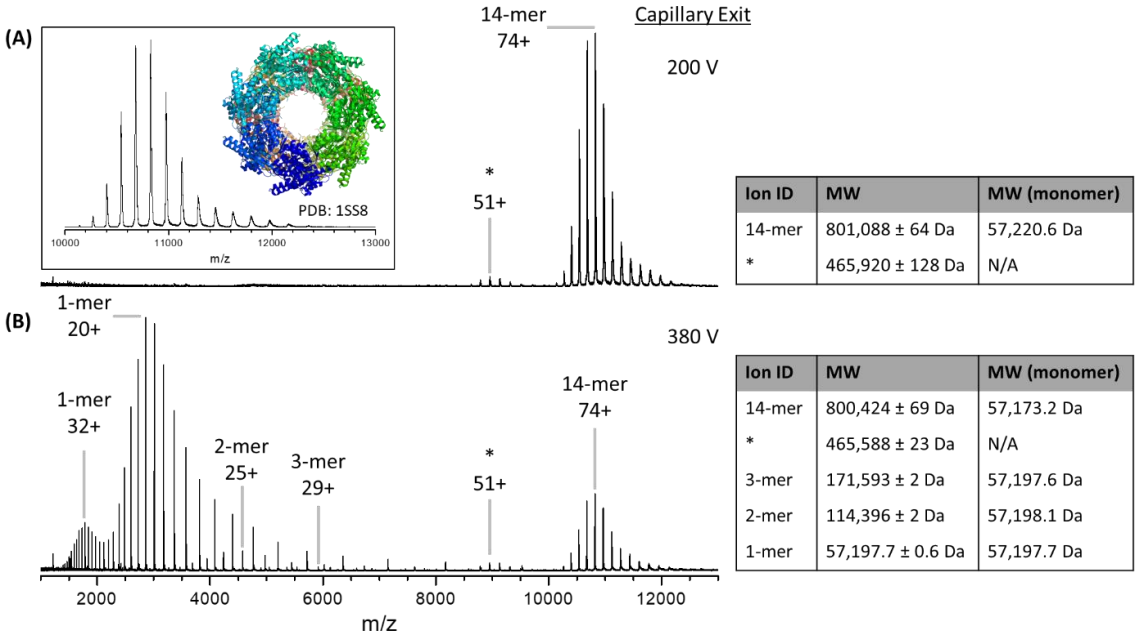

Figure 3.11. Native mass spectrum for GroEL. (A) Mass spectrum of GroEL obtained using low source potential nESI contains abundance signals for intact 14-mer complex centered at 74^+. The inset in (A) contains a narrow *m/z* range that illustrates the high resolution obtained for the intact 14-mer complex shown and the crystal structure of GroEL (PDB 1SS8). (B) In-source dissociation (ISD) mass spectrum of GroEL contains strong signals for unfolded and native-like monomer ions (charge states 20^+ and 32^+, respectively) as well as di- and tri-mer ions centered at 25^+, and 29^+, respectively. The measured MWs for each of the GroEL species are reported in the boxes. Note that the measured mass for the CSD labeled with an * (assigned as 51^+ ions with MW of 465.9 kDa) does not agree with any known ions derived from GroEL (see text). It is possible that this species could be an 8-mer of GroEL, as an intact 7-mer with a monomer trapped inside the cavity along with water, salts, and other small molecules.

Signals corresponding to a possible 8-mer (labeled with * in **Figure 3.11**) are observed at both low and high ISD collision energies, suggesting that the ions are not a product of GroEL 14-mer ions. The measured mass of these ions at high energy (465,588 ± 23 Da) would result from an octamer complex with subunit MW of 58,198.5 Da. While octameric ring complexes are common features of Group II chaperonins,[137] they are unlikely to coexpress with Group I chaperonins like GroEL. This species may be an

octamer of GroEL, wherein an unfolded monomer is bound to a 7-mer ring with the extra mass difference (*ca.* 1 kDa per subunit, 8 kDa total) due to salt, water, or small molecule binding to the interior and exterior of this complex. Further identification of the stoichiometry and topology of this contaminant species is ongoing.

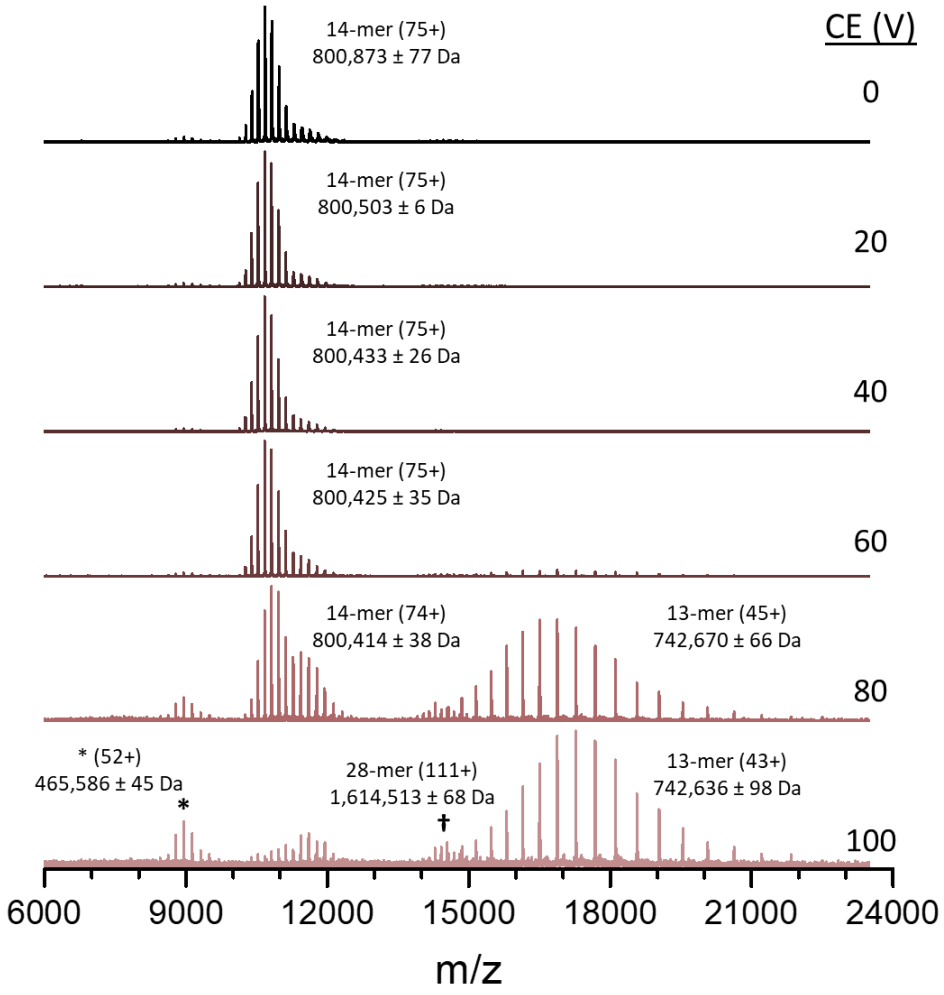

Figure 3.12. MS spectra of GroEL over a range of collision energy (CE) voltages. As the CE increases, both charge-stripping and CID are observed. Low abundance GroEL 28-mer ions appear at higher relative abundance at high collision voltage due to lower abundance of neighboring signals.

The native GroEL complex was also examined using different CID energies (**Figure 3.12**). Note that increasing the collision cell voltage from 20 to 60 V results in shifts of the measured mass of the GroEL owing to removal of adducted species. At higher CID energies charge stripping of the 14-mer ions is observed as evidenced by shifts in the CSD towards lower charge states. Alternatively, the relative abundance of lower charge state ions (higher *m/z*) increases at higher CE owing to depletion of higher charge state ions. Note that at CE of 60 V low abundance 13-mer ions are detected, and at CE greater than 80 V 13-mer ions centered at 45^+ are present in high abundances. When charge balanced, the CSD of the native 14-mer (CE 0 V, centered at 75^+) and charge-stripped 13-mer ions (CE 100 V, centered at 43^+) suggest the ejected monomer ions would be centered at 32^+ (*m/z* 1787.6), which agrees well with the results of ISD presented in **Figure 3.11(B)** as well as previously published tandem-MS spectra.[65, 135] While the monomer signal (centered at *m/z* 1787.6) is outside the mass range available when sampling up to 24,000 *m/z* on this instrument, some of the ejected monomer signal can be observed with the charge-stripped 13-mer when the upper *m/z* limit is reduced to to 20,000 *m/z* (see **Figure 3.13**). Overall, these results agree well with the observation of ejected monomer ions centered at 32^+ under conditions that promote dissociation (**Figure 3.11(B)**). It is interesting to note that no identifiable fragment ion, mass shifts, or charge-stripping product ions associated with the unidentified CSD noted in **Figure 3.11** are observed in **Figure 4.12** (labeled as *). It is unclear as to whether the abundances of these fragment ions are below the detection level, or that these ions are resistant to fragmentation. Also of interest is the detection of ions that are assigned to a GroEL 28-mer, a dimer of native

GroEL 14-mers. It is unclear as to whether the 28-mer is a native complex that might be formed by an ESI-induced dimerization. While there is no known biological significance of these GroEL dimers, their transmission, mass analysis, and detection further illustrate the potential of the Agilent 6545XT Q-TOF for studies of megadalton protein complexes.

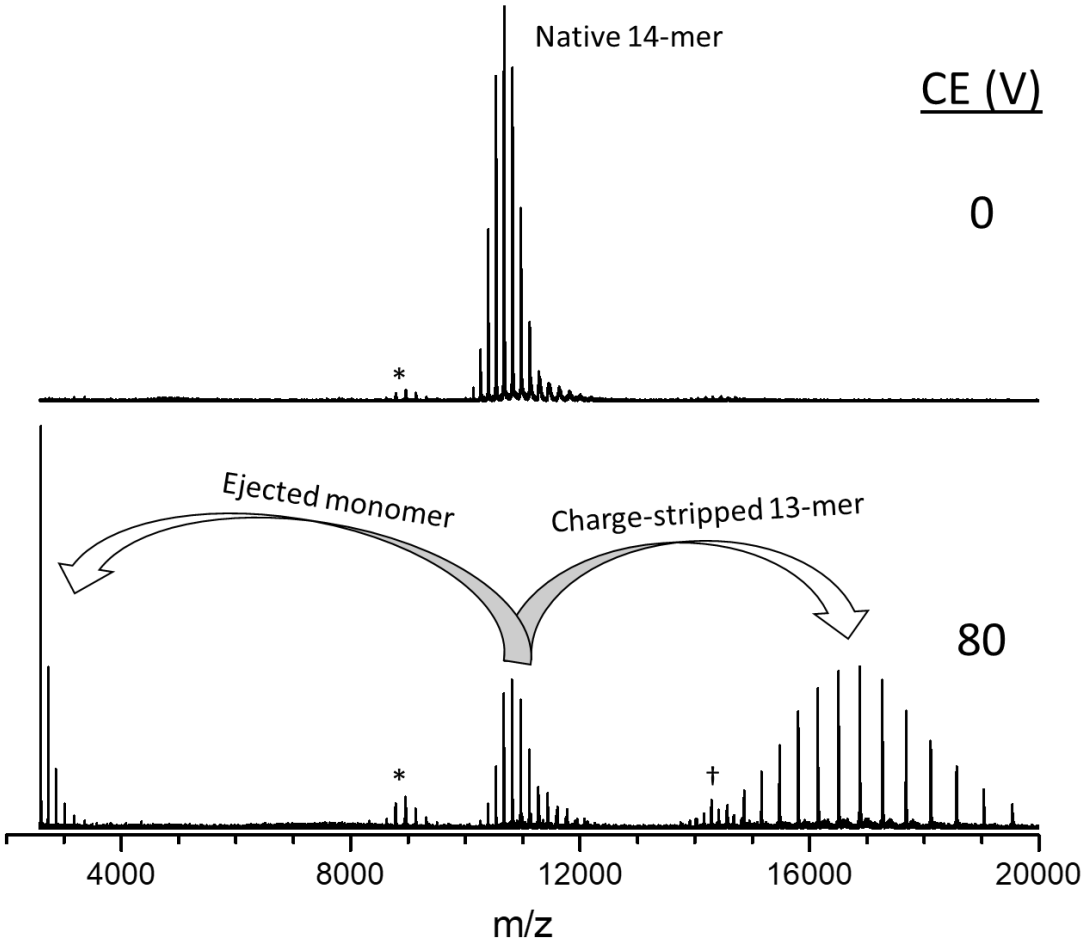

Figure 3.13. CID of GroEL was performed by increasing the collision energy (CE) from 0 to 80 V, leading to signals corresponding to monomer ejection and charge-stripped 13-mer ions. The instrument was tuned for simultaneous detection of both CID products. Low abundance ions corresponding to a 28-mer (labelled †) and possible 8-mer (labeled *) are observed at high CE.

3.4. Conclusion

MS studies of intact protein complexes require that they retain native contacts and minimal unfolding of the subunits as they undergo the transition from the native solution-phase environment to a solvent-free, gas phase ion. For soluble protein complexes, this transition involves the removal of solvent, whereas for membrane protein complexes both solvent and detergents/buffers must be removed. Great progress has been realized over the past 30 years since Ganem, Li and Henion[138] and Katta and Chait[139] first reported their studies on soluble, non-covalent protein complexes using ESI-MS. Subsequent developments in the ESI processes, in particular static ESI using nm to μm size emitters,[121, 122, 140] and MS instruments are now broadly recognized as native mass spectrometers.[16, 25, 141, 142]

Recent advances in Orbitrap MS instrumentation has opened new vistas for studies of larger protein complexes (>100 kDa.) and even MDa virus (>10 MDa.);[143] however, TOF-MS instruments are still widely used for native MS studies, especially for studies where quantitation is required.[144-146] To date, however, the mass resolution of most TOF-MS instruments is not sufficient for accurate determinations of MW of high mass complexes and efficient removal of solvent and salt adducts continues to be a challenge, especially for large protein complexes. The increased mass resolution and mass measurement accuracy of the Agilent 6545XT instrument is achieved by narrowing the pulse width for gating the ions into the TOF analyzer, increasing the length of the TOF, and decreasing the pressure within the TOF analyzer. The improvements in the instrument are most impactful for the analysis of larger ions (*i.e.* >100 kDa). because these ions are

prone to retaining small molecules, salt and/or water adducts during the transition to the gas phase.

Here, these advantages are illustrated by results for soluble and membrane protein complexes as well as the chaperonin GroEL ranging in sizes from ~127 kDa. to ~801 kDa. Increasing MS resolving power allows for analysis of smaller adducts, and the increase in sensitivity allows for detection of low abundance species, which may have biological relevance. The improved mass resolution of advanced TOF analyzers allows for more detailed analysis of multiply-charged ion distributions, thereby expanding characterization of sample heterogeneity.[12] In addition, the ability to perform ISD of these complexes affords a means for removal of some small molecule adducts, thereby allowing for more accurate determinations of molecular weight of the complex. ISD can also be used to dissociate the complex to better define the individual subunits of the complex. Collectively, these capabilities can be used to differentiate mass shifts resulting from PTMs and other sequence modifications and/or truncations.[37] These improvements will then open new opportunities toward the study and characterization of larger and more complex systems.

4. HUMAN IgG1κ CHARACTERIZATION BY HIGH-RESOLUTION MASS SPECTROMETRY REVEALS NEW GLYCAN HETEROGENEITY

4.1. Introduction

Glycosylated monoclonal antibodies (mAbs) are ubiquitous research targets for understanding disease mechanisms and designing therapeutics.[75] The topology of immunoglobulin gamma (IgG) mAbs is typically shown as a "Y"-shaped homodimer (H_2L_2) of heavy-light chain heterodimers (HL) (see **Figure 4.1**). For IgG1, the heavy chains (H) are each disulfide bound to one light chain (L), and the heavy chains are bound to each other with two disulfides located near the hinge region. The antigen-binding fragment (F_{ab}) domains for the branches of the "Y", where the structurally constant immunoglobulin domains of the heavy and light chains ($C_{H1\text{-}3}$ and C_L), are terminated in the variable heavy and light chains (V_H and V_L, respectively) responsible for antigen recognition and binding. The crystallizable fragment (F_c) then forms the base of the "Y" with two intra-heavy chain disulfides in IgG1 mAbs in the hinge region. IgG's are also glycosylated by *N*-linked glycans in this region with one glycan bound to each heavy chain at Asn299 in human IgG1κ. The heterogeneity of *N*-linked glycans is attributed to differing levels of enzymatic processing in the endoplasmic reticulum and Golgi *in vivo* with up to 36 possible resulting structures for N-linked glycans each differing by the number, identity, or linkage of the sugar residues.[147] With both heavy chains singly glycosylated, as is the case with most mAbs, the statistical heterogeneity leads to a possible 1,296 glycan combinations on intact structures.

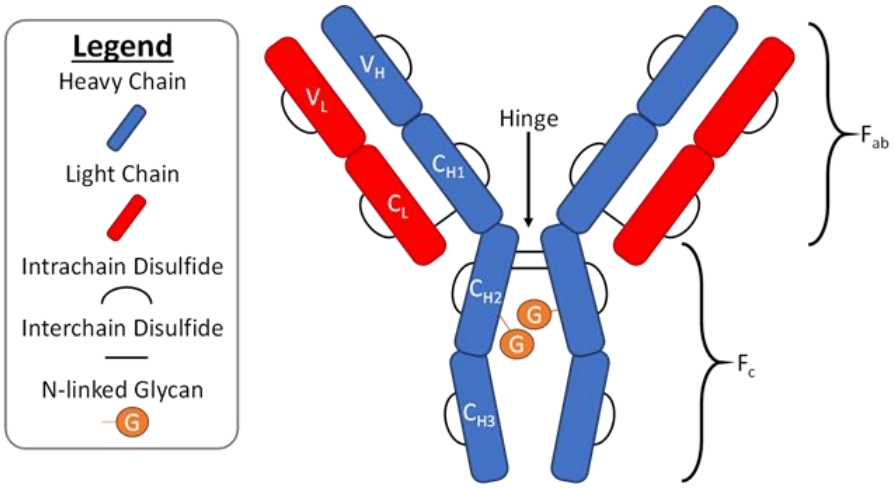

Figure 4.1. General structure of a glycosylated IgG1 mAb.

In human IgG mAb standards, the observed glycan patterns are typically denoted as G0F through G2F for each heavy chain with linked geometric symbols corresponding to different sugar residues.[148] The G0F nomenclature refers to a branched glycan structure containing four N-acetylglucosamine (GlcNAc) residues, three mannose (Man) residues, and one fucose (Fuc) residue bound to the base GlcNAc residue. This G0F glycan is formed following the loss of most of the antennary sugar residues. Sequential addition of up to two galactose (Gal) residues on each N-glycan is often observed; these glycans are denoted as G1F and G2F. Thus, for mAbs with two N-glycans, the five most abundant glycan combinations are often annotated in order of increasing mass as G0F/G0F, G0F/G1F, G1F/G1F (or G0F/G2F), G1F/G2F, and G2F/G2F.

While the antigen-binding specificity of immunoglobulins is typically located within the loops of the complementary-determining regions (CDR) at the end of the variable regions of the F_{ab} domains,[149, 150] there is growing evidence regarding the impact

of glycosylation of heavy chains on the structure of the F_c domain and, by proxy, the stability of the mAbs.[151-153] Identification of oligosaccharide structure, position, and quantitative abundance has created the field of glycomics;[154] however, glycomics methods often involve enzymatic release of glycans for structural identification and quantitation by LC-MS/MS analyses.[155] Methods for analysis of intact antibodies have also employed denaturing and/or reducing the antibodies.[75] Denaturing LC-MS methods often use acids and organic solvents to achieve better chromatographic separation and enhanced desolvation of intact mAbs into the mass spectrometer compared to non-denaturing (or native) LC-MS; however, these methods often produce broad charge-state distributions (CSDs) centered at high charge states owing to the increased solvent-accessible surface area of the denatured mAbs.[156] Antibody reduction methods are often used in conjunction with denaturing methods to solvent-expose and reduce the interchain disulfides to selectively separate and study the light chains, heavy chains, and light-heavy chain dimers, depending on the degree of disulfide reduction.[157]

While methods of antibody denaturation and/or reduction have worked previously, antibody analysis by native MS is also of particular interest to study the folded structure of immunoglobulins as well as antibody-drug conjugates (ADCs), where the harsh conditions used in denaturing MS may disrupt formation, ionization, and transmission of ADCs prior to mass analysis.[158] There is also growing concerns that analysis of denatured proteins by high resolution, Fourier transform-based MS or axially harmonic trapping MS (*e.g.* ion-cyclotron resonance MS or Orbitrap MS, respectively) suffers from significant losses in sensitivity compared to native MS. These losses have been attributed to the

increased collision-cross section of denatured antibodies (compared to native antibodies) owing to increased collisions in the orbitrap mass analyzer, reduced transient times, and decreased sensitivity and mass resolution.[159]

Common methods for interrogation of glycosylated mAbs includes reduction of intrachain disulfides with reducing reagents and/or treatment with deglycosylation enzymes. Reducing intrachain disulfides leads to the release of heavy and light chains from the mAb complex. MS analysis of these samples is often used to determine MW and sequence information. By reducing the intrachain disulfide bonds to thiols, the disulfide bond connecting the subunit heavy and light chains can be reduced to measure and compare the experimental chain MW to the theoretical MW of the known sequences. Deglycosylation enzymes are often used to remove or release glycans from mAbs by selective cleavage of asparagyl glycosidic and/or interglycan bonds. Following deglycosylation, the MW of the deglycosylated mAbs can be compared against the theoretical sequence and/or the released glycans can be analyzed by LC-MS/MS methods to determine specific glycan structure based on fragmentation patterns of chromatographically separated released glycans.

Herein, we show that when electrosprayed from native-like buffers, intact human IgG1κ mAbs from myeloma plasma reveal glycan heterogeneity that has not been previously observed. In-source trapping (IST) instrument tune settings produce clean, well-resolved IgG ion signals for baseline-resolved glycans for the intact mAbs. In addition, we observe a resolved mass shoulder on each of the intact glycosylated mAb peaks differing from the dominant mass signals by ~40 Da. These mass shoulders are

tentatively assigned as substitutions of GlcNAc residues for Man or Gal residues in the N-glycan structures. While the specific identification of the structure of these glycans is unknown, the resolving power achieved herein provides the foundation for future high-resolution analyses of native, intact antibodies and interpretation of glycan and other heterogeneity.

4.2. EXPERIMENTAL

4.2.1. Sample Preparation

Human IgG1κ from myeloma plasma was obtained as a frozen, buffered solution from Sigma-Aldrich (St. Louis, MO). Upon arrival, the samples were defrosted, separated into 75 μL aliquots, and flash frozen to prevent unnecessary freeze-thaw cycles for future experiments. Ammonium acetate (AmA), triethylammonium acetate (TEAA), dithiothreitol (DTT), and tris(2-carboxyethyl)phosphine (TCEP) were obtained from Sigma. Deglycosylation enzymes were expressed and purified by the Laganowsky group at Texas A&M University. To prepare the mAb samples for nMS analysis, the buffered antibody aliquots were defrosted and diluted to 1 μM prior to desalting into 200 mM AmA using Micro BioSpin P-6 columns (BioRad). For the charge-reducing experiment, the IgG samples in 200 mM AmA were supplemented with 50 mM TEAA. For deglycosylation, the antibody-enzyme solutions were mixed, desalted, and allowed to incubate overnight at room temperature prior to mass analysis. For disulfide reduction, 1 mM of TCEP or DTT was added to the desalted IgG sample and loaded into a static spray emitter needle. This emitter was then incubated in a variable-temperature static nESI source[160] at ~50°C

for several minutes to capture the loss of the light and/or heavy chains prior to sample aggregation.[161]

4.2.2. Instrumental Analysis

The MS analyses were carried out using a ThermoFisher Q-Exactive Plus UHMR (Bremen, Germany) mass spectrometer. ESI was facilitated using borosilicate glass capillaries pulled with a Flaming-Brown micropipette puller (P-1000, Sutter Instruments) to an O.D. of ~5 μm. ESI voltage was set to ~1.5 kV with a platinum wire inserted into the solution. The instrument was mass calibrated using CsI. The instrument was tuned by varying the desolvation energy from 0 to -300 V with in-source trapping mode enabled to enhance desolvation and removal of non-specific adducts prior to injection into the C-trap. The mass resolution was set to 25,000 to achieve efficient mass-to-charge separation of neighboring glycan signals while minimizing mass spectral artifacts. The best resolution/sensitivity was achieved with of desolvation energy set to -300 V while acquiring at a set mass resolution of 25,000 at *m/z* 200.

4.2.3. Data Processing

Data were initially extracted in Thermo Qual Software. UniDec was used to convert MS data files from .RAW to .txt files for visualization.[162] Mass spectral deconvolution was performed using ProteinMetrics-Intact with peak sharpening enabled with a point spread function of 10 Da.[163] Figures were prepared using OriginPro 2021. Calculation of theoretical molecular weight (MW) of the intact antibodies was performed using ChemCalc's online tools[109] with the available sequences for human IgG1κ heavy and light chains from UniProt (P0DOX7 and P0DOX5).[164]

4.3. RESULTS

4.3.1. Optimization of Native, Intact IgG1κ MS Signals

In-source trapping (IST) and collisional activation were first used to activate and remove residual nonspecific adducts from the IgG1κ ions. Increasing the magnitude of desolvation energy potentials from 0 to -400 V results in IgG ions with fewer bound adducts and with charge-state distributions (CSDs) shifted towards higher *m/z* (see **Figure 4.2(A)**). At desolvation potentials below -200V, neighboring glycan signals become baseline-resolved for IgG1κ^{22+} ions as shown in **Figure 4.2(B)**. The shoulder signals observed on each glycan peak at these high source energies have not been previously observed and is revealed in large part due to the combination of IST and the high practical mass resolution afforded by the Orbitrap mass analyzer.

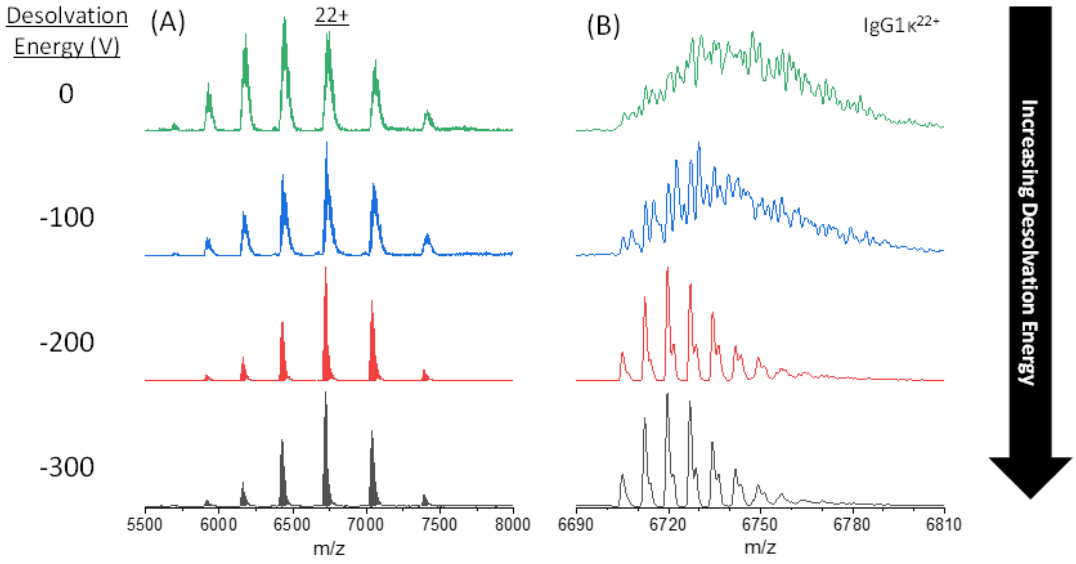

Figure 4.2. Effects of in-source trapping desolvation energy on spectral quality. **(A)** Increasing the magnitude of desolvation energy results in mass spectra with lower average charge. **(B)** As desolvation energy is increased to its maximum value of -300V, glycan signals become baseline resolved to reveal previously unresolved glycan microheterogeneity at a set resolution of 25,000 at 200 *m/z*.

In the experiments shown herein, mass resolution of 25,000 at *m/z* 200 reveals details that are hidden at lower mass resolutions. As shown in **Figure 4.3**, while changing the set mass resolution does not affect the observed CSDs (**Figure 4.3(A)**), at low and high resolution, the observed signal-to-noise ratio (SNR) decreases as the spectral baseline increases as shown in **Figure 4.3(B)** for IgG1κ^{23+} ions. The glycan mass heterogeneity revealed at high resolution for the mass shoulder signals is only well-resolved at a mass resolution of 25,000 (**Figure 4.3(B)**, red trace), although *m/z* signals for the various glycan signals on IgG1κ^{23+} are observed with non-normal distributions at lower resolution (12,500, **Figure 4.3(B)**, blue trace). When increasing the mass resolution to 50,000, mass spectral artifact peaks resulting from spectral leakage result in decreased sensitivity and SNR.[165]

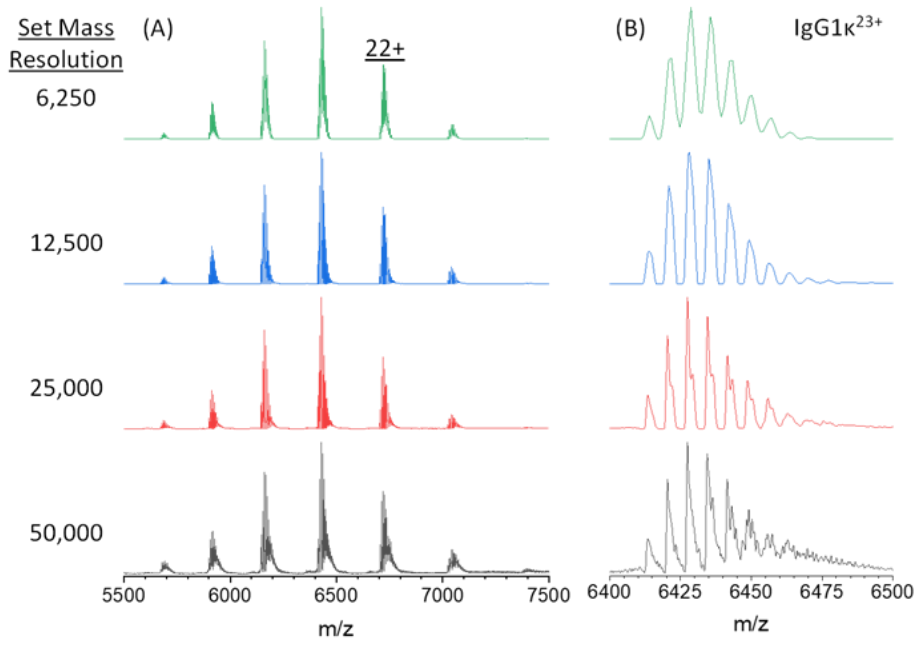

Figure 4.3. The set mass resolution was increased to increase resolution of neighboring glycan signals. **(A)** At low and high mass resolution (6,250 and 50,000, respectively), baseline signal increases, reducing sensitivity. **(B)** Expanded mass spectra for the IgG1κ^{23+} ions reveal baseline resolved glycan signals for spectra collected at 12,500 and 25,000 set resolution. The signal obtained at 25,000 provided the best signal-to-noise ratio and resolving power while minimizing mass spectral artifacts.

Previous native MS studies of proteins and protein complexes have benefitted from the addition of charge-reducing reagents to increase spacing between neighboring mass peaks by reducing the charge component (*z*) of their respective *m/z* differences.[116, 117, 166] Results from mass deconvolution (with algorithmic peak sharpening enabled) from an AmA-buffered control sample and a *z*-reduced sample containing an additional 50 mM TEAA are shown in **Figure 4.4**. While the addition of TEAA shifts the CSD centroid from 23+ (in AmA) to 17+ (spectra not shown), the apparent gains in resolution of neighboring glycan signals in minimal. In addition, the resolution of the glycan shoulder signals decreases slightly following addition of TEAA as observed by a decreased valley depth

between the sharpened shoulder. This may be a result of less efficient ionization (or transmission) of the lower-charge ions leading to decreased sensitivity; however, the overall MW of the identified features does not change significantly for the most abundant deconvolved signals.

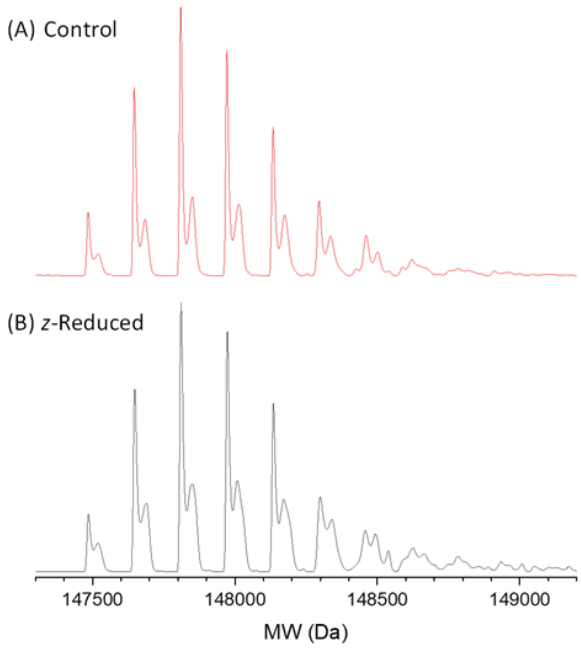

Figure 4.4. Charge reduction was implemented as an attempt to increase the apparent sensitivity and resolution of neighboring glycan signals. To a control sample in AmA **(A)**, TEAA was added as a charge-reducing cosolute. Results from mass deconvolution with peak sharpening enabled show worse resolution of neighboring glycans in the z-reduced sample **(B)**.

4.3.2. ProteinMetrics Deconvolution and Peak Sharpening

Peak sharpening is achieved through application of Richardson-Lucy deconvolution with a point spread function set herein to 10 Da.[163] Unsharpened deconvolved mass spectra primarily reveals mass differences between neighboring, baseline-resolved signals of 162.4±0.8 Da for the first 6 mass peaks (see **Figure 4.5(A)**,

black arrows). These differences are attributed to increasing numbers of galactose (Gal) or mannose (Man) glycans with theoretical glycan residue masses of 162.1 Da. After enabling peak sharpening, resolution of the shouldering signals allows for identification of new mass differences at lower relative abundance, featuring a series of Gal/Man additions with average mass differences of 162.7±1.6 Da (**Figure 4.5(B)**, blue arrows).

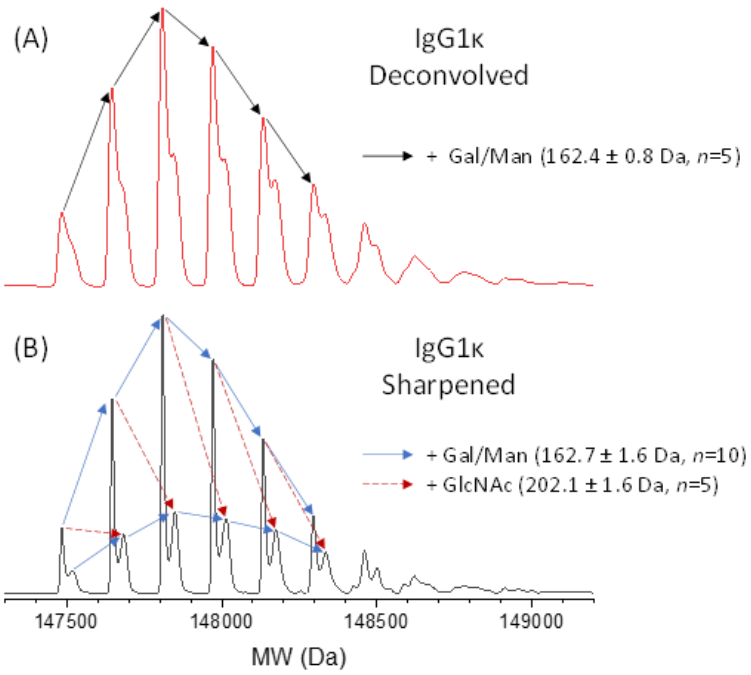

Figure 4.5. (A) Mass deconvolution without peak sharpening reveals neighboring signals differing by 162.4±0.8 Da, corresponding to sequential addition of Gal/Man glycans. **(B)** Mass deconvolution with peak sharpening enabled reveals additional signals separated by the mass of Gal/Man glycans (162.7±1.6 Da) as well as signals separated by the mass of GlcNAc glycans (202.1±1.6 Da).

The mass difference between the main peak and sharpened shoulder of the adjacent baseline-resolved cluster (**Figure 4.5(B)**, red arrow) is calculated as 202.1±1.6 Da. These mass differences were initially assigned to increasing numbers of *N*-acetylglucosamine glycan residues (GlcNAc; theoretical residue mass of 203.2 Da). While specific structural

assignments of these glycans is tentative without further confirmation by bottom-up and/or middle-down glycomics experiments, we note that the glycans assigned to the mass differences are within <1 standard deviation of their theoretical MWs. Careful comparison of these mass/glycan shifts with known structures of N-linked high mannose and hybrid glycans on human mAbs does not allow a simple identification of the bound glycan structural heterogeneity. Due to the highly conserved enzymatic mechanisms for *N*-glycosylation,[77, 147] it appears unlikely that Gal or Man residues could be substituted for GlcNAc *in vivo*.

The mass difference between the main and shoulder pair of the baseline-resolved glycan mass clusters is *ca.* 40 Da, which does not correspond with an intuitive post-translational modification (PTM) *a priori*; however, we cannot rule out certain point mutations (e.g. P→G, S→Q, H→P, D→R) which may lead to an increase in mass of *ca.* 40-42 Da. Additional theoretical point mutation mass deltas are calculated and shown in **Table 4.1**. The assignment of the mass shifts as metal cation adducts (e.g. K^+ or Ca^{2+}) is also possible; however, these metal adducts would likely replace charge carriers (*viz.* K^+ or Ca^{2+} would substitute one or two protons, respectively) leading to mass differences closer to *ca*. 38 Da.

Table 4.1. Mass deltas were calculated for theoretical point mutations and are shown as the difference between the "high mass" residue and the "low mass residue". Mass deltas of 40-42 Da are *highlighted*.

			"High Mass" Residue																		
			G	A	S	P	V	T	C	I	L	N	D	Q	E	H	F	U	R	Y	W
		MW	57	71	87	97	99	101	103	113	113	114	115	128	129	137	147	150	156	163	186
"Low Mass" Residue	G	57	0	14	30	**40**	**42**	44	46	56	56	57	58	71	72	80	90	93	99	106	129
	A	71		0	16	26	28	30	32	**42**	**42**	43	44	57	58	66	76	79	85	92	115
	S	87			0	10	12	14	16	26	26	27	28	**41**	**42**	50	60	63	69	76	99
	P	97				0	2	4	6	16	16	17	18	31	32	**40**	50	53	59	66	89
	V	99					0	2	4	14	14	15	16	29	30	38	48	51	57	64	87
	T	101						0	2	12	12	13	14	27	28	36	46	49	55	62	85
	C	103							0	10	10	11	12	25	26	34	44	47	53	60	83
	I	113								0	0	1	2	15	16	24	34	37	43	50	73
	L	113									0	1	2	15	16	24	34	37	43	50	73
	N	114										0	1	14	15	23	33	36	**42**	49	72
	D	115											0	13	14	22	32	35	**41**	48	71
	Q	128												0	1	9	19	22	28	35	58
	E	129													0	8	18	21	27	34	57
	H	137														0	10	13	19	26	49
	F	147															0	3	9	16	39
	U	150																0	6	13	36
	R	156																	0	7	30
	Y	163																		0	23
	W	186																			0

4.3.3. Application of Glycomics Approaches

Figure 4.6 contains the deconvolved mass spectra from samples incubated with deglycosidase enzymes PNGase F and Endo H (see panels (B) & (C), respectively). PNGase F removes the entire *N*-linked oligosaccharides from glycoproteins through enzymatic cleavage between the innermost GlcNAc and asparagine residues. Glycan cleavage following incubation with PNGase F should reduce the heterogeneity of the deconvolved MS spectra down to a single mass peak owing the fully degylcosylated mAb, with a theoretical MW of 145,056 Da. Instead, a truncation of the IgG1κ is observed as the distribution of glycosylated signals shifts by 2881.2 Da or 1440.6 Da per glycan without much change in the relative abundance of the neighboring glycan signals. The low MW glycans from the control (**Figure 4.6(A)**) and PNGase F (**Figure 4.6(B)**) incubated

samples are measured as 147,485.4 and 144,604.2 Da, respectively. While the expected mass loss from cleavage of two G0F N-glycans is 2,890 Da and could explain the observed mass shift, deglycosylation should result in a much more homogeneous spectrum. These results suggest that the enzymatic activity of PNGase F did not proceed as expected based on its known deglycosylating activity. In addition, many of the deconvolved mass signals from PNGase F incubation are below the calculated theoretical MW of the degylcosylated IgG1κ ions (shown as a vertical red line in **Figure 4.6(B)**), which suggests that the sequence used to calculate the theoretical MW may be incorrect.

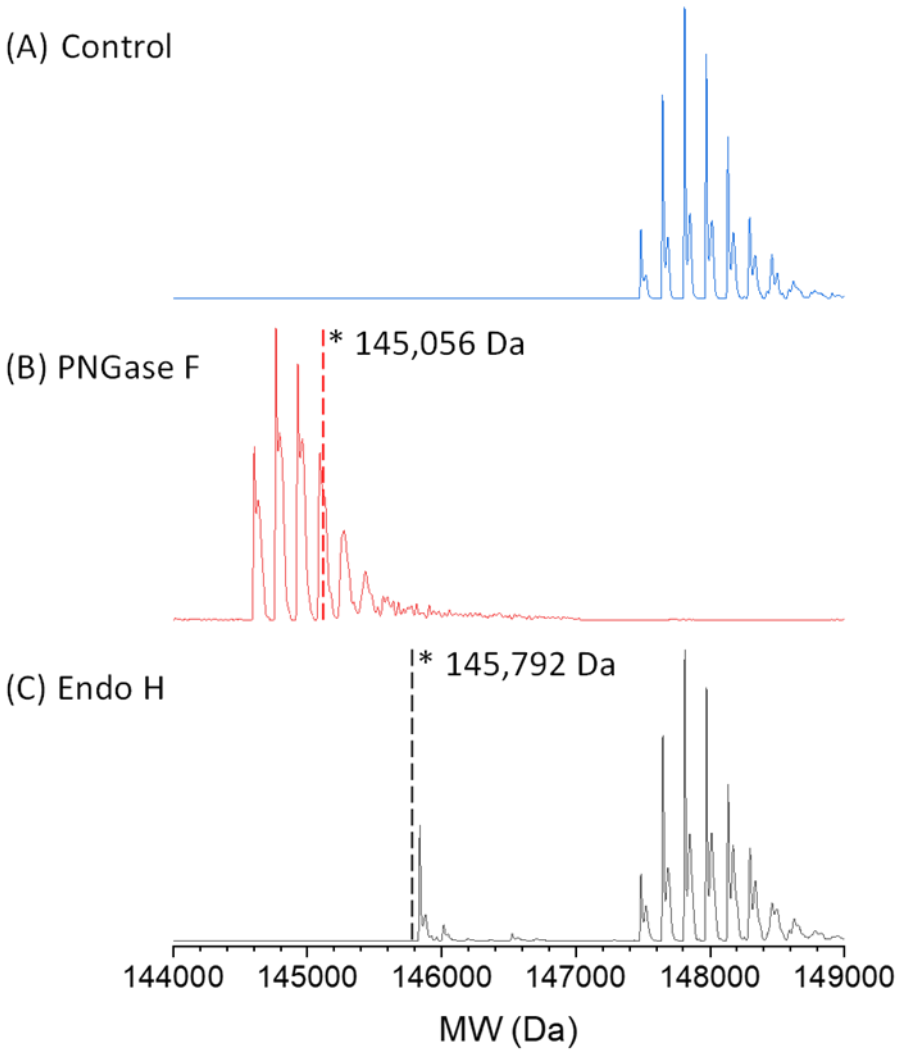

Figure 4.6. Incubation with deglycosylation enzymes resulted in mass shift from **(A)** the unreacted control to samples incubated with **(B)** PNGase F and **(C)** Endo H enzymes. The vertical dashed lines represent the theoretical MW of the IgG1κ following full deglycosylation with PNGase F and partial deglycosylation with Endo H (panels **(B)** & **(C)**, respectively.

The Endoglycosidase H (Endo H) enzyme was used to cleave between to GlcNAc subunits proximal to the N-linked asparagine residue, leaving one N-linked GlcNAc residue without disrupting the possible fucose residue bound to the remaining GlcNAc. The deconvolved mass spectra resulting from incubation of IgG1κ with Endo H is shown

in **Figure 4.6(C)** and shows signals for unreacted IgG1κ and some signal for deglycosylated mAb. The theoretical MW of IgG1κ with one GlcNAc-Fuc residue on each heavy chain was calculated as 145,792 Da. The measured MW of the deglysoylated IgG1κ is measured as 145,838 Da. These MW values agree within 46 Da (~300 ppm error) and suggest that the N-glycans on IgG1κ may be fucosylated; however, the base glycan for fucosylated N-glycans is typically observed as G0F/G0F. The theoretical MW of this combination is 147,982 Da, which does not agree with the observed low-mass glycan-bound IgG1κ MW of 147,485 Da (difference of 497 Da). The theoretical G0F/G0F MW best agrees with the fourth major glycan signal that has a measured MW of 147,973 Da (difference of 9 Da); however, their assignment by comparison with the theoretical MW is purely speculative, and the mass shifts to neighboring glycan signals do not agree with expected N-glycan heterogeneity in human mAbs *in vivo*. Future work will include evaluation with additional deglycosylase enzymes and follow-up bottom-up glycomics of the released glycans to further evaluate their structure.

4.3.4. Reduction of IgG1κ

To isolate the differences between the experimentally measured and theoretical sequences to the heavy and/or light chains of IgG1κ, disulfide reducing reagents (e.g. TCEP and DTT) were used to covalently separate and measure the MW of the heavy and light chains of IgG1κ. As shown in **Figure 4.7(A)**, incubation with TCEP results in minimal disulfide reduction as very little additional signal is observed in the deconvolved spectra for mAbs other than the intact H_2L_2 complex. Following incubation with DTT (shown in **Figure 4.7(B)**), additional signals for the H_2L complex are observed at *ca.* 125

kDa. The mass difference between the least glycosylated mAb signals for the H_2L_2 and H_2L was calculated to be 23.41 kDa which agrees well with the theoretical MW of one light chain (23.38 kDa). These results suggest that if there are sequence differences between the known sequence of human IgG1κ and the sample used herein, that these sequence modifications are likely localized to the heavy chains.

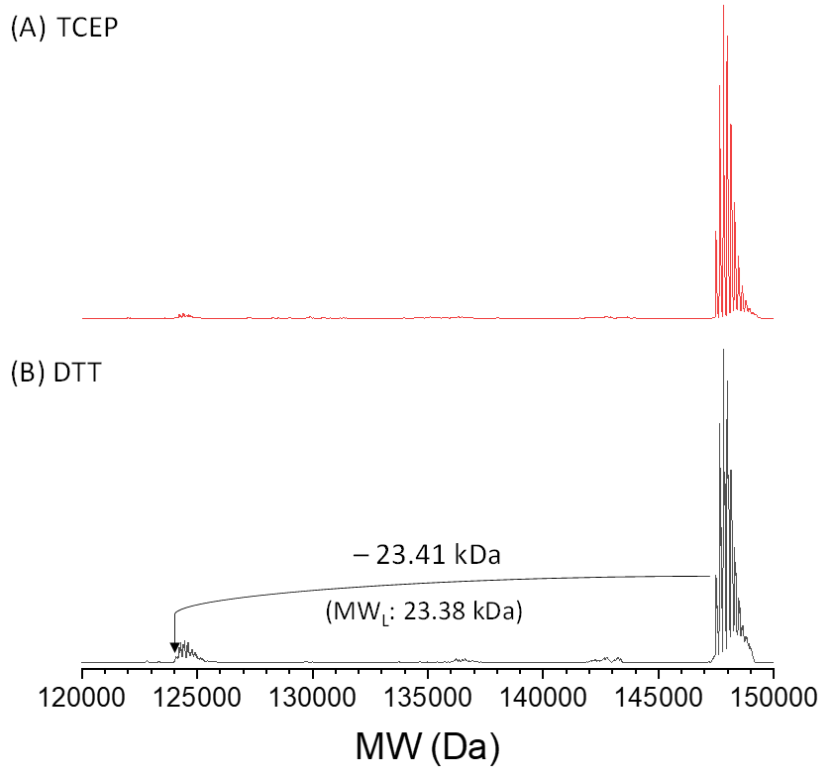

Figure 4.7. Deconvolved mass spectra following incubation of IgG1κ with **(A)** TCEP and **(B)** DTT are shown. DTT incubation results in greater disulfide reduction efficiency as signals for the loss of a light chain from IgG1κ are observed.

4.4. Discussion

Identification of glycan heterogeneity of intact mAbs by high-resolution, native MS represents a growing field of biopharmaceutical research as these glycans can affect

mAb structure and function; however, to take advantage of high mass resolution, mAbs must be ionized and transmitted while retaining few, if any, nonspecific solvent and/or salt adducts. Herein, we find that algorithmic peak sharpening of deconvolved mass spectra, a unique feature of the ProteinMetrics-Intact software suite, can be used to increase resolution of mass shoulder signals in the deconvolved mass spectra of IgG1κ. These mass shoulders are ~40 Da heavier than their neighboring glycoprotein mass signals. Disulfide reduction and deglycosylation experiments were performed to provide more insight into the structural heterogeneity of these human IgG1κ mAbs to answer two primary questions: (1) does treatment with deglycosylating enzymes result in the loss of glycans commonly observed in IgG1κ mAbs, and (2) can disulfide reduction be used to localize sequence misinformation to the light or heavy chains? Results from incubation with deglycosylase enzymes were largely inconclusive, and similar mass shoulders were observed on the partially deglycosylated mAb mass signals. Reduction of IgG1κ with DTT leads to loss of one light chain in good agreement with its theoretical MW. This then suggests that the observed mass shifts may be localized to the heavy chain sequence. Point mutations in the variable heavy and light immunoglobulin domains (V_H and V_L, respectively from **Figure 4.1**) may produce the observed 40 Da mass shifts. Mutant residues can affect antigen binding specificity, especially if these point mutations are localized within the so-called complementarity-determining region (CDR) loops.[149] Finally, at this time, we cannot rule out the possibility of metal cation adducts. Exchanging charge-carrying protons with K^+ or Ca^{2+} cations would produce a nominal mass shift of 38 Da. Although this theoretical metal mass shift is not accurate to the observed 40 Da

shift, current studies are ongoing to evaluate potential cooperative binding of metals to these mAbs.

4.5. Conclusion

Intact analysis of glycosylated mAbs by high-resolution MS is becoming more routine in biopharmaceutical research to determine their representative sequences and glycan structural variants. While analytical methods using denatured mAbs is more traditional,[167-169] sensitivity and SNR decreases from denatured protein analysis may limit the practical mass resolution from axial harmonic trapping-based MS instruments (i.e. Orbitrap MS). Intact MS analysis of glycosylated IgG1κ from human myeloma plasma from native-like buffers (e.g. ammonium acetate) produces spectra with previously unseen microheterogeneity in the deconvolved mass spectra. While the identification of the mass shifts is ongoing, the mass shifts between neighboring abundant glycan signals agrees well with subsequent addition (or removal) of Gal residues as is commonly observed in human mAbs. However, the additional mass shifts that agree with the addition (or removal) of GlcNAc has not been observed on other published work on intact analyses of glycosylated mAbs. That said, we tentatively note that the mass shifts between neighboring signals may result from singly mutated sequence variants and/or binding of metal cations.

Results from incubation with deglycosylase enzymes suggest that the glycans on IgG1κ may be fucosylated which is not uncommon for human IgG mAbs; however, the measured intact MW of the glycosylated IgG1κ ions do not agree with the theoretical MW of commonly observed N-glycan distributions (G0F/G0F, G0F/G1F, G1F/G1F, etc.). This

suggests that (1) the N-glycan distribution contains an unexpected mix of different glycan types (e.g. high mannose, hybrid), or (2) the human IgG1κ sequence used to calculate the theoretical MW did not match the actual sequence of the mAb studied herein due to sequence variants and/or truncations. To isolate the potential sequence errors to the heavy or light chain, disulfide reduction experiments were performed. Results from these experiments suggest that the light MW matches the theoretical MW of the known sequence, thereby isolating potential sequence modifications to the heavy chains. Future work will include further bottom-up glycomics analysis of the released glycans and top/middle-down proteomic analyses of the IgG1κ heavy chains to characterize the mass shift, and application of these methodologies towards characterization of IgG1λ mAb from human myeloma plasma.

5. CONTRIBUTIONS TOWARD CROSS-LABORATORY EVALUATION OF ION OPTICS FOR COLLISION-INDUCED UNFOLDING OF PROTEINS AND PROTEIN COMPLEXES

5.1. Introduction

Ion mobility-mass spectrometry (IM-MS) is increasingly used to study the structure of proteins and protein complexes in the gas-phase.[170, 171] While MS provides information on the mass and structural heterogeneity encoded in ions' respective mass-to-charge ratios (*m/z*), IMS can yield information regarding gas-phase shape and/or structure. IMS devices provide separation based on differences in the interaction of ions with a weak electric field and a neutral buffer gas. IMS allows for the separation of ions based on their charge and size/shape due to their differing interactions with the weak electric field and friction forces from interaction with the buffer gas. This separation results in separation of ions and determination of an arrival time distribution (ATD) that can be converted to an ion-neutral collision cross section (CCS) for comparison between different experimental conditions.[38] Encoded in the CCS is the rotationally averaged surface area of the ions of interest, and for proteins or protein complexes, this CCS will remain small for folded or compact ions and will increase for unfolded or denatured ions.

Native IM-MS (nIM-MS) allows for the determination of ion CCS while retaining non-covalent interactions (e.g. H-bonds, salt bridges, hydrophobic interactions) through ionization and desolvation to the gas-phase ions while maintaining secondary, tertiary, and quaternary protein structure.[67] nIM-MS is primarily facilitated in two parts: (1)

electrospray from nondenaturing buffers[16] and (2) minimizing effects of pre-IMS collisional activation in the gas phase.[21, 26] In nIM-MS, the experimental ion CCS can be compared to CCS values calculated from condensed-phase structures as determined by nuclear magnetic resonance spectroscopy, x-ray diffraction crystallography, and/or cryogenic electron microscopy.[44, 49-52, 54, 55, 172]

The CCS distributions observed for proteins and protein complexes can be important for comparisons following ligand, substrate, or metal binding;[173-176] however, for many systems, the ground-state CCS distributions do not significantly change.[70, 177] Experiments implementing collisional activation (CA) of protein ions prior to IMS analysis have been employed to survey the gas-phase conformational landscape of many proteins and protein complexes.[178] This collision-induced unfolding (CIU) allows for the interrogation of partially and completely unfolded conformers resulting from progressive CA of gas-phase ions with background gas molecules. By plotting the ATD of these ions as a function of their collision energy or instrument potential, CIU fingerprints or heatmaps can show shifts in ATD or CCS as a function of collision energy.[70] Identification and fitting of the observed IM features following CIU can then be used to compare CCS values of ground-state and unfolded features, and comparison of the transition energies between different features can inform on effects of structural (de-)stabilization of the respective ions in the gas phase.[69]

Much of the modern CIU-based studies have employed the use of Waters SYNAPT traveling wave-IMS (TWIMS) instrumentation. This is largely due to (1) the SYNAPT was the first commercialized IM-MS platform, allowing for more widespread

access to IM experimentation without the need for home-built instrumentation, (2) the relative ease of performing CIU experiments by simply varying the trap CE potentials in the MassLynx software, and (3) the ability to perform quadrupolar mass selection prior to activation and TWIM analysis.

More recently, Agilent Technologies has developed a uniform field, drift tube IMS (DTIMS) instrument with sampling capabilities up to 20,000 *m/z*. This platform allows for calculation of ion CCS values without the need for external calibrants as the experimental drift times can be directly converted to CCS using the Mason-Schamp equation based on first-principles ion-neutral collision dynamics.[38] Following further research and development, Agilent has partially redesigned the source ion optics to facilitate ion activation (and CIU) prior to DTIMS separation. This has allowed for CIU experiments to be performed on this platform with its high-mass capabilities to probe protein complexes, antibodies, chaperonin ions in academic studies.[120, 179, 180]

One area of concern then is the interlaboratory reproducibility of CIU results collected on this DTIMS instrument. Previously, interlaboratory studies were conducted to evaluate the robustness of the ground-state CCS determinations with great success for small molecule standards (CCS RSD 0.29%)[181] and small and large native protein and protein complex ions (CCS RSD 0.43%)[179] with great success. To test the reproducibility of CIU results collected using a new prototype desolvation assembly prior to commercialization, an interlaboratory study was designed using Agilent 6560 IM-Q-TOF instruments equipped with prototype source ion optics at Texas A&M University, University of Michigan, Vanderbilt University, and Agilent Technologies in Santa Clara,

CA. These optics were evaluated using proteins and protein complexes as standards which have been used previously in CIU experiments.

5.2. Methods

5.2.1. Sample Preparation

Ammonium acetate (AmA), bovine ubiquitin (Ubq), horse heart myoglobin (Myo), bovine serum albumin (BSA), streptavidin from *Streptomyces avidinii* (SA), and Sigma SiLuLite IgG1 standard (IgG1) were purchased from Millipore-Sigma (St. Louis, MO). Lyophilized protein samples were acquired at University of Michigan, dissolved to 5 μM in 200 mM AmA at pH ~7.2, aliquoted, flash frozen, and shipped to each laboratory. Prior to IM-MS analysis, the frozen aliquots were defrosted and desalted to fresh 200 mM AmA using Micro BioSpin P-6 columns (BioRad Hercules, CA). Ubiquitin samples were not desalted due to sample loss near the molecular weight cut-off of the BioSpin columns.

5.2.2. IM-MS

The Agilent 6560 IM-Q-TOF used in this study was equipped with a second-generation prototype desolvation assembly and power supplies to facilitate higher energy CA of ions for CIU. This source incorporates a ring electrode immediately following the ion transfer capillary exit prior to entrance of ions into the high-pressure funnel region. By increasing the potential offset between the capillary exit and ring electrode, increasing degrees of CA can be imparted on ions prior to refocusing, trapping, and release into the DTIMS analyzer. This prototype allows for significant CIU of protein ions without the

addition of heavier dopant gases (e.g. Ar, SF_6) as was required by earlier prototypes.[120, 179, 180]

All samples were introduced to the Agilent 6560 by direct infusion ESI using a microflow nebulizer at flow rates of 1-5 μL/min with the following ESI source settings: ion transfer capillary voltage, 2.5-3.5 kV; ion focusing nozzle voltage, 1-2 kV; drying gas flow, 5 L/min; drying gas temperature, 140°C; sheath gas flow, 11 L/min; sheath gas temperature, 140°C. The high-pressure funnel was maintained at ~4.80 Torr, the trapping funnel was set to ~3.80 Torr, and the DT pressure was set to ~3.95 Torr for all experiments. Desolvation, drying, and drift gases all employed high-purity N_2. The default DT entrance and exit potentials were used (1700 V and 250 V, respectively). The maximum drift time was set to capture all features for each analyte, the trap fill time was set to 10 ms shorter than the maximum drift time, and the trap release time was set to 1 ms for all experiments. Following the manufacturer suggested protocols for single-field CCS calibration, TuneMix ions were electrosprayed using the microflow nebulizer with the In-Source CE set to 0 V, and their ATDs were collected under the same tune conditions used in the CIU studies.

5.2.3. Collision-Induced Unfolding

CIU experiments were performed by sequential increase of the In-Source CE potential in MassHunter Acquisition (B.10.1) without addition of dopant gasses into the drying gas (N_2) stream. The In-Source CE potentials were increased in 10 V increments from 0 to 450 V in most experiments or until signal for intact ions was depleted. Increasing

the In-Source CE potential beyond 450 V generally lead to electrical breakdown in the source region at the set pressures and temperatures used herein.

5.2.4. Data Processing

IM-MS spectra for TuneMix ions were initially analyzed in Agilent IM-MS Browser (B.08) to determine t_{fix} and β parameters for the single-field CCS calculations in CIUSuite2 following established protocols.[78] CIU IM-MS data were analyzed in IM-MS Browser (B.08.00) and/or MassHunter Qualtitative Analysis Navigator (B.08.00) to identify charge states and m/z ranges for further processing. CIU fingerprints were extracted and processed in CIUSuite2 using default smoothing parameters.[69]

5.3. Results & Discussion

5.3.1. Cross-Laboratory CIU of Bovine Serum Albumin

Bovine serum albumin (BSA) has been used previously as a standard protein due to its unique CIU pathway revealing unfolded features corresponding to unfolding of specific subdomains of BSA.[182] **Figure 5.1(A)** contains CIU fingerprints from University of Michigan (UM), Texas A&M University (TAMU), and Vanderbilt University (VU) for BSA 16+ ions. Each laboratory was able to achieve triplicate RMSDs of less than 3%, showing excellent reproducibility of the CIU fingerprints. In addition, each laboratory was able to observe five features (labeled F1 through F5) in each CIU fingerprint including the native-like starting conformer (F1) of ~3400 Å^2. The CCS of the identified features from each laboratory are shown in **Figure 5.1(B)** with changes in CCS between features (as ΔCCS) shown in **Figure 5.1(C)**. Comparisons of the CCS of these identified features

shows good agreement across the different laboratories with TAMU CCS values for BSA slightly smaller across all identified features compared to UM and VU.

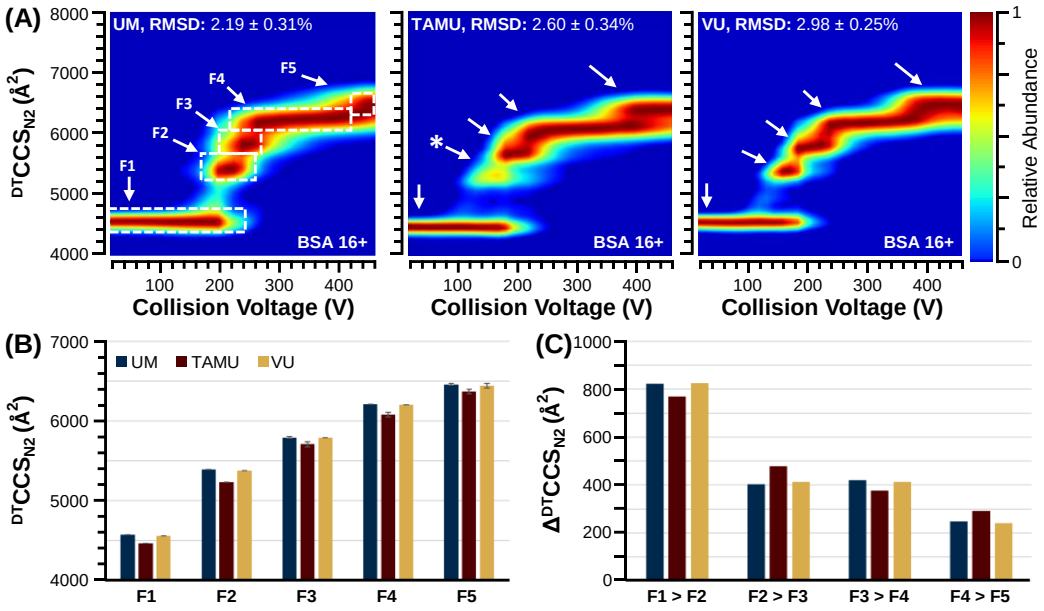

Figure 5.1. (A) CIU fingerprints for BSA 16+ ions were acquired on separate DTIM-MS instruments located at University of Michigan (UM), Texas A&M University (TAMU), and Vanderbilt University (VU). RMSDs from triplicate CIU experiments are included in each CIU heatmap. Five unfolding features (F1 through F5) are observed in each CIU fingerprint. The second feature in the TAMU fingerprint was lower in relative abundance and was identified using a modified feature fitting strategy. (B) CCS of each identified feature are compared between the different instruments. (C) ΔCCS of adjacent features were calculated and shown for each laboratory.

It is interesting to note that while the CIU feature CCS for BSA features are in good agreement, the observed activation thresholds are slightly different. For example, the UM CIU fingerprint shows an unfolding transition of F1 to F2 at a higher collision voltage (~180 V) than is observed in the TAMU and VU heatmaps (~140 V). This may be a result of less efficient collisional activation for BSA at UM at these collision potentials compared to TAMU or VU. These results are consistent and particularly apparent with the

final unfolded feature (F5) observed near the end of the CIU experiment for UM (~440 V), whereas TAMU and VU observe the F5 feature at ~370 V. Ideally, both the CIU feature CCS values and the CIU potentials at which unfolding transitions occur would be consistent across instruments. While the former has been largely achieved for BSA, the latter is an active area of research and development for commercialization of the CIU hardware upgrades.

5.3.2. Cross-Laboratory CIU of Proteins and Protein Complexes

Figure 5.2 contains CIU fingerprints from UM, TAMU, and VU for the three lowest MW proteins studied herein: ubiquitin (Ubq^{6+}, panel (A)), myoglobin (Myo^{8+}, panel (B)), and streptavidin tetramer (SA^{11+}, panel (C)). These CIU fingerprints show good reproducibility within each lab with an average RMSD across all laboratories and proteins of 2.8±0.4%. Qualitatively, these CIU fingerprints show similar features across the different laboratories with good agreements between ground-state and unfolded conformer CCS. Intermediate feature populations show much greater variability between different instruments. For example, Ubq^{6+} exhibits differing stabilities of the intermediate F2 (~1400 Å²) and F3 (~1700 Å²) conformers relative to the fully unfolded feature, F4 (~1800 Å²). Myo^{8+} shows excellent reproducibility of its unfolded feature (F3, ~2700 Å²); however, features F1 (~2000 Å²) and F2 (~2100 Å²) appear with different relative abundances across the different laboratories. SA^{11+} shows excellent agreement of the ground-state and unfolded features (F1 and F3, respectively); however, a collapsed intermediate conformer (F2, ~3500 Å²) is observed across the widest CIU voltage range

in the UM heatmap and the shortest voltage range for TAMU. For SA^{11+}, there is also a CIU intermediate of ~4000 Å^2 with very low relative abundances.

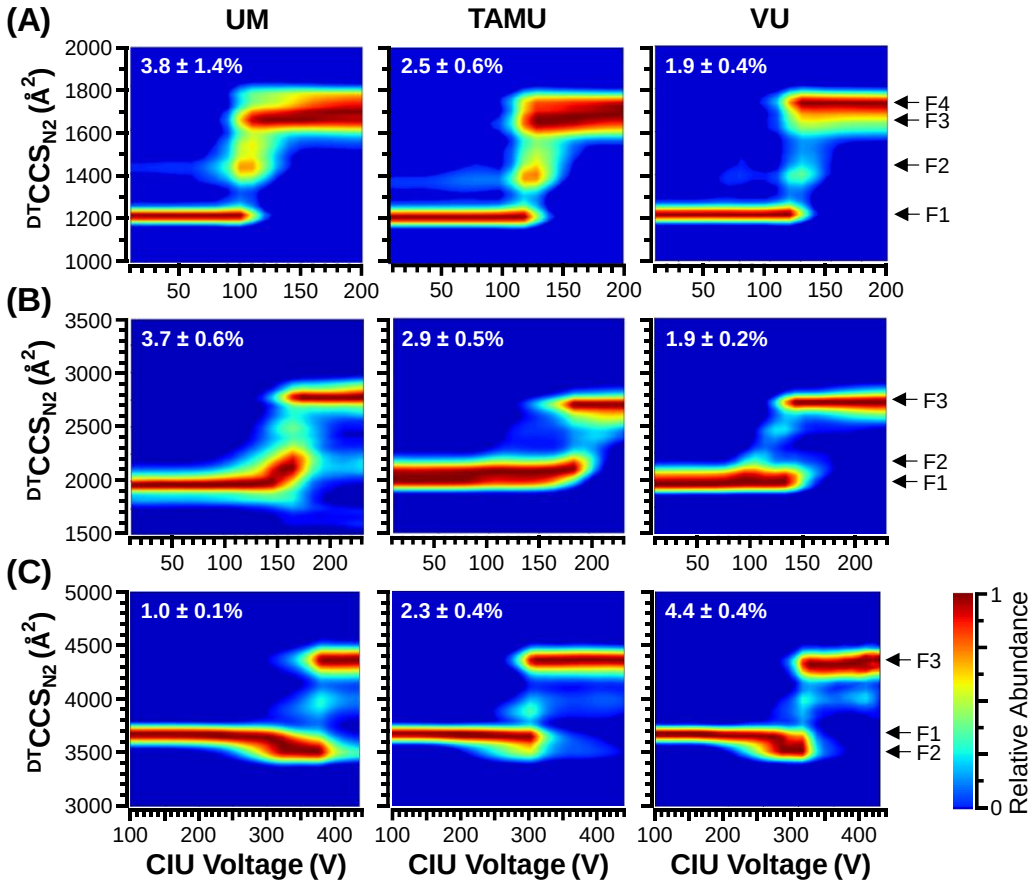

Figure 5.2. Average CIU fingerprints for (A) Ubq^{6+} (B) Myo^{8+}, and (C) SA^{11+} from triplicate measurements are shown for UM, TAMU, and VU. RMSDs from triplicate measurements are shown in the upper left corner of each CIU fingerprint. Identified CIU features are indicated by arrows at the right of the CIU fingerprint grid.

5.3.3. Cross-Laboratory CIU of Antibodies

Figure 5.3 contains CIU fingerprints for the IgG1 antibody standard from each laboratory. These fingerprints have slightly higher triplicate RMSDs compared to the fingerprints contained in **Figure 5.1** and **Figure 5.2**. These fingerprints also contain

significantly different observed features both in terms of the numbers of features and the CCS of these features. The starting, ground-state CCS of these IgG1 ions range from ~7600 Å² (for VU, panel (C)) to ~8200 Å² (for TAMU, panel (B)) with noticeably differing CCS peak widths as well. These heterogeneous ground-state conformers then unfold through differing numbers of intermediate features prior to transitioning to a ~11000 Å² feature in each laboratory. As shown in panels (A) and (C), UM and VU laboratories were able to observe discrete, partially unfolded intermediate features, whereas TAMU observes a smearing of intermediate features from the ground-state conformers until the end of the experiment (~450 V). This discrepancy in the overall shape of the TAMU fingerprint may result from unfolding of a more unfolded and less stable ground state conformer with a larger starting CCS whereby CIU from this state may not produce stable unfolding intermediates.

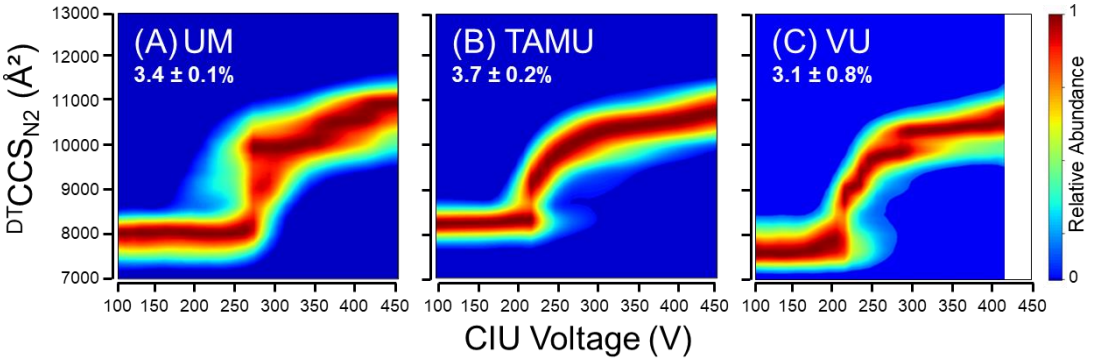

Figure 5.3. CIU fingerprints for IgG1^{26+} ions from (A) UM, (B) TAMU, and (C) VU are shown with RMSDs from triplicate measurements.

Previous work on CIU of IgG1 and other monoclonal antibody ions via static nanoESI has shown discrete unfolding transitions.[180, 183] The results presented herein used microflow direct infusion with elevated source gas temperatures (140°C) and gas flow

rates (5 L/min) to facilitate desolvation and ion transmission. For static nanoESI experiments, these elevated temperatures and gas flow rates are often unnecessary to achieve similar sensitivities. We postulate that differences in ground-state CCS distributions (and unfolding intermediate feature CCS) may result from differences in collisional activation and ion heating prior to the controlled CIU experiments performed in the high-pressure funnel region. Further development of optimized source conditions, especially for larger ions (>100 kDa) is ongoing.

5.3.4. Cross-Laboratory CIU Feature Comparisons

The CCS values of all significant features from each protein from each laboratory are summarized in **Figure 5.4** and **Table 5.1**. Overall, the CCS of every feature is in good agreement across the different laboratories as well as compared to an earlier generation CIU prototype at VU (notated VUp). The feature CCS values also agree reasonably well with previously published values as indicated with the red arrows in **Figure 5.4(A)**. These literature DTIMS values are summarized in **Table 5.1** and are in good agreement (>2% bias) for all features except SA F1 (2.1% bias) and Ubq F3 (6.5% bias).[120, 179, 184, 185] Comparison of feature CCS across all laboratories results excellent reproducibility with cross-laboratory RSDs of less than 1% for a majority of the features (13/20) as shown in **Figure 5.4(B)**. Two additional features (BSA F1, 1.2% and BSA F4, 1.1%) are also very close to this arbitrary 1% RSD threshold. The remaining features show much lower cross-laboratory reproducibility, especially the Ubq F2 and Myo F2 features and the IgG1 features discussed previously. Overall, for small and medium sized proteins and protein complexes (<100 kDa), we find good cross-laboratory agreement of CCS of CIU features.

For the IgG1 standard CIU fingerprints, the observed cross-laboratory differences largely stem from differences in ground-state ion conformer population distributions. Mitigation of these deleterious effects is under further investigation as well as isolating the cause of the observed differences to minute changes in ionization, desolvation source effects, or final sample preparation differences between each laboratory.

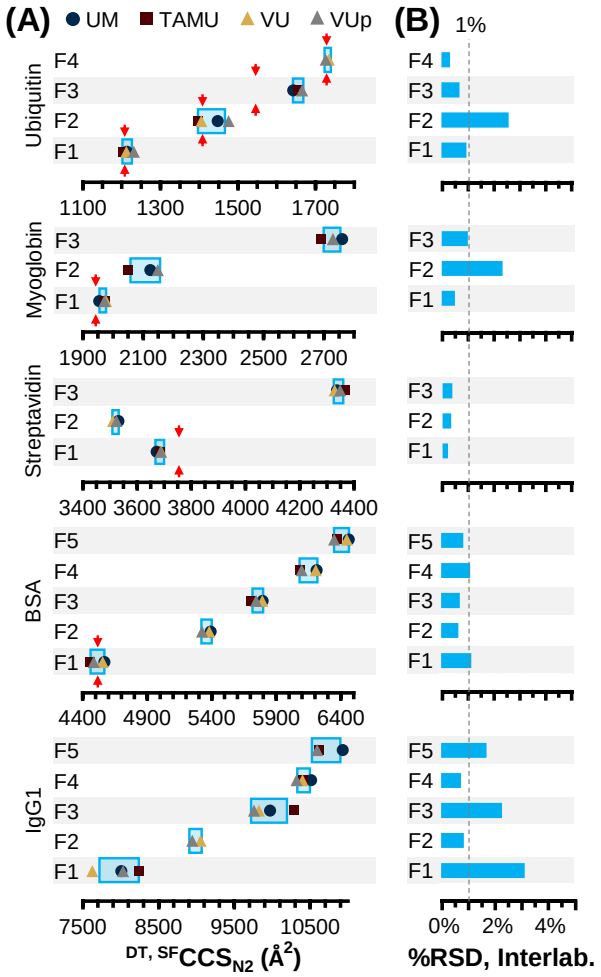

Figure 5.4. (A) CCS of significant CIU features (F1, F2, etc.) are shown for each laboratory with the addition of a lower-energy prototype collected at VU (notated as VUp). The feature CCS average and standard deviations are indicated by the light blue boxes. Red arrows indicate previous literature DTIM-MS CCS values as shown in **Table 5.1**. (B) Interlaboratory relative standard deviations (%RSD) are shown for the identified features with a majority being at or less than ~1%.

Table 5.1. Previously reported DTIM-MS CCS values are summarized with respect to the cross-laboratory CCS values for identified features.

		$^{DT}CCS_{N2}$ values reported for each protein (A^2) [a.]						
		2018 May et al.	*2020 Stiving et al.*[b.]	*2020 Zheng et al.*	*2020 Gadkari et al.*[c.]	*Lit. Avg.*	*This work* [d.]	*% Bias* [e.]
Ubiquitin (+6)	F1	1222±14 (3)	--	1214±9 (3)	1191±5 (3)	1209 (3)	1215±12 (4), 0.9%	*0.5%*
	F2	1474±18 (4)	--	--	1345±9 (3)	1410 (2)	1432±37 (4), 2.6%	*1.5%*
	F3	1628±13 (5)	--	--	1466±13 (3)	1547 (2)	1655±12 (3), 0.7%	*6.5%*
	F4	--	1730±14 (3)	--	--	1730 (1)	1731±6 (2), 0.3%	*0.0%*
Myoglobin (+8)	F1	1937±30 (5)	--	--	--	1937 (1)	1969±10 (4), 0.5%	1.6%
	F2	--	--	--	--	--	2108±50 (3), 2.4%	--
	F3	--	--	--	--	--	2728±28 (4), 1.0%	--
Streptavidin (+11)	F1	--	3760±41 (3)	--	--	3760 (1)	3683±8 (4), 0.2%	2.1%
	F2	--	--	--	--	--	3518±12 (3), 0.3%	--
	F3	--	--	--	--	--	4345±17 (4), 0.4%	--
BSA (+16)	F1	--	4510±36 (3)	--	4526±19 (3)	4518 (2)	4517±53 (4), 1.2%	0.0%
	F2	--	--	--	--	--	5364±36 (3), 0.7%	--
	F3	--	--	--	--	--	5759±42 (4), 0.7%	--
	F4	--	--	--	--	--	6149±69 (4), 1.1%	--
	F5	--	--	--	--	--	6406±55 (4), 0.9%	--
IgG1 (+26)	F1	--	--	--	--	--	7976±258 (4), 3.2%	--
	F2	--	--	--	--	--	8997±79 (2), 0.9%	--
	F3	--	--	--	--	--	9959±235 (4), 2.4%	--
	F4	--	--	--	--	--	10409±80 (4), 0.8%	--
	F5	--	--	--	--	--	1071±188 (3), 1.8%	--

a. Number of measurements are indicated in the parenthesis. Percent RSDs, when reported, are converted to standard deviations in $Å^2$.
b. The CCS values reported for ammonium acetate solution are used for ubiquitin, and BSA, and the value measured in TEAA solution is used for streptavidin. For ubiquitin, only one CCS value is reported for the +6 charge state and it is assumed this is the fully-extended conformer. The streptavidin +11 and BSA +16 values are assumed to be the lowest-energy states. CCS measurements were obtained with nano-ESI.
c. The CCS values for ubiquitin are assumed to correspond to F1, F2, and F3 in this study. CCS measurements were obtained with nano-ESI.
d. The interlaboratory relative standard deviations are also provided at the end of each entry. In some cases, not all features were observed across all laboratories/hardware configurations.
e. The percent bias is referenced against the CCS values obtained in this study.

5.4. Conclusion

For small proteins and protein complexes (<100 kDa), the upgraded CIU hardware on the Agilent 6560 shows good cross-laboratory reproducibility. For Ubq, Myo, SA, and BSA, a strong majority (13/15) of the significant CIU features had excellent cross-laboratory CCS RSDs around or below 1%. The greatest cross-laboratory variability was found for the second CIU features for Ubq and Myo, and both of these intermediate features were only stable across a narrow range of collision voltages. Overall, the

identified features for these smaller proteins and protein complexes show good cross-laboratory reproducibility in their respective CCS; however, the transition collision voltages are not reproducible between laboratories likely due to slightly different pressures and temperatures in the capillary exit region where CIU is occurring. This may require additional calibration strategies to normalize the applied collision voltage to the CID voltages required to fragment TuneMix calibrant ions.

Of greater concern is the cross-laboratory reproducibility of CIU of IgG1 ions. The CIU fingerprints from each laboratory show significantly different features. This may be explained by the differences in ground-state conformer or CCS distributions leading to CIU of different ground-state conformers that only show cross-laboratory agreement of the fully unfolded conformer at ~11,000 Å^2. Others have claimed that monoclonal antibodies, like the IgG1 standard used herein, undergo significant structural collapse of the antigen binding fragment domains during desolvation.[186] Disrupting this rearrangement process may then lead to different starting conformers for the CIU fingerprints observed herein.

It is unclear if the interlaboratory variability between CIU fingerprints is related to ion heating in the source or differences in gas-flow dynamics (*i.e.* gas expansion, gas viscosity) in the CIU lens. Optimization of source desolvation conditions (*e.g.* drying gas flow rate and temperature) may be protein-specific and may affect ground-state CCS distributions. Additionally, in this instrument, CIU is performed in a region of supersonic expansion as the exit plume of the ion transfer capillary expands into the high-pressure funnel (at ~4.8 Torr). Minor fluctuations in the pressure or temperature in this region are

likely to affect collision dynamics and may impact cross-laboratory reproducibility of CIU results. Resolving these differences through optimization of acquisition methods and refinement of the desolvation assembly hardware is an ongoing area of interest.

6. CONCLUSIONS AND FUTURE DIRECTIONS

6.1. Conclusions

Methods of nIM-MS were successfully employed to study labile reaction products of CDSA reactions in Chapter 2. By reducing the internal energy of the reaction product ions in the gas phase, intact reaction products revealed rigid topologies with no observable conformational heterogeneity. In Chapter 3, nMS of large proteins and protein complexes produced well-resolved features of low relative abundant signals for further interrogation. Truncated PK tetramer ions were interrogated, and small, covalent β-ME adducts were observed on the trimeric membrane protein complex AmtB. The native 14-mer of the protein chaperonin GroEL was also characterized as well as its CID products with resolvable signals up to 22,000 *m/z* for the charge-stripped 13-mer CID product on an extended mass range Q-TOF MS instrument. In Chapter 4, IgG1κ ions from human plasma were characterized by high-resolution MS from native-like buffer conditions. The high mass resolution revealed signals for a 40 Da mass shift on each observed glycan signal. These 40 Da mass shifts were investigated further using deglycosylation and antibody reduction techniques. Finally in Chapter 5, new desolvation assembly hardware was evaluated for CIU of proteins and protein complexes on a commercial DTIM-MS instrument in a cross-laboratory study. While the more traditional protein standards (e.g. Ubq, Myo, BSA, SA) demonstrated great interlaboratory reproducibility in CCS distributions of ground-state, intermediate, and unfolded conformer distributions, the mAb standard (e.g. universal IgG1 standard) from the different laboratories produced

significantly different CIU fingerprints, both in terms of ground-state CCS distributions as well as the number and CCS of observed intermediate features. The only common IgG1 feature among the three laboratories was the most unfolded conformer with a CCS of ~11,000 Å^2. Overall, it has been shown that nMS and nIM-MS methods are invaluable for the characterization and interrogation of ions ranging from small CDSA reaction products to monoclonal antibodies to protein folding chaperones.

6.2. Future Directions

6.2.1. IgG1κ Proteomic and Glycomic Identifications

The specific identity of the 40 Da mass shift on the *N*-glycan mass peaks IgG1κ from human myeloma plasma discussed in Chapter 4 is still not known. Future work will include further probing primary sequence for point mutations using top-down proteomics (TDP) methods with electron-capture dissociation (ECD) to obtain sequence coverage of interior amino acid residues. More traditional CID top-down sequence coverage is often limited to N- and C-terminal residues. If sequences of the IgG1 heavy and/or light chains can be identified with neighboring signals differing by 40 Da, it may help to localize the mass shifts to a section of the primary sequence. Future work will also include characterization of deglycosylase digests by LC-MS/MS to identify the structure of enzymatically released glycans. Finally, the structures of the IgG1 mAbs from myeloma plasma containing the kappa or lambda light chain must be determined and correlated with the myeloma plasma disease state from which they were purified. Understanding the

structure-function relationship between these mAbs and myeloma may prove informative for future biotherapeutic approaches.

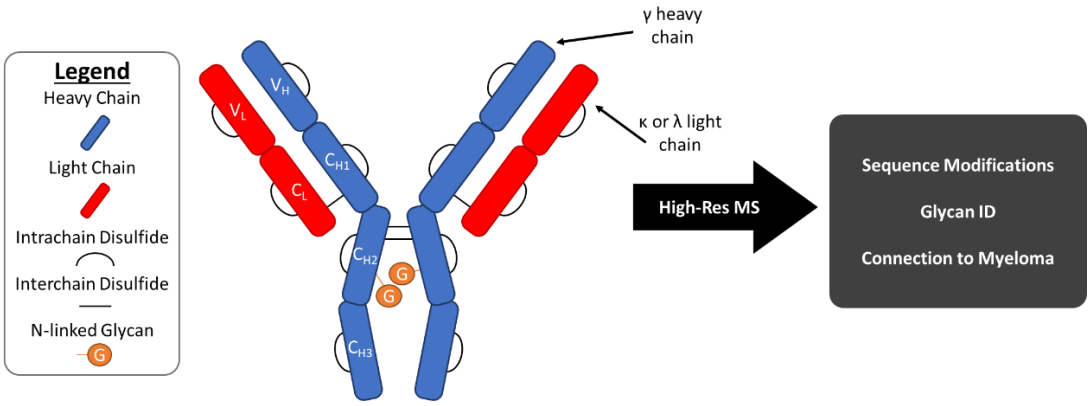

Figure 6.1. The cartoon IgG1 structure from Figure 4.1 was modified to focus on the future directions of identifying potential sequence modifications, elucidating N-glycan structures, and connecting these properties from the IgG1κ and IgG1λ to mechanisms of myeloma from which they were purified.

6.2.2. Variable-Temperature ESI of mAbs

The relationship between solution temperature and protein conformer and structural preferences in solution has been studied for decades using solution-averaged, condensed-phase assays like differential scanning calorimetry and variable-temperature circular dichroism and nuclear magnetic resonance spectroscopy. While the denaturing effects of high solution temperatures on protein structure are well-understood, the effects of subambient temperatures are less understood. Recently, we have developed a stacked Peltier chip device (shown in **Figure 6.2(B)**) amenable to variable temperature, static nESI mass spectrometry (vT-nESI-MS) experiments where the solution temperature can be varied from ~5°C to ~95°C. The degradation or decomposition of the SiLuLite IgG1 universal antibody (cartoon structure shown in **Figure 6.2(A)**) has been studied previously

by high-temperature vT-nESI-MS; however, the reversibility of conformational destabilization following repeat heating and cooling has not been studied until now. **Figure 6.2(C)** features Preliminary results from vT-nESI coupled to high-resolution MS shows distinct patterns of increased average charge below ambient temperatures owing the partial denaturation and increased SASA at low temperature. Future directions will include surveying effect of vT-nESI on other mAbs as well as transferring this technology to the Agilent ESI sources for vT-nESI-DTIM-MS on the Agilent 6560 using the source design shown in **Figure 6.2(D)**.

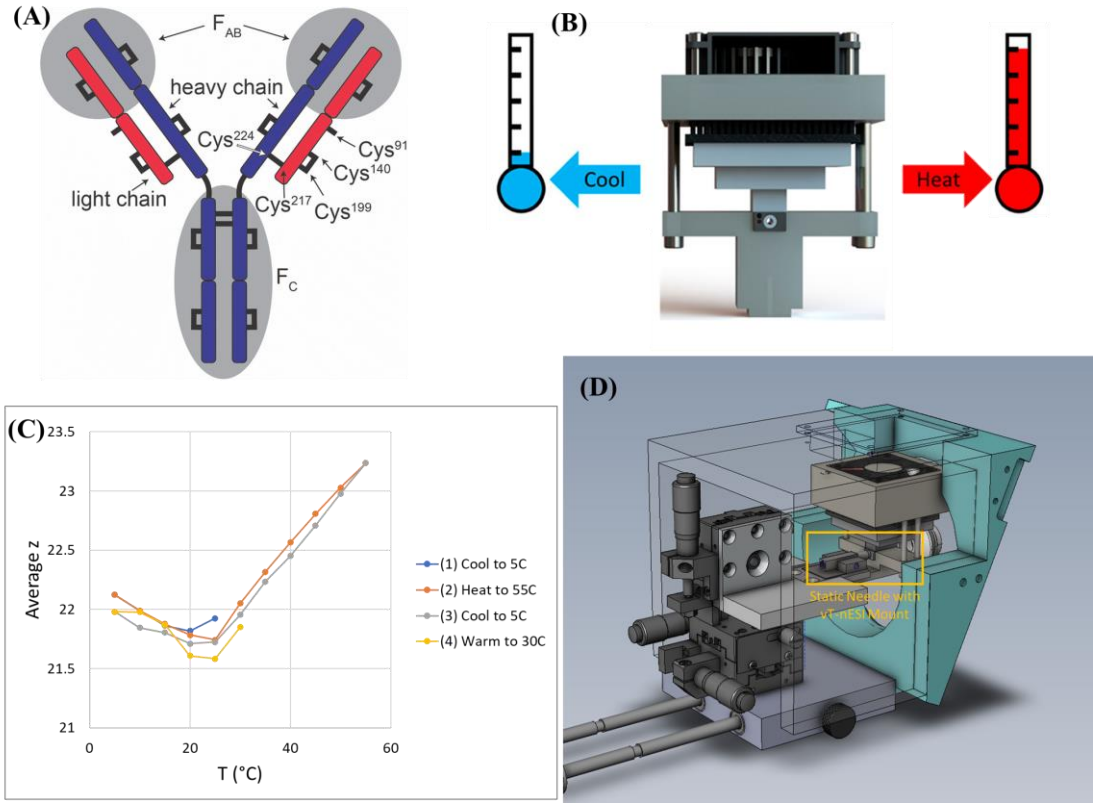

Figure 6.2. (A) The cartoon structure of the Sigma SiLuLite universal antibody standards shows the respective heavy (blue) and light (red) chains as well as the F_{ab} and F_c domains and available Cys residues for disulfide scrambling. **(B)** The three-tiered Peltier chip stack assists in the heating and cooling of the static nESI emitters for vT-nESI-MS experiments. **(C)** The resulting correlation of average charge of the most abundant IgG1 glycoform with

temperature shows effects of reversible cold and heat denaturation. **(D)** The modular prototype design for vT-nESI source will provide opportunities to characterize the effects of temperature on protein structure using the Agilent 6560 DTIMS-Q-TOF and/or Agilent 6545XT Q-TOF. Panel (A) reprinted with permission from Brown, C.J.; Woodall, D.W.; El-Baba, T.J.; Clemmer, D.E. *Journal of the American Society for Mass Spectrometry*, **2019**, *30*, 2438-2445. Copyright 2019 American Chemical Society. Panel (B) reprinted with permission from McCabe, J.W.; Shirzadeh, M.; Walker, T.E.; Lin, C.-W.; Jones, B.J.; Wysocki, V.H.; Barondeau, D.P.; Clemmer, D.E.; Laganowsky, A.; Russell, D.H. *Analytical Chemistry*, **2021**, *93*, 6924-6931. Copyright 2012 American Chemical Society.

REFERENCES

1. Wu, C.; Siems, W. F.; Klasmeier, J.; Hill, H. H., Separation of Isomeric Peptides Using Electrospray Ionization/High-Resolution Ion Mobility Spectrometry. *Analytical Chemistry* **2000,** *72* (2), 391-395.
2. Ruotolo, B. T.; Verbeck; Thomson, L. M.; Woods, A. S.; Gillig, K. J.; Russell, D. H., Distinguishing between Phosphorylated and Nonphosphorylated Peptides with Ion Mobility−Mass Spectrometry. *Journal of Proteome Research* **2002,** *1* (4), 303-306.
3. Bush, M. F.; Campuzano, I. D. G.; Robinson, C. V., Ion Mobility Mass Spectrometry of Peptide Ions: Effects of Drift Gas and Calibration Strategies. *Analytical Chemistry* **2012,** *84* (16), 7124-7130.
4. Ohshimo, K.; Takahashi, T.; Moriyama, R.; Misaizu, F., Compact Non-Rock-Salt Structures in Sodium Fluoride Cluster Ions at Specific Sizes Revealed by Ion Mobility Mass Spectrometry. *The Journal of Physical Chemistry A* **2014,** *118* (43), 9970-9975.
5. Ouyang, H.; Larriba-Andaluz, C.; Oberreit, D. R.; Hogan, C. J., The Collision Cross Sections of Iodide Salt Cluster Ions in Air via Differential Mobility Analysis-Mass Spectrometry. *J Am Soc Mass Spectr* **2013,** *24* (12), 1833-1847.
6. Abbas, Y. M.; Wu, D.; Bueler, S. A.; Robinson, C. V.; Rubinstein, J. L., Structure of V-ATPase from the mammalian brain. *Science* **2020,** *367* (6483), 1240-1246.
7. McLaughlin, S. H.; Sobott, F.; Yao, Z.-P.; Zhang, W.; Nielsen, P. R.; Grossmann, J. G.; Laue, E. D.; Robinson, C. V.; Jackson, S. E., The Co-chaperone p23 Arrests the Hsp90 ATPase Cycle to Trap Client Proteins. *J. Mol. Biol.* **2006,** *356* (3), 746-758.
8. Lin, C.-W.; McCabe, J. W.; Russell, D. H.; Barondeau, D. P., Molecular Mechanism of ISC Iron–Sulfur Cluster Biogenesis Revealed by High-Resolution Native Mass Spectrometry. *Journal of the American Chemical Society* **2020,** *142* (13), 6018-6029.
9. Fuerstenau, S. D.; Benner, W. H.; Thomas, J. J.; Brugidou, C.; Bothner, B.; Siuzdak, G., Mass Spectrometry of an Intact Virus. *Angewandte Chemie International Edition* **2001,** *40* (3), 541-544.
10. Uetrecht, C.; Watts, N. R.; Stahl, S. J.; Wingfield, P. T.; Steven, A. C.; Heck, A. J. R., Subunit exchange rates in Hepatitis B virus capsids are geometry- and temperature-dependent. *Physical Chemistry Chemical Physics* **2010,** *12* (41), 13368.
11. Wörner, T. P.; Snijder, J.; Bennett, A.; Agbandje-Mckenna, M.; Makarov, A. A.; Heck, A. J. R., Resolving heterogeneous macromolecular assemblies by Orbitrap-based single-particle charge detection mass spectrometry. *Nature Methods* **2020,** *17* (4), 395-398.
12. Poltash, M. L.; McCabe, J. W.; Shirzadeh, M.; Laganowsky, A.; Russell, D. H., Native IM-Orbitrap MS: Resolving What Was Hidden. *Trends Analyt Chem* **2020,** *124*.

13. McCabe, J. W.; Hebert, M. J.; Shirzadeh, M.; Mallis, C. S.; Denton, J. K.; Walker, T. E.; Russell, D. H., The Ims Paradox: A Perspective on Structural Ion Mobility-Mass Spectrometry. *Mass Spectrom Rev* **2021,** *40* (3), 280-305.
14. Mallis, C. S.; Saha, M. L.; Stang, P. J.; Russell, D. H., Topological Characterization of Coordination-Driven Self-assembly Complexes: Applications of Ion Mobility-Mass Spectrometry. *J Am Soc Mass Spectr* **2019,** *30* (9), 1654-1662.
15. Mallis, C. S.; Zheng, X.; Qiu, X.; McCabe, J. W.; Shirzadeh, M.; Lyu, J.; Laganowsky, A.; Russell, D. H., Development of Native MS Capabilities on an Extended Mass Range Q-TOF MS. *Int J Mass Spectrom* **2020,** *458*, 116451.
16. Leney, A. C.; Heck, A. J., Native Mass Spectrometry: What is in the Name? *J Am Soc Mass Spectrom* **2017,** *28* (1), 5-13.
17. Dill, K. A.; Chan, H. S., From Levinthal to pathways to funnels. *Nat Struct Biol* **1997,** *4* (1), 10-9.
18. Dill, K. A.; MacCallum, J. L., The protein-folding problem, 50 years on. *Science* **2012,** *338* (6110), 1042-6.
19. Vanaernum, Z. L.; Busch, F.; Jones, B. J.; Jia, M.; Chen, Z.; Boyken, S. E.; Sahasrabuddhe, A.; Baker, D.; Wysocki, V. H., Rapid online buffer exchange for screening of proteins, protein complexes and cell lysates by native mass spectrometry. *Nature Protocols* **2020,** *15* (3), 1132-1157.
20. Benesch, J. L., Collisional activation of protein complexes: picking up the pieces. *J Am Soc Mass Spectrom* **2009,** *20* (3), 341-8.
21. Gabelica, V.; Livet, S.; Rosu, F., Optimizing Native Ion Mobility Q-TOF in Helium and Nitrogen for Very Fragile Noncovalent Structures. *J Am Soc Mass Spectrom* **2018,** *29* (11), 2189-2198.
22. Eldrid, C.; Ujma, J.; Kalfas, S.; Tomczyk, N.; Giles, K.; Morris, M.; Thalassinos, K., Gas Phase Stability of Protein Ions in a Cyclic Ion Mobility Spectrometry Traveling Wave Device. *Analytical Chemistry* **2019,** *91* (12), 7554-7561.
23. Shu-Hua Chen, D. H. R., How Closely Related Are Conformations of Protein Ions
Sampled by IM-MS to Native Solution Structures? *J Am Soc Mass Spectrom* **2015,** *26*, 1433-1443.
24. Schachner, L. F.; Ives, A. N.; McGee, J. P.; Melani, R. D.; Kafader, J. O.; Compton, P. D.; Patrie, S. M.; Kelleher, N. L., Standard Proteoforms and Their Complexes for Native Mass Spectrometry. *J Am Soc Mass Spectrom* **2019,** *30* (7), 1190-1198.
25. Heck, A. J., Native mass spectrometry: a bridge between interactomics and structural biology. *Nat Methods* **2008,** *5* (11), 927-33.
26. Chen, S. H.; Russell, D. H., How Closely Related Are Conformations of Protein Ions Sampled by IM-MS to Native Solution Structures? *J Am Soc Mass Spectrom* **2015,** *26* (9), 1433-43.
27. Harrison, J. A.; Kelso, C.; Pukala, T. L.; Beck, J. L., Conditions for Analysis of Native Protein Structures Using Uniform Field Drift Tube Ion Mobility Mass Spectrometry and Characterization of Stable Calibrants for TWIM-MS. *J Am Soc Mass Spectrom* **2019,** *30* (2), 256-267.

28. Calabrese, V.; Lavanant, H.; Rosu, F.; Gabelica, V.; Afonso, C., Collision Cross Sections of Phosphoric Acid Cluster Anions in Helium Measured by Drift Tube Ion Mobility Mass Spectrometry. *J Am Soc Mass Spectr* **2020,** *31* (4), 969-981.
29. Taylor, G., Disintegration of water drops in an electric field. *Proceedings of the Royal Society of London. Series A. Mathematical and Physical Sciences* **1964,** *280* (1382), 383-397.
30. Rayleigh, L., XX. On the equilibrium of liquid conducting masses charged with electricity. *The London, Edinburgh, and Dublin Philosophical Magazine and Journal of Science* **1882,** *14* (87), 184-186.
31. Banerjee, S.; Mazumdar, S., Electrospray ionization mass spectrometry: a technique to access the information beyond the molecular weight of the analyte. *Int J Anal Chem* **2012,** *2012*, 282574.
32. Lee, S.-W.; Freivogel, P.; Schindler, T.; Beauchamp, J. L., Freeze-Dried Biomolecules: FT-ICR Studies of the Specific Solvation of Functional Groups and Clathrate Formation Observed by the Slow Evaporation of Water from Hydrated Peptides and Model Compounds in the Gas Phase. *Journal of the American Chemical Society* **1998,** *120* (45), 11758-11765.
33. Loo, R. R. O.; Loo, J. A., Salt Bridge Rearrangement (SaBRe) Explains the Dissociation Behavior of Noncovalent Complexes. *J Am Soc Mass Spectr* **2016,** *27* (6), 975-990.
34. Chingin, K.; Barylyuk, K., Charge-State-Dependent Variation of Signal Intensity Ratio between Unbound Protein and Protein–Ligand Complex in Electrospray Ionization Mass Spectrometry: The Role of Solvent-Accessible Surface Area. *Analytical Chemistry* **2018,** *90* (9), 5521-5528.
35. Poltash, M. L.; Shirzadeh, M.; McCabe, J. W.; Moghadamchargari, Z.; Laganowsky, A.; Russell, D. H., New insights into the metal-induced oxidative degradation pathways of transthyretin. *Chem Commun (Camb)* **2019,** *55* (28), 4091-4094.
36. Susa, A. C.; Xia, Z.; Williams, E. R., Small Emitter Tips for Native Mass Spectrometry of Proteins and Protein Complexes from Nonvolatile Buffers That Mimic the Intracellular Environment. *Analytical Chemistry* **2017,** *89* (5), 3116-3122.
37. Lanucara, F.; Holman, S. W.; Gray, C. J.; Eyers, C. E., The power of ion mobility-mass spectrometry for structural characterization and the study of conformational dynamics. *Nat Chem* **2014,** *6* (4), 281-94.
38. Revercomb, H. E.; Mason, E. A., Theory of plasma chromatography/gaseous electrophoresis. Review. *Analytical Chemistry* **1975,** *47* (7), 970-983.
39. Ruotolo, B. T.; Benesch, J. L.; Sandercock, A. M.; Hyung, S. J.; Robinson, C. V., Ion mobility-mass spectrometry analysis of large protein complexes. *Nat. Protoc.* **2008,** *3* (7), 1139-52.
40. Duez, Q.; Chirot, F.; Lienard, R.; Josse, T.; Choi, C.; Coulembier, O.; Dugourd, P.; Cornil, J.; Gerbaux, P.; De Winter, J., Polymers for Traveling Wave Ion Mobility Spectrometry Calibration. *J Am Soc Mass Spectrom* **2017,** *28* (11), 2483-2491.

41. Hines, K. M.; May, J. C.; McLean, J. A.; Xu, L., Evaluation of Collision Cross Section Calibrants for Structural Analysis of Lipids by Traveling Wave Ion Mobility-Mass Spectrometry. *Anal Chem* **2016,** *88* (14), 7329-36.
42. Hernandez, D. R.; Debord, J. D.; Ridgeway, M. E.; Kaplan, D. A.; Park, M. A.; Fernandez-Lima, F., Ion dynamics in a trapped ion mobility spectrometer. *The Analyst* **2014,** *139* (8), 1913-1921.
43. Silveira, J. A.; Ridgeway, M. E.; Park, M. A., High Resolution Trapped Ion Mobility Spectrometery of Peptides. *Analytical Chemistry* **2014,** *86* (12), 5624-5627.
44. Berman, H. M., The Protein Data Bank. *Nucleic Acids Research* **2000,** *28* (1), 235-242.
45. Rolland, A. D.; Prell, J. S., Computational insights into compaction of gas-phase protein and protein complex ions in native ion mobility-mass spectrometry. *TrAC Trends in Analytical Chemistry* **2019**.
46. Wyttenbach, T.; Helden, G. v.; Batka, J. J.; Carlat, D.; Bowers, M. T., Effect of the long-range potential on ion mobility measurements. *J. Am. Soc. Mass Spectrom.* **1997,** *8* (3), 275-82.
47. Mesleh, M. F.; Hunter, J. M.; Shvartsburg, A. A.; Schatz, G. C.; Jarrold, M. F., Structural Information from Ion Mobility Measurements: Effects of the Long-Range Potential. *J. Phys. Chem.* **1996,** *100* (40), 16082-6.
48. Shvartsburg, A. A.; Jarrold, M. F., An exact hard-spheres scattering model for the mobilities of polyatomic ions. *Chemical Physics Letters* **1996,** *261* (1-2), 86-91.
49. Bleiholder, C.; Wyttenbach, T.; Bowers, M. T., A novel projection approximation algorithm for the fast and accurate computation of molecular collision cross sections (I). Method. *Int. J. Mass Spectrom.* **2011,** *308* (1), 1-10.
50. Anderson, S. E.; Bleiholder, C.; Brocker, E. R.; Stang, P. J.; Bowers, M. T., A novel projection approximation algorithm for the fast and accurate computation of molecular collision cross sections (III): Application to supramolecular coordination-driven assemblies with complex shapes. *Int. J. Mass Spectrom.* **2012,** *330* (Supplement C), 78-84.
51. Bleiholder, C.; Contreras, S.; Bowers, M. T., A novel projection approximation algorithm for the fast and accurate computation of molecular collision cross sections (IV). Application to polypeptides. *Int J Mass Spectrom* **2013,** *354*, 275-280.
52. Bleiholder, C.; Contreras, S.; Do, T. D.; Bowers, M. T., A novel projection approximation algorithm for the fast and accurate computation of molecular collision cross sections (II). Model parameterization and definition of empirical shape factors for proteins. *Int J Mass Spectrom* **2013,** *345*, 89-96.
53. McCabe, J. W.; Mallis, C. S.; Kocurek, K. I.; Poltash, M. L.; Shirzadeh, M.; Hebert, M. J.; Fan, L.; Walker, T. E.; Zheng, X.; Jiang, T.; Dong, S.; Lin, C. W.; Laganowsky, A.; Russell, D. H., First-Principles Collision Cross Section Measurements of Large Proteins and Protein Complexes. *Anal Chem* **2020,** *92* (16), 11155-11163.
54. Marklund, E. G.; Degiacomi, M. T.; Robinson, C. V.; Baldwin, A. J.; Benesch, J. L., Collision cross sections for structural proteomics. *Structure* **2015,** *23* (4), 791-9.

55. Ewing, S. A.; Donor, M. T.; Wilson, J. W.; Prell, J. S., Collidoscope: An Improved Tool for Computing Collisional Cross-Sections with the Trajectory Method. *J Am Soc Mass Spectrom* **2017,** *28* (4), 587-596.
56. Poltash, M. L.; McCabe, J. W.; Shirzadeh, M.; Laganowsky, A.; Clowers, B. H.; Russell, D. H., Fourier Transform-Ion Mobility-Orbitrap Mass Spectrometer: A Next-Generation Instrument for Native Mass Spectrometry. *Anal Chem* **2018,** *90* (17), 10472-10478.
57. Zinnel, N. F.; Pai, P. J.; Russell, D. H., Ion mobility-mass spectrometry (IM-MS) for top-down proteomics: increased dynamic range affords increased sequence coverage. *Anal Chem* **2012,** *84* (7), 3390-7.
58. Harvey, S. R.; Macphee, C. E.; Barran, P. E., Ion mobility mass spectrometry for peptide analysis. *Methods* **2011,** *54* (4), 454-461.
59. Kliman, M.; May, J. C.; McLean, J. A., Lipid analysis and lipidomics by structurally selective ion mobility-mass spectrometry. *Biochimica et Biophysica Acta (BBA) - Molecular and Cell Biology of Lipids* **2011,** *1811* (11), 935-945.
60. Leaptrot, K. L.; May, J. C.; Dodds, J. N.; McLean, J. A., Ion mobility conformational lipid atlas for high confidence lipidomics. *Nature Communications* **2019,** *10* (1).
61. Zheng, X.; Smith, R. D.; Baker, E. S., Recent advances in lipid separations and structural elucidation using mass spectrometry combined with ion mobility spectrometry, ion-molecule reactions and fragmentation approaches. *Current Opinion in Chemical Biology* **2018,** *42*, 111-118.
62. Laganowsky, A.; Reading, E.; Allison, T. M.; Ulmschneider, M. B.; Degiacomi, M. T.; Baldwin, A. J.; Robinson, C. V., Membrane proteins bind lipids selectively to modulate their structure and function. *Nature* **2014,** *510* (7503), 172-175.
63. Allison, T. M.; Reading, E.; Liko, I.; Baldwin, A. J.; Laganowsky, A.; Robinson, C. V., Quantifying the stabilizing effects of protein-ligand interactions in the gas phase. *Nat Commun* **2015,** *6*.
64. Liu, Y.; Cong, X.; Liu, W.; Laganowsky, A., Characterization of Membrane Protein-Lipid Interactions by Mass Spectrometry Ion Mobility Mass Spectrometry. *J Am Soc Mass Spectrom* **2017,** *28* (4), 579-586.
65. Zhou, M.; Jones, C. M.; Wysocki, V. H., Dissecting the large noncovalent protein complex GroEL with surface-induced dissociation and ion mobility-mass spectrometry. *Anal Chem* **2013,** *85* (17), 8262-7.
66. van Duijn, E.; Barendregt, A.; Synowsky, S.; Versluis, C.; Heck, A. J., Chaperonin complexes monitored by ion mobility mass spectrometry. *J Am Chem Soc* **2009,** *131* (4), 1452-9.
67. Konijnenberg, A.; Butterer, A.; Sobott, F., Native ion mobility-mass spectrometry and related methods in structural biology. *Biochimica et Biophysica Acta (BBA) - Proteins and Proteomics* **2013,** *1834* (6), 1239-1256.
68. Hopper, J. T.; Oldham, N. J., Collision induced unfolding of protein ions in the gas phase studied by ion mobility-mass spectrometry: the effect of ligand binding on conformational stability. *J Am Soc Mass Spectrom* **2009,** *20* (10), 1851-8.

69. Polasky, D. A.; Dixit, S. M.; Fantin, S. M.; Ruotolo, B. T., CIUSuite 2: Next-Generation Software for the Analysis of Gas-Phase Protein Unfolding Data. *Anal Chem* **2019,** *91* (4), 3147-3155.
70. Eschweiler, J. D.; Rabuck-Gibbons, J. N.; Tian, Y.; Ruotolo, B. T., CIUSuite: A Quantitative Analysis Package for Collision Induced Unfolding Measurements of Gas-Phase Protein Ions. *Anal Chem* **2015,** *87* (22), 11516-22.
71. Stang, P. J.; Olenyuk, B., Self-Assembly, Symmetry, and Molecular Architecture: Coordination as the Motif in the Rational Design of Supramolecular Metallacyclic Polygons and Polyhedra. *Accounts of Chemical Research* **1997,** *30* (12), 502-518.
72. Chakrabarty, R.; Mukherjee, P. S.; Stang, P. J., Supramolecular coordination: self-assembly of finite two- and three-dimensional ensembles. *Chem Rev* **2011,** *111* (11), 6810-918.
73. Giles, K.; Pringle, S. D.; Worthington, K. R.; Little, D.; Wildgoose, J. L.; Bateman, R. H., Applications of a travelling wave-based radio-frequency-only stacked ring ion guide. *Rapid Commun Mass Spectrom* **2004,** *18* (20), 2401-14.
74. Pringle, S. D.; Giles, K.; Wildgoose, J. L.; Williams, J. P.; Slade, S. E.; Thalassinos, K.; Bateman, R. H.; Bowers, M. T.; Scrivens, J. H., An investigation of the mobility separation of some peptide and protein ions using a new hybrid quadrupole/travelling wave IMS/oa-ToF instrument. *Int J Mass Spectrom* **2007,** *261* (1), 1-12.
75. Campuzano, I. D. G.; Sandoval, W., Denaturing and Native Mass Spectrometric Analytics for Biotherapeutic Drug Discovery Research: Historical, Current, and Future Personal Perspectives. *J Am Soc Mass Spectrom* **2021**.
76. Li, W.; Zhu, Z.; Chen, W.; Feng, Y.; Dimitrov, D. S., Crystallizable Fragment Glycoengineering for Therapeutic Antibodies Development. *Front Immunol* **2017,** *8* (1554), 1554.
77. Boune, S.; Hu, P.; Epstein, A. L.; Khawli, L. A., Principles of N-Linked Glycosylation Variations of IgG-Based Therapeutics: Pharmacokinetic and Functional Considerations. *Antibodies (Basel)* **2020,** *9* (2), 22.
78. Kurulugama, R. T.; Darland, E.; Kuhlmann, F.; Stafford, G.; Fjeldsted, J., Evaluation of drift gas selection in complex sample analyses using a high performance drift tube ion mobility-QTOF mass spectrometer. *The Analyst* **2015,** *140* (20), 6834-6844.
79. Whitesides, G. M.; Grzybowski, B., Self-assembly at all scales. *Science* **2002,** *295* (5564), 2418-21.
80. Northrop, B. H.; Zheng, Y. R.; Chi, K. W.; Stang, P. J., Self-organization in coordination-driven self-assembly. *Acc Chem Res* **2009,** *42* (10), 1554-63.
81. Baxter, P. N. W.; Lehn, J. M.; Baum, G.; Fenske, D., The design and generation of inorganic cylindrical cage architectures by metal-ion-directed multicomponent self-assembly. *Chem-Eur J* **1999,** *5* (1), 102-112.
82. Lehn, J. M.; Rigault, A.; Siegel, J.; Harrowfield, J.; Chevrier, B.; Moras, D., Spontaneous Assembly of Double-Stranded Helicates from Oligobipyridine Ligands and

Copper(I) Cations - Structure of an Inorganic Double Helix. *P Natl Acad Sci USA* **1987,** *84* (9), 2565-2569.
83. Kramer, R.; Lehn, J. M.; Marquis-Rigault, A., Self-Recognition in Helicate Self-Assembly - Spontaneous Formation of Helical Metal-Complexes from Mixtures of Ligands and Metal-Ions. *P Natl Acad Sci USA* **1993,** *90* (12), 5394-5398.
84. Datta, S.; Saha, M. L.; Stang, P. J., Hierarchical Assemblies of Supramolecular Coordination Complexes. *Acc Chem Res* **2018,** *51* (9), 2047-2063.
85. Zhou, Z.; Yan, X.; Cook, T. R.; Saha, M. L.; Stang, P. J., Engineering Functionalization in a Supramolecular Polymer: Hierarchical Self-Organization of Triply Orthogonal Non-covalent Interactions on a Supramolecular Coordination Complex Platform. *J Am Chem Soc* **2016,** *138* (3), 806-9.
86. Saha, M. L.; Yan, X.; Stang, P. J., Photophysical Properties of Organoplatinum(II) Compounds and Derived Self-Assembled Metallacycles and Metallacages: Fluorescence and its Applications. *Acc Chem Res* **2016,** *49* (11), 2527-2539.
87. Fujita, D.; Ueda, Y.; Sato, S.; Mizuno, N.; Kumasaka, T.; Fujita, M., Self-assembly of tetravalent Goldberg polyhedra from 144 small components. *Nature* **2016,** *540* (7634), 563-+.
88. Hoshino, M.; Khutia, A.; Xing, H.; Inokuma, Y.; Fujita, M., The crystalline sponge method updated. *IUCrJ* **2016,** *3* (Pt 2), 139-51.
89. Yoneya, M.; Tsuzuki, S.; Yamaguchi, T.; Sato, S.; Fujita, M., Coordination-directed self-assembly of M12L24 nanocage: effects of kinetic trapping on the assembly process. *ACS Nano* **2014,** *8* (2), 1290-6.
90. Chan, Y. T.; Li, X.; Soler, M.; Wang, J. L.; Wesdemiotis, C.; Newkome, G. R., Self-assembly and traveling wave ion mobility mass spectrometry analysis of hexacadmium macrocycles. *J. Am. Chem. Soc.* **2009,** *131* (45), 16395-7.
91. Chan, Y. T.; Li, X.; Yu, J.; Carri, G. A.; Moorefield, C. N.; Newkome, G. R.; Wesdemiotis, C., Design, synthesis, and traveling wave ion mobility mass spectrometry characterization of iron(II)- and ruthenium(II)-terpyridine metallomacrocycles. *J Am Chem Soc* **2011,** *133* (31), 11967-76.
92. Li, X.; Chan, Y. T.; Newkome, G. R.; Wesdemiotis, C., Gradient tandem mass spectrometry interfaced with ion mobility separation for the characterization of supramolecular architectures. *Anal Chem* **2011,** *83* (4), 1284-90.
93. Cook, T. R.; Zheng, Y. R.; Stang, P. J., Metal-organic frameworks and self-assembled supramolecular coordination complexes: comparing and contrasting the design, synthesis, and functionality of metal-organic materials. *Chem Rev* **2013,** *113* (1), 734-77.
94. Cook, T. R.; Stang, P. J., Recent Developments in the Preparation and Chemistry of Metallacycles and Metallacages via Coordination. *Chem Rev* **2015,** *115* (15), 7001-45.
95. Yam, V. W.; Au, V. K.; Leung, S. Y., Light-Emitting Self-Assembled Materials Based on d(8) and d(10) Transition Metal Complexes. *Chem Rev* **2015,** *115* (15), 7589-728.

96. Hong, C. M.; Bergman, R. G.; Raymond, K. N.; Toste, F. D., Self-Assembled Tetrahedral Hosts as Supramolecular Catalysts. *Acc Chem Res* **2018,** *51* (10), 2447-2455.
97. Zhang, D.; Ronson, T. K.; Nitschke, J. R., Functional Capsules via Subcomponent Self-Assembly. *Acc Chem Res* **2018,** *51* (10), 2423-2436.
98. Jurneczko, E.; Barran, P. E., How useful is ion mobility mass spectrometry for structural biology? The relationship between protein crystal structures and their collision cross sections in the gas phase. *Analyst* **2011,** *136* (1), 20-8.
99. Bohrer, B. C.; Merenbloom, S. I.; Koeniger, S. L.; Hilderbrand, A. E.; Clemmer, D. E., Biomolecule analysis by ion mobility spectrometry. *Annu Rev Anal Chem (Palo Alto Calif)* **2008,** *1* (1), 293-327.
100. Bleiholder, C.; Bowers, M. T., The Solution Assembly of Biological Molecules Using Ion Mobility Methods: From Amino Acids to Amyloid beta-Protein. *Annu Rev Anal Chem (Palo Alto Calif)* **2017,** *10* (1), 365-386.
101. Kind, T.; Fiehn, O., Seven Golden Rules for heuristic filtering of molecular formulas obtained by accurate mass spectrometry. *BMC Bioinformatics* **2007,** *8*, 105.
102. Shi, L.; Holliday, A. E.; Glover, M. S.; Ewing, M. A.; Russell, D. H.; Clemmer, D. E., Ion Mobility-Mass Spectrometry Reveals the Energetics of Intermediates that Guide Polyproline Folding. *J Am Soc Mass Spectrom* **2016,** *27* (1), 22-30.
103. Gaye, M. M.; Nagy, G.; Clemmer, D. E.; Pohl, N. L., Multidimensional Analysis of 16 Glucose Isomers by Ion Mobility Spectrometry. *Anal Chem* **2016,** *88* (4), 2335-44.
104. Brocker, E. R.; Anderson, S. E.; Northrop, B. H.; Stang, P. J.; Bowers, M. T., Structures of metallosupramolecular coordination assemblies can be obtained by ion mobility spectrometry-mass spectrometry. *J Am Chem Soc* **2010,** *132* (38), 13486-94.
105. Morsa, D.; Gabelica, V.; De Pauw, E., Effective temperature of ions in traveling wave ion mobility spectrometry. *Anal Chem* **2011,** *83* (14), 5775-82.
106. Harrison, J. A.; Kelso, C.; Pukala, T. L.; Beck, J. L., Conditions for Analysis of Native Protein Structures Using Uniform Field Drift Tube Ion Mobility Mass Spectrometry and Characterization of Stable Calibrants for TWIM-MS. *J Am Soc Mass Spectrom* **2018**.
107. Giles, K.; Williams, J. P.; Campuzano, I., Enhancements in travelling wave ion mobility resolution. *Rapid Commun Mass Spectrom* **2011,** *25* (11), 1559-66.
108. Haler, J. R. N.; Kune, C.; Massonnet, P.; Comby-Zerbino, C.; Jordens, J.; Honing, M.; Mengerink, Y.; Far, J.; De Pauw, E., Comprehensive Ion Mobility Calibration: Poly(ethylene oxide) Polymer Calibrants and General Strategies. *Anal Chem* **2017,** *89* (22), 12076-12086.
109. Patiny, L.; Borel, A., ChemCalc: a building block for tomorrow's chemical infrastructure. *J Chem Inf Model* **2013,** *53* (5), 1223-8.
110. Kune, C.; Far, J.; De Pauw, E., Accurate Drift Time Determination by Traveling Wave Ion Mobility Spectrometry: The Concept of the Diffusion Calibration. *Anal Chem* **2016,** *88* (23), 11639-11646.

111. Bush, M. F.; Campuzano, I. D. G.; Robinson, C. V., Ion mobility mass spectrometry of peptide ions: effects of drift gas and calibration strategies. *Anal Chem* **2012,** *84* (16), 7124-30.
112. Smith, D. P.; Knapman, T. W.; Campuzano, I.; Malham, R. W.; Berryman, J. T.; Radford, S. E.; Ashcroft, A. E., Deciphering drift time measurements from travelling wave ion mobility spectrometry-mass spectrometry studies. *Eur J Mass Spectrom (Chichester)* **2009,** *15* (2), 113-30.
113. Toby, T. K.; Fornelli, L.; Kelleher, N. L., Progress in Top-Down Proteomics and the Analysis of Proteoforms. *Annu Rev Anal Chem (Palo Alto Calif)* **2016,** *9* (1), 499-519.
114. Gillet, L. C.; Leitner, A.; Aebersold, R., Mass Spectrometry Applied to Bottom-Up Proteomics: Entering the High-Throughput Era for Hypothesis Testing. *Annu Rev Anal Chem (Palo Alto Calif)* **2016,** *9* (1), 449-72.
115. Mukherjee, M.; Mondal, J., Osmolyte-Induced Collapse of a Charged Macromolecule. *J Phys Chem B* **2019,** *123* (22), 4636-4644.
116. Lyu, J.; Liu, Y.; McCabe, J. W.; Schrecke, S.; Fang, L.; Russell, D. H.; Laganowsky, A., Discovery of Potent Charge-Reducing Molecules for Native Ion Mobility Mass Spectrometry Studies. *Anal Chem* **2020,** *92* (16), 11242-11249.
117. Patrick, J. W.; Laganowsky, A., Generation of Charge-Reduced Ions of Membrane Protein Complexes for Native Ion Mobility Mass Spectrometry Studies. *J Am Soc Mass Spectrom* **2019,** *30* (5), 886-892.
118. Rosgen, J.; Pettitt, B. M.; Bolen, D. W., Protein folding, stability, and solvation structure in osmolyte solutions. *Biophys J* **2005,** *89* (5), 2988-97.
119. Worner, T. P.; Snijder, J.; Bennett, A.; Agbandje-McKenna, M.; Makarov, A. A.; Heck, A. J. R., Resolving heterogeneous macromolecular assemblies by Orbitrap-based single-particle charge detection mass spectrometry. *Nat Methods* **2020,** *17* (4), 395-398.
120. Zheng, X.; Kurulugama, R. T.; Laganowsky, A.; Russell, D. H., Collision-Induced Unfolding Studies of Proteins and Protein Complexes using Drift Tube Ion Mobility-Mass Spectrometer. *Anal Chem* **2020,** *92* (10), 7218-7225.
121. Xia, Z.; Williams, E. R., Protein-Glass Surface Interactions and Ion Desalting in Electrospray Ionization with Submicron Emitters. *J Am Soc Mass Spectrom* **2018,** *29* (1), 194-202.
122. Kenderdine, T.; Xia, Z.; Williams, E. R.; Fabris, D., Submicrometer Nanospray Emitters Provide New Insights into the Mechanism of Cation Adduction to Anionic Oligonucleotides. *Anal Chem* **2018,** *90* (22), 13541-13548.
123. Poltash, M. L.; McCabe, J. W.; Patrick, J. W.; Laganowsky, A.; Russell, D. H., Development and Evaluation of a Reverse-Entry Ion Source Orbitrap Mass Spectrometer. *J Am Soc Mass Spectrom* **2019,** *30* (1), 192-198.
124. Patrick, J. W.; Boone, C. D.; Liu, W.; Conover, G. M.; Liu, Y.; Cong, X.; Laganowsky, A., Allostery revealed within lipid binding events to membrane proteins. *Proc Natl Acad Sci U S A* **2018,** *115* (12), 2976-2981.

125. Weaver, J.; Jiang, M.; Roth, A.; Puchalla, J.; Zhang, J.; Rye, H. S., GroEL actively stimulates folding of the endogenous substrate protein PepQ. *Nat Commun* **2017,** *8* (1), 15934.
126. Desport, J. S.; Frache, G.; Patiny, L., MSPolyCalc: A web-based App for polymer mass spectrometry data interpretation. The case study of a pharmaceutical excipient. *Rapid Commun Mass Spectrom* **2020,** *34 Suppl 2* (n/a), e8652.
127. Gasteiger, E.; Gattiker, A.; Hoogland, C.; Ivanyi, I.; Appel, R. D.; Bairoch, A., ExPASy: The proteomics server for in-depth protein knowledge and analysis. *Nucleic Acids Res* **2003,** *31* (13), 3784-8.
128. Lossl, P.; Snijder, J.; Heck, A. J., Boundaries of mass resolution in native mass spectrometry. *J Am Soc Mass Spectrom* **2014,** *25* (6), 906-17.
129. Liao, Y. D.; Jeng, J. C.; Wang, C. F.; Wang, S. C.; Chang, S. T., Removal of N-terminal methionine from recombinant proteins by engineered E. coli methionine aminopeptidase. *Protein Sci* **2004,** *13* (7), 1802-10.
130. Loo, J. A.; Benchaar, S. A.; Zhang, J., Integrating Native Mass Spectrometry and Top-Down MS for Defining Protein Interactions Important in Biology and Medicine. *Mass Spectrom (Tokyo)* **2013,** *2* (Spec Iss), S0013.
131. Dorsam, R. T.; Gutkind, J. S., G-protein-coupled receptors and cancer. *Nat Rev Cancer* **2007,** *7* (2), 79-94.
132. Laganowsky, A.; Reading, E.; Hopper, J. T.; Robinson, C. V., Mass spectrometry of intact membrane protein complexes. *Nat Protoc* **2013,** *8* (4), 639-51.
133. van Duijn, E.; Simmons, D. A.; van den Heuvel, R. H.; Bakkes, P. J.; van Heerikhuizen, H.; Heeren, R. M.; Robinson, C. V.; van der Vies, S. M.; Heck, A. J., Tandem mass spectrometry of intact GroEL-substrate complexes reveals substrate-specific conformational changes in the trans ring. *J Am Chem Soc* **2006,** *128* (14), 4694-702.
134. Hogan, C. J., Jr.; Ruotolo, B. T.; Robinson, C. V.; Fernandez de la Mora, J., Tandem differential mobility analysis-mass spectrometry reveals partial gas-phase collapse of the GroEL complex. *J Phys Chem B* **2011,** *115* (13), 3614-21.
135. Sobott, F.; Robinson, C. V., Characterising electrosprayed biomolecules using tandem-MS—the noncovalent GroEL chaperonin assembly. *Int J Mass Spectrom* **2004,** *236* (1-3), 25-32.
136. Bush, M. F.; Hall, Z.; Giles, K.; Hoyes, J.; Robinson, C. V.; Ruotolo, B. T., Collision cross sections of proteins and their complexes: a calibration framework and database for gas-phase structural biology. *Anal Chem* **2010,** *82* (22), 9557-65.
137. Klunker, D.; Haas, B.; Hirtreiter, A.; Figueiredo, L.; Naylor, D. J.; Pfeifer, G.; Muller, V.; Deppenmeier, U.; Gottschalk, G.; Hartl, F. U.; Hayer-Hartl, M., Coexistence of group I and group II chaperonins in the archaeon Methanosarcina mazei. *J Biol Chem* **2003,** *278* (35), 33256-67.
138. Ganem, B.; Li, Y. T.; Henion, J. D., Detection of noncovalent receptor-ligand complexes by mass spectrometry. *Journal of the American Chemical Society* **1991,** *113* (16), 6294-6296.

139. Katta, V.; Chait, B. T., Observation of the heme-globin complex in native myoglobin by electrospray-ionization mass spectrometry. *Journal of the American Chemical Society* **1991,** *113* (22), 8534-8535.
140. Panczyk, E. M.; Gilbert, J. D.; Jagdale, G. S.; Stiving, A. Q.; Baker, L. A.; Wysocki, V. H., Ion Mobility and Surface Collisions: Submicrometer Capillaries Can Produce Native-like Protein Complexes. *Anal Chem* **2020,** *92* (3), 2460-2467.
141. Loo, J. A., Studying noncovalent protein complexes by electrospray ionization mass spectrometry. *Mass Spectrom Rev* **1997,** *16* (1), 1-23.
142. Rostom, A. A.; Robinson, C. V., Detection of the intact GroEL chaperonin assembly by mass spectrometry. *Journal of the American Chemical Society* **1999,** *121* (19), 4718-4719.
143. Fort, K. L.; van de Waterbeemd, M.; Boll, D.; Reinhardt-Szyba, M.; Belov, M. E.; Sasaki, E.; Zschoche, R.; Hilvert, D.; Makarov, A. A.; Heck, A. J. R., Expanding the structural analysis capabilities on an Orbitrap-based mass spectrometer for large macromolecular complexes. *Analyst* **2017,** *143* (1), 100-105.
144. Jones, J.; Pack, L.; Hunter, J. H.; Valliere-Douglass, J. F., Native size-exclusion chromatography-mass spectrometry: suitability for antibody-drug conjugate drug-to-antibody ratio quantitation across a range of chemotypes and drug-loading levels. *MAbs* **2020,** *12* (1), 1682895.
145. Li, W.; Yu, J.; Kane, M. A., Quantitation of the Noncovalent Cellular Retinol-Binding Protein, Type 1 Complex Through Native Mass Spectrometry. *J Am Soc Mass Spectr* **2017,** *28* (1), 29-37.
146. Zhang, L.; Vasicek, L. A.; Hsieh, S.; Zhang, S.; Bateman, K. P.; Henion, J., Top-down LC-MS quantitation of intact denatured and native monoclonal antibodies in biological samples. *Bioanalysis* **2018,** *10* (13), 1039-1054.
147. Jennewein, M. F.; Alter, G., The Immunoregulatory Roles of Antibody Glycosylation. *Trends Immunol* **2017,** *38* (5), 358-372.
148. Harvey, D. J.; Merry, A. H.; Royle, L.; P. Campbell, M.; Dwek, R. A.; Rudd, P. M., Proposal for a standard system for drawing structural diagrams of N - and O - linked carbohydrates and related compounds. *PROTEOMICS* **2009,** *9* (15), 3796-3801.
149. Söderlind, E.; Ohlin, M.; Carlsson, R., Complementarity-determining region (CDR) implantation: a theme of recombination. *Immunotechnology : an international journal of immunological engineering* **1999,** *4* (3-4), 279-285.
150. Labrijn, A. F.; Janmaat, M. L.; Reichert, J. M.; Parren, P. W. H. I., Bispecific antibodies: a mechanistic review of the pipeline. *Nature Reviews Drug Discovery* **2019,** *18* (8), 585-608.
151. Kayser, V.; Chennamsetty, N.; Voynov, V.; Forrer, K.; Helk, B.; Trout, B. L., Glycosylation influences on the aggregation propensity of therapeutic monoclonal antibodies. *Biotechnology Journal* **2011,** *6* (1), 38-44.
152. Onitsuka, M.; Kawaguchi, A.; Asano, R.; Kumagai, I.; Honda, K.; Ohtake, H.; Omasa, T., Glycosylation analysis of an aggregated antibody produced by Chinese hamster ovary cells in bioreactor culture. *Journal of Bioscience and Bioengineering* **2014,** *117* (5), 639-644.

153. Beck, A.; Wurch, T.; Bailly, C.; Corvaia, N., Strategies and challenges for the next generation of therapeutic antibodies. *Nature Reviews Immunology* **2010,** *10* (5), 345-352.
154. Shriver, Z.; Raguram, S.; Sasisekharan, R., Glycomics: a pathway to a class of new and improved therapeutics. *Nature Reviews Drug Discovery* **2004,** *3* (10), 863-873.
155. Peng, W.; Zhao, J.; Dong, X.; Banazadeh, A.; Huang, Y.; Hussien, A.; Mechref, Y., Clinical application of quantitative glycomics. *Expert Review of Proteomics* **2018,** *15* (12), 1007-1031.
156. Campuzano, I. D. G.; Robinson, J. H.; Hui, J. O.; Shi, S. D. H.; Netirojjanakul, C.; Nshanian, M.; Egea, P. F.; Lippens, J. L.; Bagal, D.; Loo, J. A.; Bern, M., Native and Denaturing MS Protein Deconvolution for Biopharma: Monoclonal Antibodies and Antibody–Drug Conjugates to Polydisperse Membrane Proteins and Beyond. *Analytical Chemistry* **2019,** *91* (15), 9472-9480.
157. Crivianu-Gaita, V.; Romaschin, A.; Thompson, M., High efficiency reduction capability for the formation of Fab′ antibody fragments from F(ab)2 units. *Biochemistry and Biophysics Reports* **2015,** *2*, 23-28.
158. Marcoux, J.; Champion, T.; Colas, O.; Wagner-Rousset, E.; Corvaïa, N.; Van Dorsselaer, A.; Beck, A.; Cianférani, S., Native mass spectrometry and ion mobility characterization of trastuzumab emtansine, a lysine-linked antibody drug conjugate. *Protein Science* **2015,** *24* (8), 1210-1223.
159. Kafader, J. O.; Melani, R. D.; Schachner, L. F.; Ives, A. N.; Patrie, S. M.; Kelleher, N. L.; Compton, P. D., Native vs Denatured: An in Depth Investigation of Charge State and Isotope Distributions. *J Am Soc Mass Spectr* **2020,** *31* (3), 574-581.
160. McCabe, J. W.; Shirzadeh, M.; Walker, T. E.; Lin, C. W.; Jones, B. J.; Wysocki, V. H.; Barondeau, D. P.; Clemmer, D. E.; Laganowsky, A.; Russell, D. H., Variable-Temperature Electrospray Ionization for Temperature-Dependent Folding/Refolding Reactions of Proteins and Ligand Binding. *Anal Chem* **2021,** *93* (18), 6924-6931.
161. Brown, C. J.; Woodall, D. W.; El-Baba, T. J.; Clemmer, D. E., Characterizing Thermal Transitions of IgG with Mass Spectrometry. *J Am Soc Mass Spectrom* **2019,** *30* (11), 2438-2445.
162. Marty, M. T.; Baldwin, A. J.; Marklund, E. G.; Hochberg, G. K.; Benesch, J. L.; Robinson, C. V., Bayesian deconvolution of mass and ion mobility spectra: from binary interactions to polydisperse ensembles. *Anal Chem* **2015,** *87* (8), 4370-6.
163. Bern, M.; Caval, T.; Kil, Y. J.; Tang, W.; Becker, C.; Carlson, E.; Kletter, D.; Sen, K. I.; Galy, N.; Hagemans, D.; Franc, V.; Heck, A. J. R., Parsimonious Charge Deconvolution for Native Mass Spectrometry. *Journal of Proteome Research* **2018,** *17* (3), 1216-1226.
164. Consortium, T. U., UniProt: the universal protein knowledgebase in 2021. *Nucleic Acids Research* **2020,** *49* (D1), D480-D489.
165. Scigelova, M.; Hornshaw, M.; Giannakopulos, A.; Makarov, A., Fourier Transform Mass Spectrometry. *Molecular & Cellular Proteomics* **2011,** *10* (7), M111.009431.

166. Townsend, J. A.; Keener, J. E.; Miller, Z. M.; Prell, J. S.; Marty, M. T., Imidazole Derivatives Improve Charge Reduction and Stabilization for Native Mass Spectrometry. *Analytical Chemistry* **2019,** *91* (22), 14765-14772.
167. Gadgil, H. S.; Pipes, G. D.; Dillon, T. M.; Treuheit, M. J.; Bondarenko, P. V., Improving mass accuracy of high performance liquid chromatography/electrospray ionization time-of-flight mass spectrometry of intact antibodies. *J Am Soc Mass Spectr* **2006,** *17* (6), 867-872.
168. Bondarenko, P. V.; Second, T. P.; Zabrouskov, V.; Makarov, A. A.; Zhang, Z., Mass measurement and top-down HPLC/MS analysis of intact monoclonal antibodies on a hybrid linear quadrupole ion trap-orbitrap mass spectrometer. *J Am Soc Mass Spectr* **2009,** *20* (8), 1415-1424.
169. Schachner, L.; Han, G.; Dillon, M.; Zhou, J.; McCarty, L.; Ellerman, D.; Yin, Y.; Spiess, C.; Lill, J. R.; Carter, P. J.; Sandoval, W., Characterization of Chain Pairing Variants of Bispecific IgG Expressed in a Single Host Cell by High-Resolution Native and Denaturing Mass Spectrometry. *Analytical Chemistry* **2016,** *88* (24), 12122-12127.
170. Uetrecht, C.; Rose, R. J.; Van Duijn, E.; Lorenzen, K.; Heck, A. J. R., Ion mobility mass spectrometry of proteins and proteinassemblies. *Chem. Soc. Rev.* **2010,** *39* (5), 1633-1655.
171. Ben-Nissan, G.; Sharon, M., The application of ion-mobility mass spectrometry for structure/function investigation of protein complexes. *Current Opinion in Chemical Biology* **2018,** *42*, 25-33.
172. Degiacomi, M. T.; Benesch, J. L. P., EM∩IM: software for relating ion mobility mass spectrometry and electron microscopy data. *The Analyst* **2016,** *141* (1), 70-75.
173. Hyung, S.-J.; Robinson, C. V.; Ruotolo, B. T., Gas-Phase Unfolding and Disassembly Reveals Stability Differences in Ligand-Bound Multiprotein Complexes. *Chemistry & Biology* **2009,** *16* (4), 382-390.
174. Wyttenbach, T.; Grabenauer, M.; Thalassinos, K.; Scrivens, J. H.; Bowers, M. T., The effect of calcium ions and peptide ligands on the relative stabilities of the calmodulin dumbbell and compact structures. *J Phys Chem B* **2010,** *114* (1), 437-47.
175. Illes-Toth, E.; Dalton, C. F.; Smith, D. P., Binding of Dopamine to Alpha-Synuclein is Mediated by Specific Conformational States. *J Am Soc Mass Spectrom* **2013,** *24* (9), 1346-54.
176. Dong, S.; Wagner, N. D.; Russell, D. H., Collision-Induced Unfolding of Partially Metalated Metallothionein-2A: Tracking Unfolding Reactions of Gas-Phase Ions. *Anal Chem* **2018,** *90* (20), 11856-11862.
177. Shirzadeh, M.; Poltash, M. L.; Laganowsky, A.; Russell, D. H., Structural Analysis of the Effect of a Dual-FLAG Tag on Transthyretin. *Biochemistry* **2020,** *59* (9), 1013-1022.
178. Dixit, S. M.; Polasky, D. A.; Ruotolo, B. T., Collision induced unfolding of isolated proteins in the gas phase: past, present, and future. *Curr Opin Chem Biol* **2018,** *42*, 93-100.
179. Gadkari, V. V.; Ramirez, C. R.; Vallejo, D. D.; Kurulugama, R. T.; Fjeldsted, J. C.; Ruotolo, B. T., Enhanced Collision Induced Unfolding and Electron Capture Dissociation of Native-like Protein Ions. *Anal Chem* **2020,** *92* (23), 15489-15496.

180. Vallejo, D. D.; Polasky, D. A.; Kurulugama, R. T.; Eschweiler, J. D.; Fjeldsted, J. C.; Ruotolo, B. T., A Modified Drift Tube Ion Mobility-Mass Spectrometer for Charge-Multiplexed Collision-Induced Unfolding. *Analytical Chemistry* **2019,** *91* (13), 8137-8146.
181. Stow, S. M.; Causon, T. J.; Zheng, X.; Kurulugama, R. T.; Mairinger, T.; May, J. C.; Rennie, E. E.; Baker, E. S.; Smith, R. D.; McLean, J. A.; Hann, S.; Fjeldsted, J. C., An Interlaboratory Evaluation of Drift Tube Ion Mobility-Mass Spectrometry Collision Cross Section Measurements. *Anal Chem* **2017,** *89* (17), 9048-9055.
182. Eschweiler, J. D.; Martini, R. M.; Ruotolo, B. T., Chemical Probes and Engineered Constructs Reveal a Detailed Unfolding Mechanism for a Solvent-Free Multidomain Protein. *Journal of the American Chemical Society* **2017,** *139* (1), 534-540.
183. Campuzano, I. D. G.; Larriba, C.; Bagal, D.; Schnier, P. D., Ion Mobility and Mass Spectrometry Measurements of the Humanized IgGk NIST Monoclonal Antibody. In *State-of-the-Art and Emerging Technologies for Therapeutic Monoclonal Antibody Characterization Volume 3. Defining the Next Generation of Analytical and Biophysical Techniques*, American Chemical Society: 2015; Vol. 1202, pp 75-112.
184. May, J. C.; Jurneczko, E.; Stow, S. M.; Kratochvil, I.; Kalkhof, S.; McLean, J. A., Conformational Landscapes of Ubiquitin, Cytochrome c, and Myoglobin: Uniform Field Ion Mobility Measurements in Helium and Nitrogen Drift Gas. *Int J Mass Spectrom* **2018,** *427*, 79-90.
185. Stiving, A. Q.; Jones, B. J.; Ujma, J.; Giles, K.; Wysocki, V. H., Collision Cross Sections of Charge-Reduced Proteins and Protein Complexes: A Database for Collision Cross Section Calibration. *Anal Chem* **2020,** *92* (6), 4475-4483.
186. Hansen, K.; Lau, A. M.; Giles, K.; McDonnell, J. M.; Struwe, W. B.; Sutton, B. J.; Politis, A., A Mass-Spectrometry-Based Modelling Workflow for Accurate Prediction of IgG Antibody Conformations in the Gas Phase. *Angew Chem Int Ed Engl* **2018,** *57* (52), 17194-17199.